

May 1992

**Thermal and Structural
Tests of René 41
Honeycomb Integral-Tank
Concept for Future Space
Transportation Systems**

John L. Shideler,
Roger A. Fields,
Lawrence F. Reardon,
and Leslie Gong

1992

**Thermal and Structural
Tests of René 41
Honeycomb Integral-Tank
Concept for Future Space
Transportation Systems**

John L. Shideler
*Langley Research Center
Hampton, Virginia*

Roger A. Fields,
Lawrence F. Reardon,
and Leslie Gong
*Dryden Flight Research Facility
Edwards, California*



National Aeronautics and
Space Administration
Office of Management
Scientific and Technical
Information Program

1992

The use of trademarks or names of manufacturers in this report is for accurate reporting and does not constitute an official endorsement, either expressed or implied, of such products or manufacturers by the National Aeronautics and Space Administration.

Summary

Two flat 12- by 72-in. René 41 honeycomb sandwich panels were tested to produce combined thermal and mechanical longitudinal stresses that simulate those that would occur in a larger, more complex integral tank-and-fuselage structure of an Earth-to-orbit vehicle. Elastic strains measured at temperatures below 400°F are compared with calculated values obtained from a linear elastic finite-element analysis to verify the analytical model and to establish confidence in the calculated strains. Elastic strains measured at higher temperatures (between about 600°F and 1400°F), where strain measurement is more difficult and less certain, are also compared with calculated strains. Agreement between measured and calculated strains for the lower temperatures is good, but agreement for the higher temperatures is poor because of unreliable strain measurements. Results from the tests of the first panel indicate that an ascent-and-entry life of 500 cycles is attainable under high combined thermal and mechanical elastic strains. The second panel supported applied combined mechanical and thermal loads even though the maximum compressive strain was more than 2.3 times the tensile proportional limit strain, 1.4 times the tensile yield strain, and 0.88 times the tensile ultimate strain.

Introduction

Studies of future reusable Space Transportation Systems (STS's) considered both insulated and hot-structure concepts (refs. 1 through 7). One such STS study (refs. 6 and 7) employed the hot-structure, integral tank-and-fuselage concept shown in figure 1. This vehicle concept combined the functions of propellant containment, cryogenic insulation, thermal protection, and support of the vehicle thrust and aerodynamic loads. The vehicle, which was designed for 500 missions (500 ascents and 500 entries), used a large wing planform area to achieve a low wing loading. This design approach resulted in a longer, higher altitude entry trajectory than that flown by the Space Shuttle orbiter, which has a relatively high wing loading. This higher altitude trajectory resulted in a maximum entry temperature over much of the vehicle of about 1400°F, which is considerably less than that experienced on the Space Shuttle and which is within the operating range for superalloy materials such as René 41.

The construction of the proposed tank wall for the hot-structure vehicle concept shown in figure 1 consists of a vacuum-sealed René 41 superalloy honeycomb-core sandwich on the lower surface of the vehicle. Although the superalloy material is used

on the higher temperature, windward, lower surface of the vehicle, vacuum-sealed Ti-6Al-4V honeycomb-core sandwich is used on the cooler, leeward, upper surface of the vehicle to save weight. Tension struts at each frame location carry internal pressure loads in the noncircular section. During ascent, the inner face sheet of the sandwich has a temperature of -423°F due to exposure to liquid hydrogen (LH₂) cryogenic fuel, and the outer face sheet has a maximum temperature of 400°F due to exposure to the ascent aerothermal environment. The difference in temperatures of the face sheets during ascent can produce large thermal stresses that must be accommodated in the design. These thermal stresses are reduced by the addition of longitudinal slots (fig. 1) located in the outer face sheet of the lower surface of the vehicle. A more detailed discussion of the vehicle concept is given in references 6 through 8.

In the present study, two 12- by 72-in. panels were tested to produce combined thermal and mechanical longitudinal stresses that simulated those that would occur in the larger, more complex integral tank-and-fuselage structure shown in figure 1. The panels were fabricated by The Boeing Aerospace Company and were tested at the Dryden Flight Research Facility.

This paper presents the results of the tests that were conducted to (1) evaluate the structural behavior of two 12- by 72-in. René 41 honeycomb-core sandwich panels designed to withstand the high, combined thermal and mechanical elastic stresses that could occur in an integral cryogenic tank-and-fuselage structure during repeated ascent and entry cycles; (2) explore the effect on panel strength and behavior of increasing these stresses beyond the proportional limit; and (3) gain experience in the use of strain gages in high- and low-temperature environments. Panel 1 was exposed to 500 mission (ascent and entry) cycles, and panel 2 was exposed to 252 ascent cycles. Temperatures, strains, and deflections were measured. Elastic strains, calculated with measured temperature as the thermal load, were compared with measured strains. After exposure to the cyclic tests, each panel was tested to failure by incrementally increasing the mechanical load while the thermal load was held constant. Preliminary results from this study are presented in reference 9.

Symbols and Abbreviations

DEF	deflectometer
E	modulus of elasticity, psi
G	shear modulus, psi
h	core height, in.

LH ₂	liquid hydrogen
LN ₂	liquid nitrogen
<i>M</i>	moment, in-lbf
<i>P_c</i>	pitch of honeycomb core cell, in.
<i>P_e</i>	pitch of finite elements representing the core, in.
SG	strain gage
<i>T</i>	temperature, °F
<i>t</i>	time, sec
<i>t_c</i>	thickness of honeycomb core foil, in.
<i>t_{ec}</i>	thickness of finite elements representing the core, in.
<i>t_{ef}</i>	thickness of finite elements representing the face sheets, in.
<i>t_f</i>	thickness of face sheets, in.
TC	thermocouple
<i>w</i>	deflection in <i>z</i> -direction, in.
<i>x, y, z</i>	panel coordinates in longitudinal, transverse, and through-the-thickness directions, in.
α	coefficient of thermal expansion, $\frac{\text{in.}}{\text{in.}^\circ\text{F}}$
ϵ	strain associated with stress
ϵ_A	apparent strain
ϵ_m	measured strain
ϵ_p	strain at proportional limit
ϵ_y	yield strain
σ	stress, psi
σ_p	stress at proportional limit, psi

Test Philosophy

The test philosophy selected to introduce combined thermal and mechanical loads into the 12-by 72-in. René 41 honeycomb sandwich panels consisted of the following: (1) immersing one face sheet of a panel in LN₂ to achieve a cryogenic temperature representative of that associated with LH₂ propellant; (2) radiantly heating the other face sheet to achieve temperatures representative of those produced by aerothermal heating during ascent or entry; and (3) applying bending load to achieve mechanical strain representative of that produced by internal pressure and by aerodynamic and thrust loads. Liquid nitrogen (LN₂ at -320°F) was used in place of

the LH₂ for safety reasons. The testing of the flat panel, as illustrated in figure 2, was considered to be representative of testing a complete section of an integral tank-and-fuselage structure. The panel was allowed to expand in the longitudinal direction because no external constraint against longitudinal expansion would exist on an integral tank-and-fuselage structure. However, the representation was incomplete because the test panel was not a shell structure and therefore did not experience circumferential mechanical loads. Nevertheless, the representation was reasonably accurate in simulating the thermal stresses in the integral tank-and-fuselage honeycomb sandwich panel because the slots (fig. 1) in the outer face sheet of the vehicle structure reduced the circumferential thermal stresses to small values (see ref. 8) and caused the behavior of the honeycomb sandwich on the vehicle to approach that of a series of longitudinal panels connected along their sides only by the inner face sheet.

The representation was also incomplete because no frames were welded to the test panel. If a frame were welded to the inner face sheet, the inner face sheet would be constrained to be straight in the transverse direction along the frame, and the honeycomb core at that joint would experience local flat-wise tension due to internal pressure and thermal loads. However, in the test arrangement, the reaction forces at the four simulated frame reaction supports (fig. 2) were in contact with the outer (hot) face sheet of the panel. These reaction forces tended to keep the panel straight in the transverse direction, similar to the way frames constrain the vehicle surface in the transverse direction. However, the test arrangement induced local compression in the honeycomb core rather than tension. (Subsequent to the fabrication of these panels, improvements in the status of welding technology for René 41 that are identified in reference 7 would allow frames to be welded to the honeycomb face sheets.)

Test Panel Fabrication

Honeycomb-core sandwich panels were vacuum brazed at 1975°F using Alloy Metals, Inc., 937 brazing alloy. The cells of the honeycomb core were vacuum sealed. To increase strength, the panels were aged at 1700°F in a vacuum for 1 hour and furnace cooled. Reference 10 contains a detailed discussion of the brazing process.

Panel X rays revealed that a face sheet was poorly brazed to the core over an area approximately 6 by 10 in. near one end of each panel. The poor braze resulted from a cool location within the brazing furnace caused by a missing furnace element. To

avoid expensive repairs, each poorly brazed area was reinforced with bolts that clamped the face sheets to the core. These repairs were acceptable because the ends of the panels were subjected to low bending stresses during the tests.

The dimensions of the two test panels are shown in figure 3. The dimensions of the honeycomb sandwich shown in section A-A were typical of the dimensions for the vehicle concept described in reference 7. Face sheets, which were chemically milled, were nominally 0.020 in. thick except at the regions near the reaction supports for panel 1, where the thickness was 0.025 in. These thicker regions locally reduced the stress in panel 1. The slots in the outer face sheet (fig. 3) were designed to be 0.050 in. wide (ref. 8), but were measured to be 0.041 to 0.043 in. wide. The short slots in panel 2 were positioned to further reduce thermal stress, in addition to the reduction achieved by the long slot along the panel center. The corrugated honeycomb core was fabricated from 0.0015-in-thick foil into 3/16-in-square cells to produce a core solidity of 1.5 percent and a core density of 7.8 lb/ft³. René 41 tooling core that was used around the edge of each panel during brazing inadvertently extended into the structural area of panel 2. Trimming of this core for panel 2 resulted in a width of 11.6 in. instead of 12.0 in. More detailed information on the fabrication of the panels is given in reference 8.

Instrumentation

Panel 1

Locations for the strain gages on panel 1 are listed in table I and shown in figure 4. The sketch at the top of the figure identifies the locations of the applied forces (arrows) and support reactions. All strain gages were uniaxial gages and were oriented on the panel in a longitudinal (x) direction except for those numbered 113 and 114, which were oriented in the transverse (y) direction. Many of the strain gages were clustered around the location $x = 18$ in., where the maximum strain occurs; however, strain gages placed on the outer face sheet were located at $x = 19$ in. to avoid a force-distribution pad that distributed the reaction force at $x = 18$ in. Strain gages identified by numbers less than 1000 were Micro-Measurements WK-06-250BG-350 foil gages, which were bonded to the panel using an epoxy adhesive. These gages have a maximum operating temperature of approximately 600°F. Strain gages numbered 1002, 1004, 1006, and 1008 were Ailtech SG 425 gages and were located on the inner face sheet. These gages, which were spot welded to the panel, have a maximum operating temperature of approximately

1200°F. Data from these weldable gages were not used when the gages were immersed in LN₂ because their responses were erratic. Strain gages 1001, 1003, 1005, and 1007 were Hitec capacitance strain gages and were located on the outer face sheet. These gages, which were also spot welded to the panel, have a maximum operating temperature of approximately 1500°F.

All thermocouples were chromel-alumel (type K) and were enclosed in stainless steel sheathing that was sealed against moisture at each end where the wires exited the sheathing. Each pair of thermocouple wires was spot welded to the surface of the panel. Thermocouple locations for panel 1 are presented in table I and figure 5. Differential thermocouples were attached to each capacitance strain gage element; thus, the measured strain could be adjusted to compensate for the temperature differences between the capacitance gage element and the surface to which it was attached.

Out-of-plane deflections were measured on both panels at the eight locations shown in figure 6. Quartz rods were attached to the panels by hooking the curved end of the rods through loops of stainless steel ribbon that were spot welded to the outer face sheet of the panel. Each rod passed through a bank of quartz heater lamps and was connected to a spring-loaded, wire-wound, potentiometric displacement transducer located in a cool location above the lamps.

The different types of instrumentation and their relative sizes are shown in figures 7 and 8. The strain gage lead wires, which were generally separated to avoid shielding the outer face sheet from radiation from the quartz lamps, were routed as far from lamp power wires as possible to reduce electrical noise on the data. The bolts that reinforced the poorly brazed area of the panel are visible in figure 8.

Panel 2

Deflection measurement, strain gage, and thermocouple locations for panel 2 were nearly identical to those for panel 1. They are presented in table II and in figures 6, 9, and 10. However, capacitance strain gages were not used on panel 2 because it was not exposed to high temperature (1400°F) entry cycles. Strain gages numbered 150 and 151 were three-element, 45° rosettes oriented as shown in figure 9. The center strain gage of rosette 150 was located as close as possible (0.080 in.) to the end of the short slot in the outer face sheet.

Test Apparatus and Procedure

Mechanical Loads

Application of mechanical load was controlled by the electromechanical, closed-loop hydraulic system described in reference 11. Mechanical load from a load actuator was applied to the panel with the distribution system illustrated schematically in figure 11 and shown in the photograph in figure 12. The actuator force was distributed equally, by a whiffle-tree arrangement, to the ends of four stiff beams that traversed the inner face sheet of the panel. A 0.5-in.-diameter rod was welded to the top of each beam. Compression forces were transmitted from these rods to the inner face sheet of the panel through 1.0-in.-wide (1.5 in. wide for panel 2), 0.5-in.-thick steel force-distribution pads, each of which was grooved along its center so that the pads maintained alignment with the rods but did not constrain panel rotation. Rigidized Fiberfrax insulation was located between the pads and the panel to minimize conductive heat transfer from the panel.

The forces were reacted at four line-load reaction supports, each with a beam-rod-pad-insulation arrangement identical to that for the applied forces. The combined effect of the applied forces and reaction forces produced a bending load in the panel. The level of the applied mechanical forces was controlled to produce high elastic strains for panel 1 and plastic strains for panel 2. Additional details of the design and fabrication of the loading system are given in reference 8.

Thermal Loads

The desired temperature histories for both the ascent and the entry cycles for the test panels are shown in figure 13. These temperature histories were selected from the design temperature histories for the vehicle studied in reference 7. The thermally induced moment calculated for the honeycomb sandwich in the vehicle during ascent was $-20\,824$ in-lbf. This moment is based on a model with frames equally spaced at 30 in., a face-sheet thickness of 0.020 in., an inner-face-sheet temperature of -423°F (the temperature of LH_2), and an outer-face-sheet temperature of 400°F . The same face-sheet temperature difference for the panel in the test configuration would have induced a thermal moment at the inner reaction supports ($x = 18$ and $x = 48$ in fig. 4) that was greater than that for the vehicle because the frame reaction supports were not equally spaced at 30 in. (ref. 8). Inner- and outer-face-sheet temperatures of -320°F and 350°F , respectively, on the panel in the test arrangement will produce a thermal moment of

$-20\,824$ in-lbf between the inner reaction supports. Because some nonuniformity in the temperature distribution was expected, the outer face sheet of each test panel at the locations of the control thermocouples (the hottest locations) was heated to 400°F so that a thermal moment equal to or greater than that associated with the vehicle design of reference 7 would be produced.

The use of LN_2 in place of LH_2 had only a small effect on the difference in thermal strains of the face sheets, because the slope of the curve of thermal strain versus temperature for René 41 (ref. 7) at 400°F is about five times greater than it is at -423°F . Consequently, the small increment of differential thermal strain (about 200 microinches per inch) not generated on the cold face sheet could have been generated by increasing the hot-face-sheet temperature by only 20°F . This temperature change was small compared with measured variations in outer-face-sheet temperatures.

Three high thermal stress conditions occur during the thermal cycles (fig. 13). The first condition occurs during the ascent cycle at $t = 120$ sec when the maximum temperature of the outer face sheet reaches 400°F , and the temperature of the inner face sheet remains at the cryogenic temperature. The second condition occurs during the entry cycle at $t = 230$ sec when the maximum entry temperature difference between the outer and inner face sheets (200°F) is reached. The third condition occurs during the entry cycle at $t = 1490$ sec when the maximum outer-face-sheet temperature of 1400°F is reached. The temperature of the inner face sheet was not controlled during entry cycles.

Radiant heaters were used to produce the elevated-temperature test cycles. The radiant heaters (figs. 11, 12, and 14) were assembled from 1000-W quartz lamps (with 10-in. filaments) and Cotronics 310 ceramic foam insulative reflectors. The lamps were located on 0.875-in. centers and were supported 6.0 in. above the test panel. The ends of the quartz lamps were installed in holes drilled through the sides of the ceramic reflectors. The lamps in each of four zones (figs. 5 and 10) were wired in parallel. The temperature in each zone was controlled with a single feedback thermocouple (thermocouples numbered 501, 502, 503, and 504). Ceramic side reflectors were attached around the periphery of the heater to reduce heat loss at the edges of the panel and to reduce convective air currents. Results from initial tests indicated the need to extend the side reflectors down to a level even with the outer face sheet of the panel. Additionally, aluminum tape was attached to the side reflectors during the ascent cycles to increase surface

reflectance, and a 1.5-in-wide strip of Fiberfrax insulation was suspended 4 in. above the longitudinal centerline of the panel to partially shield the center of the panel from the quartz lamps. These modifications resulted in an increased heat flux to the edges of the panel relative to the centerline of the panel and thereby improved the uniformity of the heating.

The cryogenic temperature on the inner face sheet during the ascent cycles was obtained by partially immersing the test panel in the container of LN₂ (figs. 11, 12, and 15). The level of LN₂ was manually maintained. Aluminum adhesive tape and ceramic fibrous insulation (fig. 15) were placed around the edges of the panels to prevent the cold liquid from contacting the honeycomb core and to reduce convective air currents on the outer face sheet of the panel. The aluminum tape provided an adequate seal throughout each series of ascent cycles.

Combined Loads

Combined thermal and mechanical loads were applied - quartz lamps heated the outer face sheet, LN₂ cooled the inner face sheet (during ascent cycles only), and the hydraulic actuator and whiffletree arrangement applied bending to the panels to obtain selected total strain levels (ref. 8). Typical load, shear, bending moment, slope, and deflection diagrams for a combined thermal and mechanical loading condition on the panel are shown in figure 16. For this analysis, the panel was assumed to be a simple beam. The diagrams for mechanically applied load and thermally applied load can be superimposed to obtain the total applied load. A mechanical force of 980 lbf was applied at $x = 9$ and 30 in., and the temperatures of the outer and inner face sheets were 350°F and -320°F, respectively. The shear and moment diagrams for the applied mechanical load (fig. 16(a)) and for the thermally applied load (fig. 16(b)) are shown separately to illustrate the effects of the thermal moment. The moment of 18 263 in-lbf applied at $x = 0$ in. (left column of fig. 16(b)) was required to keep the panel straight (no out-of-plane deflection) when the outer and inner face sheets were at 350°F and -320°F, respectively. The moment of -18 263 in-lbf applied at $x = 0$ in. (right column of fig. 16(b)) was the mechanical equivalent of the thermal moment and allowed the panel to be treated as a structure without temperature effects. The upward and downward forces of 1157 lbf are required to maintain zero deflection at $x = 0$ and 18 in. Thus, deflection due to the thermal load can be obtained by integrating twice the moment distribution shown in the right column of figure 16(b). Bending stress due to the thermal load can be obtained by analysis from the sum of the

moment distributions in the left and right columns of figure 16(b). The loading arrangement produced the maximum bending moment (5.98×10^3 in-lbf due to mechanical load and 20 824 in-lbf due to thermal load) at the internal reaction supports ($x = 18$ and 48 in.).

A typical application of the combined loads is illustrated in figure 17. At the beginning of each test day, strain gages were balanced to read zero before mechanical and thermal test loads were applied. The mechanical load was applied first and held constant. The thermal cyclic load was repeated until all test cycles were completed for a given day. The inner-face-sheet temperature was held constant by the LN₂ during the ascent cycles but was allowed to change during the entry cycles. The outer face sheet of the panels was heated to an initial temperature of -162°F for ascent cycles and 90°F for entry cycles at a rate of 0.5°F per second to initiate controlled heating at a low power level, after which temperature rise rates were 4°F per second for the ascent cycles and 3°F per second for the entry cycles. Nitrogen gas was used to convectively cool the panels at the end of each entry cycle to reduce test time. The next cycle was started when the face-sheet temperatures cooled to about 300°F. The effect of this shortened cycle on the temperatures of the inner and outer face sheets was negligible after the first 200 sec of each entry cycle.

The sequence of panel tests is summarized in table III. Panel 1 was exposed to both ascent and entry cycles. Because the ascent cycles produced higher thermal stress levels, they were of greater interest; thus, panel 2 was exposed only to ascent cycles.

Panel 1 was exposed first to a mechanical load cycle. Then a thermal stress cycle was applied separately, prior to exposure to combined loads. The panel was next exposed to 500 ascent cycles and 500 entry cycles. Ascent and entry cycles were alternated in groups of 1, 49, 50, 100, 100, and 200 cycles. (See table III.) These test groups were employed as a compromise between alternating ascent and entry cycles on a one-to-one basis to best simulate realistic vehicle missions and minimizing test costs by conducting 500 ascent cycles followed by 500 entry cycles. After the 500 ascent and 500 entry cycles were completed, ascent cycles 501 through 531 were imposed on the panel with a higher level of mechanical load than that used for previous cycles. This load produced a higher, but still elastic, total strain level. The panel was then intentionally failed on cycle 532 by increasing the mechanical load.

After initial separate mechanical load and thermal stress tests that were similar to those for the ascent cycle tests on panel 1, panel 2 was exposed to combined-load ascent cycles. As the number of accumulated ascent cycles increased, the mechanical load was incrementally increased. After cycle 152, the stress in the panel exceeded the proportional limit at the reaction supports. Additional ascent cycles (cycles 153 through 252) were imposed on the panel with incrementally increasing strain levels in the plastic range (table III). During cycles 253 and 254, the mechanical load was increased to the load limit of the loading mechanism in an attempt to fail the panel.

Data Reduction

All data were recorded at a rate of one sample per second and subsequently reduced to engineering units with the data acquisition equipment described in reference 11.

Strain gage data from both the foil gages and the weldable gages were corrected for apparent strain with the curves shown in figure 18. The correction shown for the foil gages is an average of data from four gages bonded to a René 41 test specimen. The correction shown for the weldable gages is based on data from a single strain gage welded to René 41.

The capacitance-type strain gage did not require correction for apparent strain due to a difference in coefficients of thermal expansion between the panel and the strain gage because the gage was fabricated from René 41. However, the output of the strain gage did require a correction for the temperature difference between the strain gage element and the test material. This correction, which was obtained for temperature differences up to 50°F, was necessary because the strain gage element was located above the test specimen and was close to the radiant heat source. During the tests, the temperature difference was determined from a thermocouple attached to each strain gage element and a thermocouple attached to the test material immediately adjacent to each gage.

Analysis

The finite-element structural analysis computer program SPAR (ref. 12) was used to calculate strains and stresses produced by applied mechanical loads and temperature distributions. The associated structural model is shown in figure 19. Because of symmetry, only one-fourth of the panel was included in the model.

The 250-node finite-element model consisted of 192 quadrilateral membrane elements (SPAR E41

elements) that represented the face sheets and 220 quadrilateral membrane elements, arranged in the pattern of an egg carton, that represented the honeycomb core. The material properties, taken from reference 13, and the geometric properties for the finite elements are given in table IV. Each element was assigned the material properties (listed in table IV) that corresponded most closely to the temperature of that element. The thicknesses of the elements representing face sheets were equal to the thicknesses of the face sheets. The through-the-thickness extensional stiffness and the shear stiffness of the core were determined based on the unit cross-sectional thickness of the core. (See table IV.) Because the extensional stiffness of the corrugated core in the plane of the panel was low, the in-plane extensional stiffness of the core elements was arbitrarily assumed to be 0.001 times the stiffness through the thickness.

The panel was analyzed for applied loads associated with both ascent and entry conditions. Results were obtained for cases that included mechanical loads separately, thermal loads separately, and combined mechanical and thermal loads.

The mechanical loads, which represent internal pressure and tank and fuselage bending loads, were applied to the panel at the locations identified in figure 19. Concentrated forces were applied to the model at each node along the line from node 22 to 30 and along the line from node 182 to 190. The forces at the end nodes of each line were half those at the internal nodes.

Temperatures obtained from measured data were applied at the model node points. Because the nodes were not coincident with the thermocouple locations, temperatures at the nodes were determined by visually fairing the measured data. Because it is assumed in the SPAR program that a stress-free state exists at 0°F and because it was assumed in the tests that a stress-free state existed at the initial test temperature of approximately 90°F, the measured temperatures were reduced by 90°F to obtain the nodal temperatures used in the analyses. Measured temperatures for the five analyzed cases are given in table V.

Boundary conditions representing symmetry were applied on the edges of the model that correspond to the panel centerlines, except hot-face-sheet nodes 1, 11, 21, ..., 241 were not constrained to prevent transverse deflections or rotations about the longitudinal axis. This exception simulated the effects of the slot along the longitudinal centerline. Additionally, deflections in the z-direction (out-of-plane) were usually constrained at nodes 111 (the central node

directly above node 112), 113, 115, 117, 119, 241, 243, 245, 247, and 249 to simulate frame reactions. Because these boundary conditions allowed no out-of-plane deflection along their respective transverse locations, they simulated the attachment of stiff frames to the panel. Because frames were not welded to the panel in the test setup and transverse bowing was allowed to occur, another set of boundary conditions was used to represent a condition where the panel was free to bow in the transverse direction at the internal support (i.e., nodes 113, 115, 117, and 119). For this second case, the deflections in the vertical direction were constrained only at nodes 111, 241, 243, 245, 247, and 249. All other constraints were the same as for the first case.

Results and Discussion

General

Typical measured temperatures and strains resulting from exposure of the panels to the previously described ascent and entry loads are shown in figure 20. The results are shown for locations near the reaction support at $x = 18$ in. As previously mentioned, $x = 18$ in. represents a vehicle frame location where maximum longitudinal strains occur in the face sheet. Results are shown in units of strain because stresses that include biaxial effects cannot be determined accurately from a single strain gage. However, measured strains are directly comparable with the strains calculated from the finite-element analysis.

For the typical ascent cycle (cycle 81), the mechanical load caused compression in the outer face sheet and tension in the inner face sheet at $x = 19$ in. (See fig. 20(a).) The mechanical load was held constant during the remainder of the test. After the LN_2 contacted the inner face sheet and the inner-face-sheet temperatures stabilized at -320°F , the heating cycle was initiated. Heating of the outer face sheet caused additional compression and tension to occur in the outer and inner face sheets, respectively. These additional thermally induced strains were large compared with those resulting from the mechanical load and LN_2 cooling. Maximum strains occurred at the time of maximum temperature difference, which coincided with the time of maximum outer-face-sheet temperature. The temperatures and strains at this time are presented for ascent cycles in subsequent figures.

For the typical entry cycle (cycle 196), the mechanical load caused tension in the outer face sheet and compression in the inner face sheet at $x = 23$ in. (See fig. 20(b).) Tension occurred here as a result of a permanent bow in the panel, which prevented compression from occurring until the panel contacted the

reaction supports. The mechanical load, which was held constant during the remainder of the test, was less than that for the ascent cycle because the assumption was that fuselage and tank structure would be empty during entry. Although the entry cycle temperatures were much higher than the ascent cycle temperatures, the entry heating cycle produced strains that were less than those for the ascent cycle because the temperature difference between the outer and inner face sheets of the sandwich structure was less. The maximum strains associated with stress again occurred at the time of maximum temperature difference. Since allowable stress decreases with increasing temperature, results for entry cycles are given in subsequent figures at both the time of maximum temperature difference and the time of maximum temperature.

Calculated deflections along the centerline ($y = 6$ in.) are shown in figure 21(a) for a 1575-lbf mechanical load applied at each load point and for the ascent thermal load at a time of maximum temperature difference between the outer and inner face sheets. The solid lines represent results obtained from the finite-element analysis, and the dashed lines represent deflections obtained from classical beam theory by integrating moment distribution curves. The deflections due to thermal load calculated from the finite-element analysis were obtained by using temperatures measured during the "thermal-only" ascent load cycle. Deflections obtained from the classical beam solution used uniform temperatures of 350°F on the outer face sheet and -320°F on the inner face sheet. Boundary conditions imposed on the finite-element model allowed no transverse bowing along the reaction node points at $x = 0$ and 18 in. The curves show the same trends. Results from beam theory do not include biaxial effects and are based on uniform face-sheet temperatures. Consequently, the results from the finite-element analyses are considered more accurate.

Deflections calculated with the finite-element analysis for the thermal-load-only ascent are compared in figure 21(b) with measured deflections along the location $y = 8.6$ in. Boundary conditions used to obtain the solid line did not allow bowing in the transverse direction at $x = 18$ in., but the boundary conditions used to obtain the dashed line did allow such bowing. The measured deflections generally fall between results for the two boundary conditions.

Application of Apparent Strain Data

As previously mentioned in the section entitled "Data Reduction," the output from the foil and weldable strain gages was corrected for apparent

strain by using the curves shown in figure 18. The scatter in apparent strain obtained from reference 14 for eight foil gages attached to titanium and that for seven weldable strain gages welded to titanium are compared in figure 22. The small scatter in the data for the foil strain gages indicates that a high consistency existed among these gages and that the use of a single apparent strain curve for the foil gages is justified. The scatter for the weldable strain gages indicates that the apparent strain varied from gage to gage by as much as 400 $\mu\text{in/in.}$ and could vary by even greater amounts at temperatures above 900°F. Data from reference 15 indicate that scatter in apparent strain between the gages welded to René 41 can be even greater than that from reference 14. To eliminate this potentially large error, the correction for apparent strain for the weldable gages should be determined for each gage. Unfortunately, the tests reported herein were completed prior to the tests of reference 14. Consequently, since all the strain data presented herein from the weldable strain gages were corrected with the apparent strain from a single gage (fig. 18), the data presented herein from weldable gages cannot be considered to be dependable even though it is consistent, often appears reasonable, and may be accurate. Subsequent to these tests, a procedure for determining the apparent strain for a weldable strain gage prior to attaching the gage was determined. The procedure is given in reference 16.

Even though capacitance strain gages did not require correction for apparent strain, frequent loss of strain gage element thermocouples prevented good strain data from being obtained. Furthermore, because the capacitance strain gage elements were exposed to radiation from the quartz lamps and the power to the lamps fluctuated, the temperature differences between the strain gage elements and the material to which they were attached were often much larger than the nominal 50°F for which the strain gages could be accurately corrected. (Temperature differences were as large as 200°F during the entry cycles.) Consequently, the constantly changing corrections to the output of the capacitance strain gages were often large with respect to the strain being measured and resulted in unreliable, erratic data.

Panel 1

Since it is not practical to present results from each of the 532 ascent cycles and 500 entry cycles for panel 1, only selected results are presented to describe the typical response of the panel to the applied combined thermal and mechanical loads.

Typical temperature distributions. Temperature distributions, such as those shown in figures 23 and 24, were generated by visually fairing data obtained from thermocouples. The grids shown in the figures identify the nodal pattern for the finite-element structural analyses. The open symbols on the grid represent thermocouple locations. The closed symbols represent "imaged" locations where the temperatures were assumed to be those measured at nearby thermocouple locations because the local temperature distribution was assumed to be symmetrical about $x = 18$ in. The open symbols on the curves identify the data obtained from thermocouples. The curves were faired through the measured data. Temperatures at the grid intersections of the faired curves were used as nodal input to the structural analyses. The measured temperatures are presented in table V. As previously mentioned in the section entitled "Analysis," these temperatures were reduced by 90°F before they were input to the structural analyses to compensate for the stress-free-temperature condition at 0°F required by the SPAR program.

For all ascent cycles, the inner-face-sheet temperature distribution was relatively uniform at approximately the temperature of LN₂ (-320°F). The temperature distributions for the outer face sheet for ascent cycles 1 and 500 were similar (fig. 23); both showed cooler temperatures at $x = 18$ in. due to shading of the panel from the quartz lamps by the reaction support beam. (See fig. 11.) Heat conduction to the reaction beam also may have contributed to the cooler temperature of the outer face sheet in this region, even though the beam was insulated from the panel to minimize this effect. Comparison of figures 23(a) and 23(b) reveals the increase in uniformity of the outer-face-sheet temperatures that was achieved by the modifications to the test setup during the early series of tests. The maximum outer-face-sheet temperature variation was about 300°F for cycle 1 (fig. 23(a)). The modifications, which occurred during the first 135 cycles, reduced the outer-face-sheet temperature variation to less than 200°F (fig. 23(b)). The temperatures shown in figure 23(b) were typical for the ascent cycles after cycle 135.

Typical outer- and inner-face-sheet temperature distributions that occurred during exposure to the entry cycles are shown in figure 24. Since LN₂ was not used to represent cryogenic propellant temperatures during entry cycles, the inner-face-sheet temperature increased as the outer face sheet was heated. The maximum outer-face-sheet temperature shown in figure 24(a) at a time of maximum temperature difference ($t = 230$ sec) was about 1000°F. The

shading effect from the load reaction beam still occurred as it did for the ascent cycle, and the temperatures still decreased near the edges of the panel despite the fixture modifications to improve surface temperature uniformity. The temperatures on each surface were uniform to within about 300°F; the lower temperatures occurred near the panel edge at the reaction support. Nominal temperature differences between the outer and inner face sheets were about 500°F at the time of maximum temperature difference and were about 300°F at the time of maximum temperature (fig. 24(b)). These temperature differences were high compared with the 200°F temperature difference predicted for the vehicle of reference 7. The results calculated in reference 7 included a radiant heat interchange with a warm wall on the opposite side of the tank. Thus, the higher measured temperature differences may have been caused by heat from the inner face sheet of the test panel radiating to a cooler, insulated stainless steel plate that was located about 10 in. below the panel. The temperatures shown in figure 24 were typical of all entry cycles after cycle 135.

Longitudinal strains. Measured longitudinal strains and longitudinal strains calculated from the finite-element analysis for ascent cycle 1 at the time of maximum ascent temperature ($t = 120$ sec, which is also the time of maximum face-sheet temperature difference) are compared in figure 25. Strain distributions along a longitudinal and a transverse cross section are shown for three load conditions: mechanical load, thermal load, and the sum of the thermal and mechanical loads. The sketch at the top of the figure shows the grid pattern used in the finite-element analysis. The calculated results are based on boundary conditions that prevent normal (z -direction) deflections for all values of y at $x = 18$ in. and thus do not allow transverse bowing at that reaction location. The abrupt changes in calculated strain for the outer face sheet at approximately $x = 12$ and 24 in. are caused by a local increase of face-sheet thickness in this region. The decrease in compressive strain in the outer face sheet, shown in the transverse distribution along the line from $y = 6$ in. to $y = 12$ in. (at $x = 19$ in.) is attributed to the decrease in temperature along that line (fig. 23(a)). All test data are from foil strain gages bonded to the panel face sheets. The test data for the applied thermal load were obtained by subtracting the mechanical load data taken before the beginning of the heating cycle from the data taken for combined thermal and mechanical loads. The maximum measured strains occurred near the reaction support and were in good agreement with the calculated results. The poor agreement at $x = 33$ in.

for the outer face sheet may have been a result of a less accurately known temperature distribution near that region since most of the thermocouples were clustered around $x = 20$ in. (fig. 23(a)).

The measured and calculated combined thermal and mechanical strains shown for cycle 1 in figure 25 are compared with data for cycle 500 in figure 26. Although strains were not calculated for all 500 cycles, a review of the temperature distributions for the 500 cycles indicates that the calculated strains for all ascent cycles would have been expected to fall between the boundaries established by the data from cycles 1 and 500. All strains were elastic, and the maximum measured strains were 75 to 80 percent of the strain at the proportional limit. The magnitudes of the calculated and measured strains for cycle 500 were less than those for cycle 1. The shapes of the transverse distributions for the outer face sheet also differed. These differences result from the more uniform temperature distribution on the outer face sheet achieved by the previously described modifications to the test setup. Data for the outer face sheet for cycle 500 (square symbols) are from capacitance strain gages that gave unreliable readings. Figures 25 and 26 reveal that measured strains generally agreed with the calculated strains from the finite-element analyses; thus the analysis model is validated and the importance of accurately determining the temperature distribution to calculate accurate strains is illustrated.

Calculated and measured longitudinal strains for entry cycle 500 are shown in figure 27. The temperature distributions used to calculate the strains for cycle 500 are shown in figure 24. The solid symbols show strains measured during cycle 500, and the connected closed and open symbols show the variation of strain that occurred during the 500 cycles. Strains due to mechanical load (which were calculated for entry cycle 1 and assumed to have been the same for all 500 cycles) were small compared with those for the thermal load because tank-and-fuselage pressure and bending loads are small during entry.

The test data in figure 27 for combined thermal and mechanical loads were obtained from capacitance strain gages on the outer face sheet and from weldable strain gages on the inner face sheet. As previously discussed, data from these high-temperature strain gages were not considered reliable. Inconsistency in the high-temperature data that were obtained from the capacitance strain gages during all 500 cycles is especially noticeable in figure 27(b). Even though some of the weldable strain gages displayed remarkable consistency during these 500 cycles, data from those gages were unreliable because

corrections for apparent strain for the individual gages were not known.

Effect of mission cycles. Summaries of the maximum longitudinal strains recorded at $x = 20.84$ in. during the 500 ascent and entry cycles are shown in figures 28 and 29, respectively. The closest location to the reaction support where data existed for both ascent and entry cycles was $x = 20.84$ in. At this location, consistency of data between all three types of strain gages at a relatively high strain level could be compared.

The measured maximum strains shown in figure 28 for every fifth cycle are relatively unchanged over the 500 ascent cycles, which indicates a relative consistency between tests. The scatter is probably due to variations in temperature distributions from test to test. The scatter decreases as the number of cycles increases because of the previously discussed modifications to the test fixture that improved temperature control. The data from the capacitance strain gage at a temperature of about 400°F (relatively low radiant heating) appear to be as consistent and reliable as the data from the bonded foil gage.

Reliability was not achieved for the capacitance gages at the higher temperatures (about 1400°F) associated with the 500 entry cycles (fig. 29). As discussed previously, the capacitance strain gages produced erratic results at these temperatures, and the thermocouples that measured the temperature of each strain gage element often required repairs. The large gaps in the data for capacitance gage 1003 resulted because testing was not stopped to repair a single gage. In contrast, the welded strain gage number 1004 produced consistent and uniform results (at a temperature of about 1000°F) over 500 entry cycles. However, this strain level cannot be considered reliable since the corrections to the apparent strain for this strain gage could be in error by hundreds of microinches per inch.

Measured time histories of out-of-plane deflection near the center of the panel ($x = 33$ in., $y = 9$ in.) during both ascent and entry cycles are shown in figure 30 for cycles 1, 300, and 500. Most of the deflection occurred during application of the mechanical load rather than during application of the thermal load. Even though the maximum value of the mechanical load remained constant, the center deflection of the panel increased as the number of cycles increased. This increased center deflection was caused by a permanent bowing of the panel that gradually occurred during the test cycles. Panel center deflection was set equal to zero at the beginning of each test

group. Thus, the deflection increased with the number of cycles because the applied mechanical load first straightened the permanent bow in the panel before forcing the panel against the inner reaction supports.

The permanent bowing of panel 1 is shown in figure 31, and the 0.58-in. maximum permanent deflection that remained after 500 ascent and entry cycles is shown in figure 32. Comparison of the solid symbols with their corresponding open symbols in figure 31 reveals that the permanent bow of the panel did not significantly increase during the ascent cycles from cycle 100 to cycle 200 or from cycle 300 to cycle 500, but did significantly increase during the entry portions of the tests. It appears, therefore, that the permanent bowing occurred during the entry cycles, and it is suspected that the bowing was caused by a combination of creep and metallurgical shrinkage (ref. 17) of the René 41 due to additional aging at high temperatures during the entry cycles. The effect that such behavior might have on the design of a vehicle with a honeycomb sandwich integral tank and fuselage is not addressed herein.

Test to failure. Additional ascent cycles (beyond the initial 500) were imposed on the panel with incrementally increasing mechanical load until a failure was achieved during cycle 532. The panel failed in an undesirable mode—core crushing directly beneath an interior reaction support. The failed core is shown in figure 33. Core crushing was not representative of a failure mode that would occur in the vehicle of reference 7 because, as previously mentioned, the test setup placed the core in compression even though the load pattern for an integral tank and fuselage with a frame welded to the inner face sheet would locally place the core in tension. In addition, the risk of core crushing was increased because the reaction loads were purposely concentrated over a small area to minimize shading of the panel from the quartz-lamp radiation during the heating cycles. Subsequent to panel 1 tests and prior to panel 2 tests, the contact area at the reaction loads was increased to reduce local core compression stresses.

Panel 2

The initial separate mechanical and thermal load tests for panel 2 were similar to those for panel 1, except panel 2 was subjected only to ascent tests because the ascent cycle produced larger thermal stresses than the entry cycle because of a larger through-the-thickness temperature difference. The mechanical load was incrementally increased as the number of accumulated ascent cycles increased. After cycle 5, the mechanical load imposed on panel 2

was higher than that imposed on panel 1. The maximum strain at the support, which was determined by extrapolation of strains measured near the support, exceeded the strain at the proportional limit for all cycles after cycle 152 (see table III) and reached a value about 1.3 times greater than the proportional limit strain by cycle 228. Panel 2 was exposed to 152 high elastic cycles and 100 plastic cycles, prior to an attempt to fail the panel.

Typical temperature distributions. The temperature distribution shown in figure 34 for cycle 81 at the time of maximum ascent temperature ($t = 120$ sec) is typical of the 254 ascent-temperature distributions imposed on panel 2. This temperature distribution was used to calculate the strain shown in subsequent figures for cycle 81. The temperature distribution is similar to that shown in figure 23(a) for panel 1. Comparison of figures 34 and 23(a) reveals that the temperature distribution on panel 2 was more uniform, especially in the transverse direction. The warmer areas of the inner face sheet of panel 2 coincided with the part of the panel that was deflected upward (positive z -direction) under combined load near $x = 9$ and $x = 30$ in. This temperature distribution suggests that the panel may have been insulated from the LN_2 by trapped nitrogen gas in these areas.

Longitudinal strains. Strains from finite-element analyses of panel 2, calculated with the applied thermal and mechanical load conditions from cycle 81, are shown in figure 35. The maximum calculated compressive longitudinal strain under combined load, shown at $x = 18$ in. by the solid line, was 93 percent of the proportional limit at 400°F . These results were obtained with the previously described boundary conditions at $x = 18$ in. that simulated a frame constraining the panel to be straight in the transverse direction. Because the test fixture did not constrain the panel to be straight, the panel was also analyzed with boundary conditions at $x = 18$ in. that allowed the panel to bow in the transverse (y) direction. Comparison of the results from these two calculations showed that an increase in maximum longitudinal compressive strain on the outer surface of only about 6 percent would have resulted if the panel were constrained by a frame to be straight in the transverse direction. Consequently, when calculated longitudinal strains are compared with test data, it makes little difference whether the theoretical boundary conditions selected at the reaction support constrained or allowed transverse bowing, since the

boundary conditions at the reaction support during the tests fell between the two extremes.

Because the actual boundary conditions were probably closer to those that allowed transverse bowing, measured longitudinal strains for panel 2 are compared with strains that were calculated with boundary conditions that allowed transverse bowing (fig. 36). All measured data are from foil strain gages. Reasonably good agreement exists between test data and calculated strains, further verifying the validity of the finite-element analysis. All test data in figure 36 are from gages along $y = 8.6$ in., except for one measurement that is from a rosette strain gage located at the end of the 0.042-in-wide intermediate slot at $y = 2.6$ in. Even though the longitudinal strain at the end of the intermediate slot ($x = 15$ in.) must have been zero, the measured value was only slightly less than that measured at a similar location where no intermediate slot existed. The width of the strain gage (0.125 in.) and the distance of the gage from the end of the slot (0.080 in.) are believed to have been too large to provide an accurate measure of the end effect.

Except for the data shown in figure 37, all calculated and measured results are in units of strain. The stresses shown in figure 37 correspond to the strain data in figure 36. The stresses calculated from the finite-element analysis account for biaxial effects in the face sheets. However, the stresses (fig. 37) based on the measured strains were determined by multiplying the measured uniaxial strains by the material modulus of elasticity E and therefore do not include biaxial effects. Since these effects were large in the region around the reaction support, there is reason to expect poor agreement in the region of $x = 18$ in. Hence, the good agreement in this region is considered serendipitous. Comparison of figures 36 and 37 shows the high level of stresses that are associated with the elastic strains to which the panel was cyclically exposed.

Transverse strains. The transverse strains in the panel (fig. 38) are low compared with the longitudinal strains. As would be expected, constraining the panel from transverse bowing along the reaction support ($x = 18$ in.) locally introduced a compression component to the transverse strain of the outer face sheet (i.e., the difference between the solid and dashed lines). However, the outer face sheet was in tension rather than in compression, because the transverse strains were dominated not by the boundary condition at the reaction support, but by (1) the Poisson effect from the large longitudinal compressive strains (see fig. 36) and by (2) the longitudinal

temperature distribution (see fig. 34), both of which induced transverse tension in the outer face sheet.

Even though the longitudinal distribution of transverse strains appears reasonable, the transverse distribution at $x = 18$ in. (fig. 38) indicates that more elements in the transverse direction are needed if we are to calculate the zero stresses that must occur on the free edges at $y = 5.6$ and $y = 11.6$ in. on the outer surface and at $y = 11.6$ in. on the inner surface. Since the finite-element model is inadequate for good definition of all transverse strains, the longitudinal distribution of transverse strains at $y = 8.6$ in. must be considered suspect. Nevertheless, agreement between the measured strains and the strains calculated at $y = 8.6$ in. is not unreasonable. For example, the test data near the reaction support ($x = 18$ in.) would be expected to be between the solid and dashed curves since the reaction forces tended to straighten the panel in the transverse direction, thereby producing a restraint that was between the condition that constrained the panel to be straight and the condition that allowed transverse bowing. Additionally, the data point for the outer face sheet is closer to the prediction for a constrained boundary than is the data point for the inner face sheet. This result appears reasonable since the outer face sheet is in direct contact with the reaction force while the inner face sheet is separated from the reaction force by the core.

Effect of plastic cycles. As additional ascent test cycles were imposed on panel 2, the level of mechanical load was incrementally increased to increase the level of strain. Selected results from these tests, including the results for cycle 81 from figure 36, are shown in figure 39. Elastic strains calculated from the finite-element analysis should be compared only with the data for cycle 81. Calculated results not shown on the figure indicate that the longitudinal strain on the outer face sheet at the reaction centerline ($x = 18$ in.) exceeded the proportional limit beginning with cycle 153. (See table III.) Thus, the panel was exposed to 100 cycles (cycles 153 through 252) during which strain exceeded the proportional limit. As the applied mechanical load was incrementally increased, the area experiencing plastic strain widened until, by cycles 228 through 252, the plastic area extended beyond $x = 19$ in. (See table III and fig. 39.)

A summary of strain data obtained during the 254 ascent cycles imposed on panel 2 is shown in figure 40. The data have less scatter than that shown for panel 1 in figure 28 because of the improved test setup, which consistently produced a more uniform

temperature distribution. Initial data are not shown in the figure because of moisture-induced resistance-to-ground problems, which were not identified and corrected until after cycle 80. The problems, which occurred when accumulated frost on the wires was warmed by the lamps and moisture formed, were corrected by applying a waterproof coating to the wires.

A slight increase in the magnitudes of strain is noticeable in figure 40(a) for $x = 21$ in., which is approximately 3 in. from the reaction support. This slight increase in elastic strain is attributed to the incremental increases in mechanical load. A larger increase in strain is shown in figure 40(b) for a location only 1 in. from the reaction support ($x = 19$ in.). Abrupt changes in strain can be identified at the cycles where mechanical load was increased. The strains at $x = 19$ in. increased beyond the proportional limit beginning with cycle 203.

Another effect of increasing the mechanical load was the development of compressive plastic strain in the outer face sheet of panel 2, which caused a permanent bowing in the same direction that panel 1 bowed. However, the creep- and aging-induced change in panel 1 caused by repeated entry cycles was considerably less than the mechanical-loading-induced plastic strain in panel 2. The cause for the small amount of bowing, shown to be about 0.050 in. in figure 41 for panel 2 during the first 100 elastic ascent cycles, is not known. (A small plastic strain at the reaction support at $x = 18$ in. may have occurred during the first 100 cycles because the calculated maximum compressive strain at that location was close to the proportional limit during these cycles (see fig. 35), and the proportional limit and temperature distribution were not exactly known.) The deflection, the shape of which becomes increasingly apparent in figure 41 after test cycle 100, was concentrated where the plastic strain occurred. By the end of the tests, the panel shape approached that of three connected straight segments, as opposed to the shape of panel 1, which exhibited a smoother curvature (fig. 31).

Test to failure. After 252 cycles, the mechanical load was increased to the load limit of the actuator in an attempt to fail the panel. The panel continued to support load during this ascent cycle even though core buckling (see fig. 42) and substantial permanent deflection (see fig. 41) occurred. The panel was subjected to a second cycle, and it continued to support load. For these two cycles, the compression strain measured at a location 1.0 in. from the

reaction centerline was about 2.3 times the proportional limit strain, 1.4 times the yield strain (fig. 39), and 0.88 times the ultimate strain. The ability of the panel to continue to support the applied loads during the occurrence of the large plastic strain indicates that substantial plastic strain can occur in the face sheet of the honeycomb sandwich before ultimate failure. A thorough understanding of the behavior of the panel requires a nonlinear viscoplastic analysis.

Concluding Remarks

Two 12- by 72-in. René 41 honeycomb-core sandwich panels were exposed to cyclic combined thermal and mechanical strains representative of high elastic strains that could occur in an integral cryogenic tank-and-fuselage hot structure of a future space transportation vehicle. The test panels did not have frames attached to them to fully represent an integral tank structure. However, a comparison of strains calculated for free and constrained boundary conditions indicated that an increase in maximum strain of only 6 percent would have resulted if a frame had constrained the panels to be straight in the transverse direction. The first panel was exposed to 500 ascent cycles (outer and inner maximum face-sheet temperatures of about 400°F and -320°F, respectively) and 500 entry cycles (outer and inner maximum face-sheet temperatures of about 1400°F and 1100°F, respectively). Strains were kept in the elastic range. The structural performance of the second panel was evaluated during 254 ascent cycles at elastic strain levels and at strains greater than the proportional limit of the material.

Results from tests of the first panel indicated that an ascent-and-entry-cycle life of 500 is attainable when the panel is exposed to high elastic combined thermal and mechanical strains (75 to 80 percent of proportional limit strain). Longitudinal strains in the elastic range, measured during tests simulating ascent thermal-mechanical loading conditions (temperatures less than 600°F), were in good agreement with calculated strains. The strains were calculated with a finite-element analysis method that used measured test temperatures (which were not uniform on the panel surfaces) and measured applied mechanical loads as input data. The good agreement validated the accuracy of the strain data and the analysis. However, there was poor agreement between measured and calculated strains for tests simulating entry thermal-mechanical loading conditions during which two types of high temperature (above 600°F) strain gages were used. The use of a single apparent-strain correction for the high-temperature, weldable

strain gages produced undependable data. It was concluded that separate apparent-strain corrections are required for each of these gages. In addition, the direct exposure of high, varying heat flux on the capacitance-type strain gages produced unreliable data because large temperature differences between the strain gage elements and the panel caused strain corrections to be required that were large relative to the level of strain being measured.

Significant permanent bowing (0.58-in. over the 72-in. length) occurred on the first panel. This deflection may have resulted from creep and metallurgical shrinkage of the hotter face sheet due to additional aging at the high entry-cycle temperatures. The effect that such a deflection could have on the structural performance of an integral tank-and-fuselage hot structure was not evaluated.

The first panel unexpectedly failed from core crushing due to a highly concentrated test-fixture load at the panel support location. The second panel was exposed to a combined thermal-structural test to the maximum load that could be applied. The panel supported the applied load even though the maximum compressive strain was greater than about 2.3 times the tensile proportional limit strain, 1.4 times the tensile yield strain, and 0.88 times the tensile ultimate strain. The continued support of the applied loads during the occurrence of the large plastic strain indicated that substantial plastic strain can occur in the face sheet of the honeycomb sandwich before ultimate failure. A more thorough understanding of the panel behavior when it is exposed to high combined thermal and mechanical strains requires a nonlinear viscoplastic analysis.

NASA Langley Research Center
Hampton, VA 23665-5225
March 3, 1992

References

1. Kelly, H. Neale; Rummeler, Donald R.; and Jackson, L. Robert: Research in Structures and Materials for Future Space Transportation Systems An Overview. *J. Spacecr. & Rockets*, vol. 20, no. 1, Jan. Feb. 1983, pp. 89-96.
2. Henry, Beverly Z.; and Eldred, Charles H.: Advanced Technology and Future Earth Orbit Transportation Systems. *Space Manufacturing Facilities II*, Jerry Grey, ed., American Inst. of Aeronautics and Astronautics, 1977, pp. 43-51. (Available as AIAA Paper 77-530.)
3. Haefeli, Rudolph C.; Littler, Ernest G.; Hurley, John B.; and Winter, Martin G.: *Technology Requirements for*

Advanced Earth-Orbital Transportation Systems -- Summary Report. NASA CR-2867, 1977.

4. Stone, J. E.; and Koch, L. C.: *Hypersonic Airframe Structures Technology Needs and Flight Test Requirements.* NASA CR-3130, 1979.
5. Taylor, Allan H.; and Jackson, L. Robert: Thermostructural Analysis of Three Structural Concepts for Reusable Space Vehicles. *Technical Papers Conference on Advanced Technology for Future Space Systems*, American Inst. of Aeronautics and Astronautics, Inc., 1979, pp. 76-86. (Available as AIAA Paper 79-0874.)
6. Hepler, A. K.; and Bangsund, E. L.: *Technology Requirements for Advanced Earth Orbital Transportation Systems. Volume 2: Summary Report.* NASA CR-2879, 1978.
7. Dishman, George A.; Hepler, Andrew K.; and Swegle, Allan R.: *Hot Structures for Lifting Reentry Vehicles.* AFWAL-TR-83-3122, U.S. Air Force, Jan. 1984. (Available from DTIC as AD B087 363L.)
8. Hepler, Andrew K.; and Swegle, Allan R.: *Design and Fabrication of Brazen René 41 Honeycomb Sandwich Structural Panels for Advanced Space Transportation Systems.* NASA CR-165801, 1981.
9. Shideler, John L.; Swegle, Allan R.; and Fields, Roger A.: Honeycomb Sandwich Structure for Future Space Transportation Systems With Integral Cryogenic Tankage. *J. Spacecr. & Rockets*, vol. 21, no. 3, May-June 1984, pp. 246-252.
10. Hepler, Andrew K.; Arnquist, John; Koetje, Edward L.; Esposito, John J.; Lindsay, Victor E. J.; and Swegle, Allan R.: *Design Data for Brazen René 41 Honeycomb Sandwich.* NASA CR-3382, 1981.
11. Sefic, Walter J.: *NASA Dryden Flight Loads Research Facility.* NASA TM-81368, 1981.
12. Whetstone, W. D.: *SPAR Structural Analysis System Reference Manual -- System Level 13A. Volume I: Program Execution.* NASA CR-158970-1, 1978.
13. *Military Standardization Handbook--Metallic Materials and Elements for Aerospace Vehicle Structures, Volume 2.* MIL-HDBK-5B, U.S. Dep. of Defense, Sept. 1, 1971.
14. Jenkins, Jerald M.: *A Study of the Effect of Apparent Strain on Thermal Stress Measurement for Two Types of Elevated Temperature Strain Gages.* NASA TM-84904, 1983.
15. Reardon, Lawrence F.: Current Hot Structures Test Instrumentation. *Workshop on Correlation of Hot Structures Test Data With Analysis, Volume I*, NASA CP-3065-Vol. I, 1990, pp. 75-97.
16. Nightingale, C. M.; and Twa, G. J.: Evaluation of Pre-calibration Techniques for Ailtech SG425 Strain Gages. *Strain Gage Accuracy Proceedings of Western Regional Strain Gage Committee*, Soc. for Experimental Stress Analysis, 1982, pp. 6-19.
17. *Metals Handbook*®, Ninth ed. Volume 4 -- Heat Treating. American Soc. for Metals, c.1981.

Table I. Location of Instrumentation on Panel 1

[See figs. 4, 5, and 6]

(a) Outer face sheet

Number	Type	x , in.	y , in.	Number	Type	x , in.	y , in.
^a TC 501		6.00	7.00	TC 235		33.17	7.00
SG 101	Foil	6.00	8.75	SG 121	Foil	33.17	8.77
SG 1001	Capacitance	6.00	9.00	SG 1007	Capacitance	33.17	9.00
TC 201		6.12	9.00	TC 233		33.29	9.03
TC 219		19.11	6.69	^a TC 503		40.70	7.00
SG 115	Foil	19.11	7.00	TC 243		43.39	8.98
^b SG 113	Foil	19.11	8.53	^a TC 504		60.20	7.00
TC 217		18.75	8.81	TC 247		60.20	9.00
SG 111	Foil	19.11	9.00	DEF 301	Deflectometer	-0.69	
SG 117	Foil	20.84	8.77	DEF 302	Deflectometer	6.12	
SG 1003	Capacitance	20.84	9.00	DEF 303	Deflectometer	18.88	
TC 221		20.87	9.03	DEF 304	Deflectometer	33.12	
TC 229		22.95	1.27	DEF 305	Deflectometer	43.39	
TC 227			7.00	DEF 306	Deflectometer	47.53	
SG 119	Foil		8.77	DEF 307	Deflectometer	60.20	
SG 1005	Capacitance	↓	9.00	DEF 308	Deflectometer	66.95	
TC 225		23.00	9.04	TC 801	Differential	6.08	
TC 223		22.95	10.78	TC 821	Differential	20.92	
^a TC 502		25.64	7.00	TC 825	Differential	23.03	
TC 237		33.17	3.00	TC 833	Differential	33.25	↓

^aControl thermocouple.

^bTransverse strain gage.

Table I. Concluded

(b) Inner face sheet

Number	Type	x , in.	y , in.	Number	Type	x , in.	y , in.
SG 102	Foil	6.00	8.50	SG 118	Foil	20.84	8.50
TC 202		↓	8.18	TC 224		22.95	10.75
TC 204			7.00	TC 226			9.35
TC 206		↓	1.25	SG 1006	Weldable		9.00
SG 104	Foil	18.11	9.50	SG 120	Foil		8.50
TC 208		18.28	9.20	TC 228			6.97
SG 1002	Weldable	18.11	8.80	TC 230		↓	1.31
SG 106	Foil		8.50	TC 232		25.64	7.00
TC 210			8.11	TC 234		33.17	9.40
SG 108	Foil		7.00	SG 1008	Weldable		9.00
TC 212			6.65	SG 122	Foil		8.53
SG 110	Foil		4.50	TC 236			7.00
TC 214		↓	4.16	TC 238		↓	3.00
TC 216		19.11	9.33	TC 240		40.70	7.00
SG 112	Foil		9.00	TC 242		43.39	10.75
SG 114	Foil		8.50	TC 244		43.39	6.97
SG 116	Foil		7.00	TC 246		43.39	1.25
TC 220		↓	6.65	TC 248		60.20	9.00
TC 218		19.51	8.50	TC 250		60.20	7.07
TC 222		20.84	9.33	TC 252		60.20	1.19
SG 1004	Weldable	20.84	9.00				

Table II. Location of Instrumentation on Panel 2

[See figs. 6, 9, and 10]

(a) Outer face sheet

Number	Type	x , in.	y , in.	Number	Type	x , in.	y , in.	
SG 101	Foil	7.00	8.35	TC 223	Foil	22.95	10.35	
TC 201		7.00	8.60	^a TC 502		25.64	6.60	
^a TC 501		9.00	6.60	TC 237		33.17	2.60	
^b SG 150	Foil	15.00	2.60	TC 235		↓	6.60	
TC 150		↓	2.85	SG 121			8.35	
^b SG 151			8.60	TC 233			8.60	
TC 151	Foil		^a TC 543	40.70		6.60		
TC 219		19.11	6.69	TC 243			43.39	8.60
SG 115	Foil	19.11	6.60	^a TC 504			60.20	6.60
^c SG 113	Foil	19.11	8.10	TC 247			60.20	8.60
TC 217		18.75	8.40	DEF 301	Deflectometer	−0.69	↓	
SG 111	Foil	19.11	8.60	DEF 302	Deflectometer	6.12		
SG 117	Foil	20.84	8.35	DEF 303	Deflectometer	18.88		
TC 221		20.87	8.60	DEF 304	Deflectometer	33.12		
TC 229		22.95	1.25	DEF 305	Deflectometer	43.39		
TC 227		22.95	6.60	DEF 306	Deflectometer	47.53		
SG 119	Foil	22.95	8.35	DEF 307	Deflectometer	60.20		
TC 225		23.00	8.60	DEF 308	Deflectometer	66.95		

^aControl thermocouple.

^bRosette strain gage.

^cTransverse strain gage.

Table II. Concluded

(b) Inner face sheet

Number	Type	x , in.	y , in.	Number	Type	x , in.	y , in.
SG 102	Foil	7.00	8.60	TC 222		20.84	8.85
TC 202		↓	8.35	SG 1004	Weldable	20.84	8.60
TG 204			6.60	SG 118	Foil	20.84	8.10
TC 206		↓	1.25	TC 224		22.95	10.35
SG 104	Foil	18.11	9.10	TC 226		↓	8.35
TC 208		18.28	8.80	SG 1006	Weldable	↓	8.60
SG 1002	Weldable	18.11	8.60	SG 120	Foil	↓	8.10
SG 106	Foil		8.10	TC 228		↓	6.60
TC 210			7.70	TC 230		↓	1.25
SG 108	Foil		6.60	TC 232		25.64	6.60
TC 212			6.35	TC 234		33.17	8.85
SG 110	Foil		4.10	SG 1008	Weldable	↓	8.60
TC 214			3.35	SG 122	Foil	↓	8.10
SG 130	Foil		4.60	TC 236		↓	6.60
SG 132	Foil		3.60	TC 238		↓	2.60
TC 214B		↓	4.85	TC 240		40.70	6.60
TC 216		19.11	8.85	TC 242		43.39	10.35
SG 112	Foil	↓	8.60	TC 244		43.39	6.60
^a SG 114	Foil	↓	8.10	TC 246		43.39	1.25
SG 116	Foil	↓	6.60	TC 248		60.20	8.60
TC 220		↓	6.35	TC 250		60.20	6.60
TC 218		19.51	8.10	TC 252		60.20	1.25

^aTransverse strain gage.

Table III. Test Sequence

Test group	Combined-load cycle	Applied mechanical load at each load point, lbf, for	
		Ascent ^a	Entry
Panel 1			
1	Mechanical only	980	206
1	Thermal only	0	0
1	1	980	206
2	2 50	980	206
3	51 100	980	206
4	101 200	980	206
5	201 300	980	206
6	301 500	980	206
7	501 531	2060	
8	532	^{b,c} 3300	
Panel 2			
1	Mechanical only	980 and 1575	
1	Thermal only	0	
2	1-5	980	
3	6 82	1575	
4	83-152	2025	
5	153-177	^b 2475	
6	178 202	^b 2700	
7	203-227	^b 2925	
8	228-252	^b 3267	
9	253	^d 4945	
10	254	^d 5003	

^aAscent cycles occurred before entry cycles in each test group.

^bExceeded proportional limit at support.

^cFailed by core crushing.

^dExceeded yield at support.

Table IV. Material and Geometric Properties for Finite-Element Analysis

(a) Material properties of René 41

[From ref. 13]

$T, ^\circ\text{F}$	$E, \text{ lbf/in}^2$	$G, \text{ lbf/in}^2$	$\alpha, \text{ in/in-}^\circ\text{F}$ (from 70°F)
-320	31.6×10^6	12.2×10^6	5.7×10^{-6}
350	30.2	11.5	6.7
500	29.3	11.2	6.9
900	27.1	10.4	7.5
1090	25.9	10.0	7.8
1350	23.4	9.5	8.2

(b) Geometric properties

[Element stiffnesses are based on these dimensions. However, the extensional stiffnesses in the x - y plane for core elements were arbitrarily reduced by a factor of 1000 to simulate the small stiffness of the honeycomb core.]

t_{ef} (except at pads), in.	0.020
t_{ef} (at pads), in.	0.025
$^a t_{ec}$, in:	
$P_c = 1.50$ in.	0.012
$P_c = 1.25$ in.	0.010
$P_c = 0.75$ in.	0.006
$P_c = 0.50$ in.	0.004

$^a t_{ec} = (t_c/P_c)P_c$, where $t_c = 0.0015$ in.; $P_c = 0.1875$ in., and P_c is determined from figure 19.

Table V. Measured Temperatures for Finite-Element Analyses
[See fig. 19]

(a) Outer face sheet

Node	Temperature, °F, on panel 1 for				Temperature, °F, on panel 2 for ascent cycle 81 at $t = 120$ sec
	Ascent cycle 1 at $t = 120$ sec	Ascent cycle 500 at $t = 120$ sec	Entry cycle 500 at $t = 230$ sec	Entry cycle 500 at $t = 1490$ sec	
1	400	375	1010	1360	420
3	400	350	980	1350	440
5	480	360	930	1335	470
7	460	375	820	1290	465
9	360	350	740	1200	430
11	430	390	1040	1380	420
13	440	365	990	1350	440
15	480	340	920	1340	470
17	450	345	850	1300	450
19	360	350	760	1200	415
21	430	400	1050	1400	415
23	440	380	1000	1390	440
25	480	345	960	1360	450
27	440	330	870	1310	440
29	360	345	770	1220	400
31	420	415	1060	1420	400
33	420	380	1010	1400	420
35	460	365	940	1380	430
37	420	360	870	1320	430
39	340	320	780	1210	380
41	420	420	1070	1420	380
43	420	385	1010	1400	380
45	440	365	950	1380	400
47	410	350	860	1310	400
49	320	305	780	1200	350
51	400	425	1070	1400	360
53	400	385	1010	1390	360
55	420	355	940	1360	370
57	380	340	860	1300	375
59	300	300	780	1200	330
61	380	425	1060	1380	330
63	380	380	990	1375	320
65	400	340	910	1340	325
67	340	330	840	1295	340
69	260	300	760	1180	300
71	360	385	1050	1370	295
73	360	360	980	1350	285

Table V. Continued

(a) Continued

Node	Temperature, °F, on panel 1 for—				Temperature, °F, on panel 2 for ascent cycle 81 at $t = 120$ sec
	Ascent cycle 1 at $t = 120$ sec	Ascent cycle 500 at $t = 120$ sec	Entry cycle 500 at $t = 230$ sec	Entry cycle 500 at $t = 1490$ sec	
75	360	310	900	1320	280
77	300	305	830	1270	300
79	220	270	730	1150	280
81	300	305	1020	1320	260
83	300	255	950	1350	250
85	320	210	860	1300	245
87	240	275	760	1240	260
89	150	250	650	1120	240
91	240	235	980	1290	225
93	250	205	870	1300	215
95	240	175	770	1260	215
97	160	225	660	1200	220
99	80	210	550	1060	↓
101	260	220	930	1265	
103	260	190	850	1270	
105	230	150	740	1210	
107	200	210	620	1160	210
109	140	190	500	1050	210
111	290	225	930	1240	205
113	320	185	830	1260	210
115	290	150	730	1220	200
117	240	210	610	1160	210
119	200	185	490	1070	200
121	320	220	930	1270	210
123	350	190	850	1280	210
125	320	150	740	1240	200
127	280	210	620	1170	220
129	230	190	500	1080	200
131	330	235	980	1300	230
133	360	205	870	1300	230
135	330	175	770	1260	225
137	360	225	660	1190	220
139	240	210	550	1120	205
141	340	320	1020	1350	280
143	360	270	950	1340	270
145	340	210	860	1290	250
147	310	270	760	1240	260
149	260	235	650	1150	245
151	360	380	1050	1400	325

Table V. Continued

(a) Continued

Node	Temperature, °F, on panel 1 for—				Temperature, °F, on panel 2 for ascent cycle 81 at $t = 120$ sec
	Ascent cycle 1 at $t = 120$ sec	Ascent cycle 500 at $t = 120$ sec	Entry cycle 500 at $t = 230$ sec	Entry cycle 500 at $t = 1490$ sec	
153	380	335	900	1360	300
155	360	275	900	1320	390
157	340	300	830	1260	300
159	280	265	730	1160	370
161	380	400	1060	1400	355
163	380	370	990	1390	340
165	380	320	910	1340	320
167	360	325	840	1280	335
169	300	290	760	1170	300
171	380	410	1070	1400	370
173	400	380	1010	1400	360
175	400	340	940	1370	345
177	360	335	860	1280	355
179	300	305	780	1190	320
181	380	410	1070	1410	390
183	440	380	1010	1410	370
185	400	350	950	1360	360
187	360	345	860	1290	360
189	300	315	780	1180	320
191	400	410	1070	1390	390
193	400	385	1010	1400	380
195	400	350	950	1360	365
197	360	350	860	1280	360
199	260	320	780	1160	365
201	380	410	1060	1380	390
203	390	385	1010	1380	370
205	380	355	950	1340	355
207	330	350	860	1260	345
209	220	325	780	1140	300
211	340	405	1050	1350	370
213	340	385	1010	1340	350
215	330	355	940	1300	335
217	280	350	860	1220	330
219	180	335	780	1100	280
221	300	410	1030	1300	340
223	300	395	990	1300	330
225	260	360	930	1250	315
227	220	355	840	1170	310

Table V. Continued

(a) Concluded

Node	Temperature, °F, on panel 1 for				Temperature, °F, on panel 2 for ascent cycle 81 at $t = 120$ sec
	Ascent cycle 1 at $t = 120$ sec	Ascent cycle 500 at $t = 120$ sec	Entry cycle 500 at $t = 230$ sec	Entry cycle 500 at $t = 1490$ sec	
229	120	340	770	1040	360
231	220	405	1000	1240	315
233	220	390	970	1240	300
235	200	360	920	1200	280
237	160	340	830	1110	280
239	80	335	760	980	230
241	120	405	970	1180	300
243	140	390	940	1140	280
245	90	360	890	1070	270
247	90	355	820	1040	250
249	80	350	730	920	200

Table V. Continued

(b) Inner face sheet

Node	Temperature, °F, on panel 1 for—				Temperature, °F, on panel 2 for ascent cycle 81 at $t = 120$ sec
	Ascent cycle 1 at $t = 120$ sec	Ascent cycle 500 at $t = 120$ sec	Entry cycle 500 at $t = 230$ sec	Entry cycle 500 at $t = 1490$ sec	
2	-270	-285	590	1040	-285
4	-270	-275	560	1020	-275
6	-300	-240	520	1000	-240
8	-310	-240	450	990	-240
10	-320	-240	390	950	-240
12	-285	-275	590	1040	-275
14	-285	-250	570	1035	-250
16	-285	-230	520	1010	-230
18	-310	-240	460	1000	-240
20	-320	-240	420	935	-240
22	-300	-265	600	1040	-265
24	-300	-250	590	1040	-250
26	-290	-230	540	1040	-230
28	-310	-240	480	1020	-240
30	-320	-250	430	940	-250
32	-305	-270	610	1050	-270
34	-305	-255	590	1040	-255
36	-290	-235	540	1040	-235
38	-310	-240	480	1020	-240
40	-320	-255	430	940	-255
42	-310	-275	590	1040	-275
44	-310	-270	580	1040	-270
46	-290	-245	530	1035	-245
48	-320	-260	490	1020	-260
50	-320	-270	430	940	-270
52	-315	-290	590	1050	-290
54	-310	-290	570	1050	-290
56	-285	-280	530	1040	-280
58	-315	-280	470	1000	-280
60	-320	-280	430	920	-280
62	-315	-300	580	1040	-300
64	-310	-295	570	1040	-295
66	-280	-280	510	1040	-280
68	-310	-285	470	1000	-285
70	-320	-300	430	920	-300
72	-310	-315	560	1050	-315
74	-310	-300	540	1040	-300
76	-280	-300	500	1040	-300
78	-310	-310	450	980	-310
80	-320	-320	420	910	-320

Table V. Continued

(b) Continued

Node	Temperature, °F, on panel 1 for—				Temperature, °F, on panel 2 for ascent cycle 81 at $t = 120$ sec
	Ascent cycle 1 at $t = 120$ sec	Ascent cycle 500 at $t = 120$ sec	Entry cycle 500 at $t = 230$ sec	Entry cycle 500 at $t = 1490$ sec	
82	-305	-320	540	1050	-320
84	-305	-310	520	1030	-310
86	-295	-310	480	1020	-310
88	-320	-320	430	970	-320
90	-320		380	950	
92	-305		510	1040	
94	-300		490	1010	
96	-295		470	980	
98	-320		390	940	
100	-320		350	860	
102	-310		490	1020	
104	-305		480	1000	
106	-300		450	980	
108	-320		370	950	
110	-320		310	840	
112	-320		480	1000	
114	-310		470	980	
116	-300		440	960	
118	-320		370	910	
120			300	840	
122			490	990	
124	↓		480	980	
126	-300		450	960	
128	-320		370	910	
130	-320		310	840	
132	-320		510	1010	
134	-310		490	1000	
136	-305		470	990	
138	-320		390	940	
140	-320		350	860	
142	-320	-315	540	1040	-315
144	-310	-315	520	1030	-315
146	-295	-310	480	1030	-310
148	-320	-310	430	960	-310
150	-320	-310	380	880	-310
152	-320	-300	560	1060	-300
154	-310	-300	540	1050	-300
156	-300	-270	500	1030	-290

Table V. Continued

(b) Continued

Node	Temperature, °F, on panel 1 for --				Temperature, °F, on panel 2 for ascent cycle 81 at $t = 120$ sec
	Ascent cycle 1 at $t = 120$ sec	Ascent cycle 500 at $t = 120$ sec	Entry cycle 500 at $t = 230$ sec	Entry cycle 500 at $t = 1490$ sec	
158	-320	-300	450	970	-300
160	-320	-305	420	900	-305
162	-310	-290	580	1060	-290
164	-300	-290	570	1060	-290
166	-290	-275	510	1040	-275
168	-320	-290	470	990	-290
170	-320	-290	430	920	-290
172	-300	-290	590	1060	-290
174	-300	-280	570	1060	-280
176	-280	-260	530	1060	-260
178	-320	-280	470	1000	-280
180	-320	-280	430	930	-280
182	-300	-290	590	1060	-290
184	-300	-280	580	1040	-280
186	-280	-250	530	1010	-250
188	-320	-270	490	1000	-270
190	-320	-280	430	920	-280
192	-300	-300	480	1060	-300
194	-300	-280	570	1040	-280
196	-280	-260	550	1040	-260
198	-320	-275	500	1000	-275
200	-320	-300	440	910	-300
202	-300	-310	570	1060	-310
204	-310	-295	570	1040	-295
206	-280	-270	540	1020	-270
208	-320	-280	490	990	-280
210	↓	-310	440	900	-310
212	↓	-315	560	1040	-315
214	↓	-305	560	1020	-305
216	-290	-290	540	1000	-290
218	-320	-305	480	960	-305
220	↓	-320	430	880	-320
222	↓	-320	550	1010	-320
224	↓	-320	550	1000	-320
226	-290	-300	530	980	-300
228	-320	-320	470	930	-320

Table V. Concluded

(b) Concluded

Node	Temperature, °F, on panel 1 for—				Temperature, °F, on panel 2 for ascent cycle 81 at $t = 120$ sec
	Ascent cycle 1 at $t = 120$ sec	Ascent cycle 500 at $t = 120$ sec	Entry cycle 500 at $t = 230$ sec	Entry cycle 500 at $t = 1490$ sec	
230	-320	-320	410	840	-320
232	-320		530	990	
234	-320		5430	980	
236	-300		520	960	
238	-320		450	910	
240			370	800	
242			510	930	
244			510	910	
246	-310		490	900	
248	-320		420	840	
250	-320		340	760	

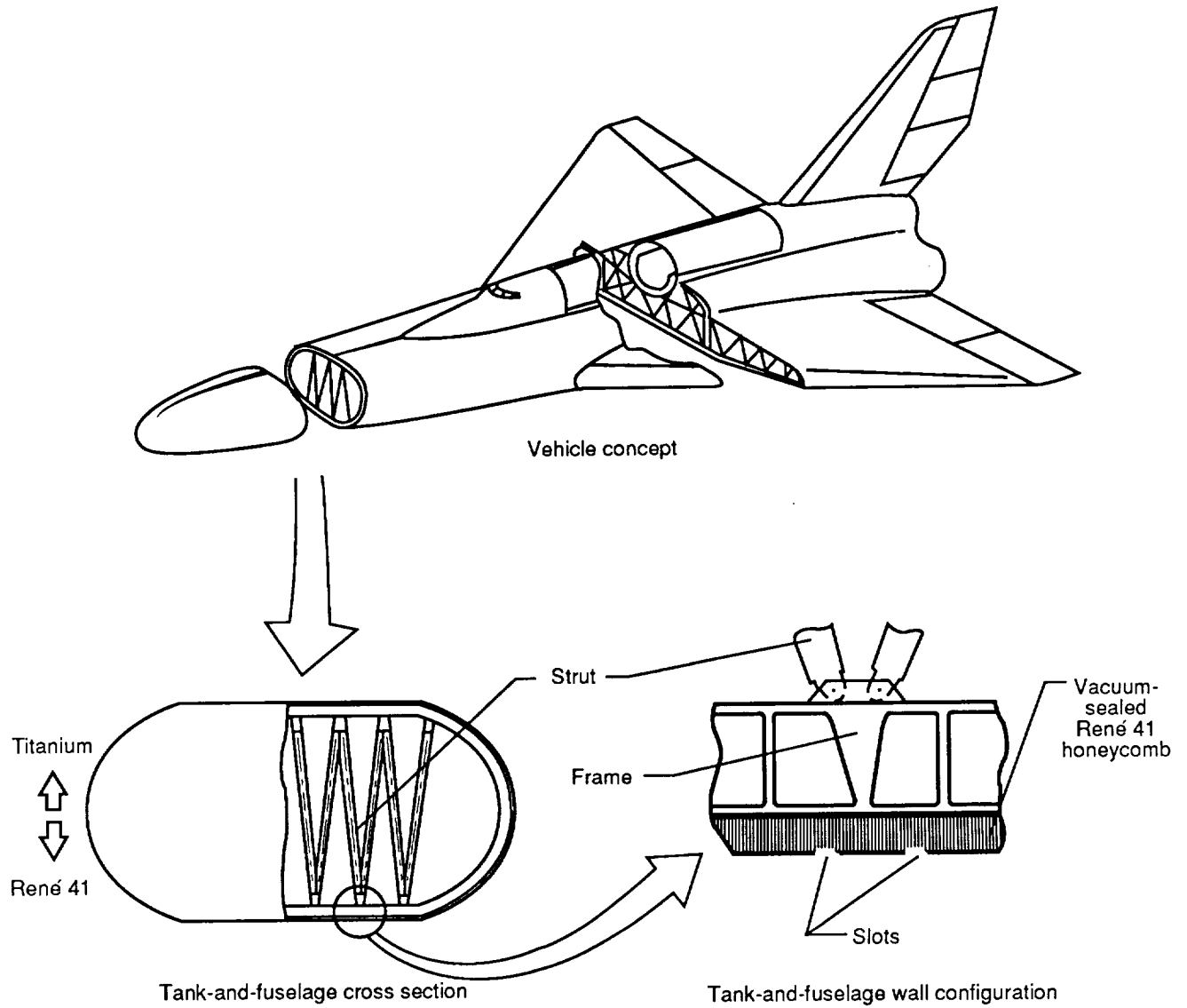


Figure 1. Integral tank-and-fuselage hot-structure concept (from references 6 and 7).

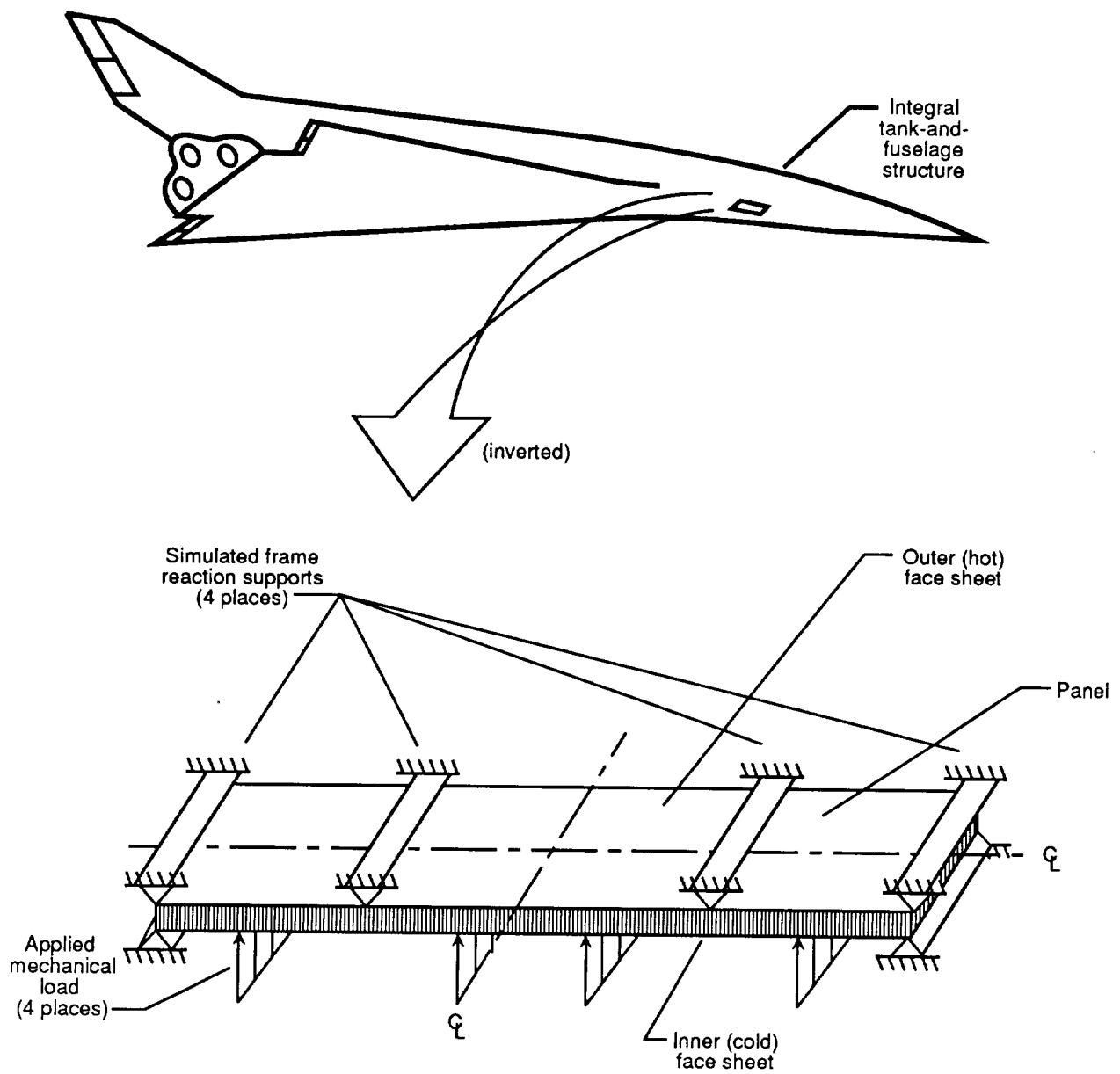


Figure 2. Test concept for 12- by 72-in. honeycomb panel representing section of integral tank-and-fuselage hot structure.

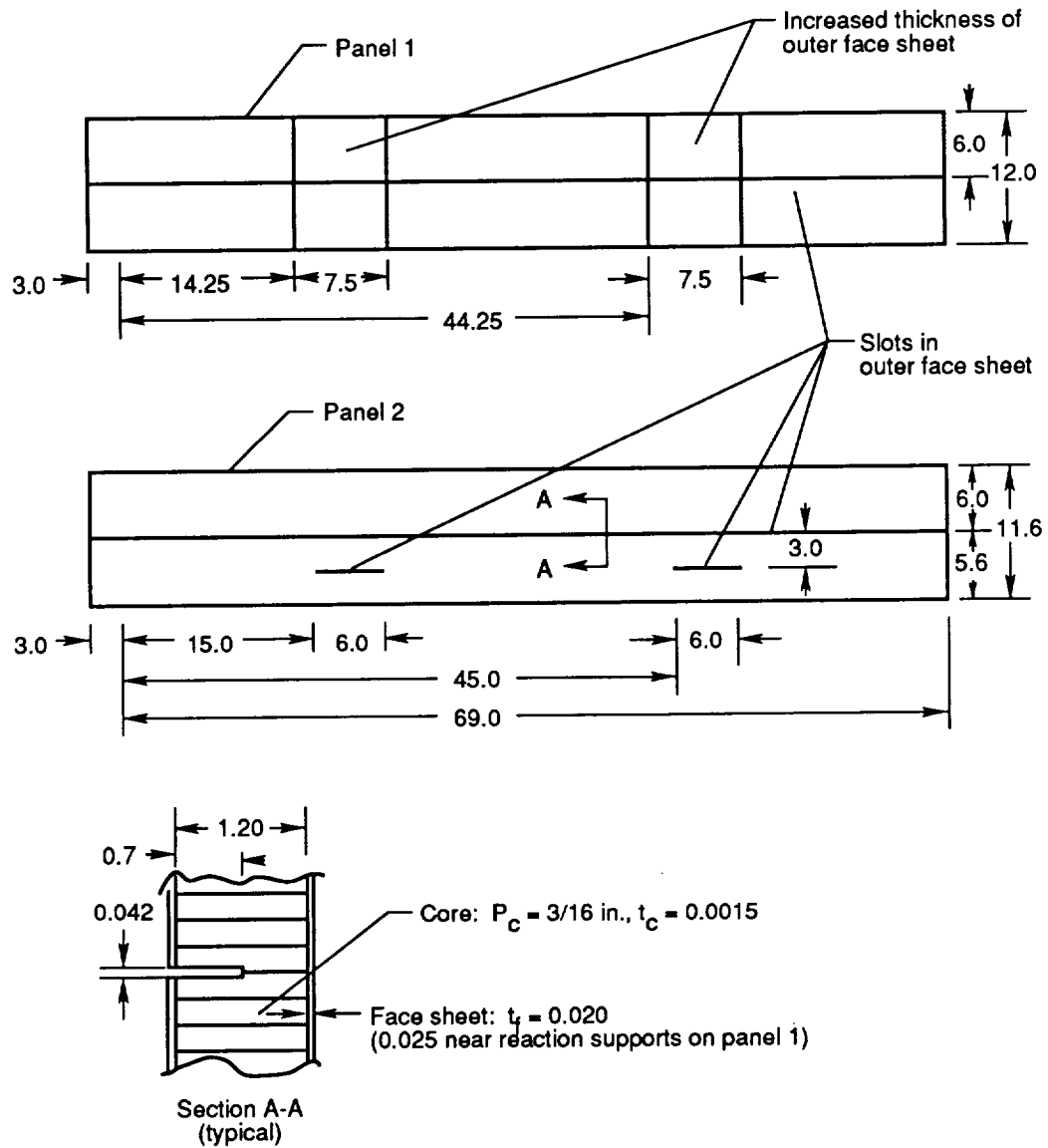
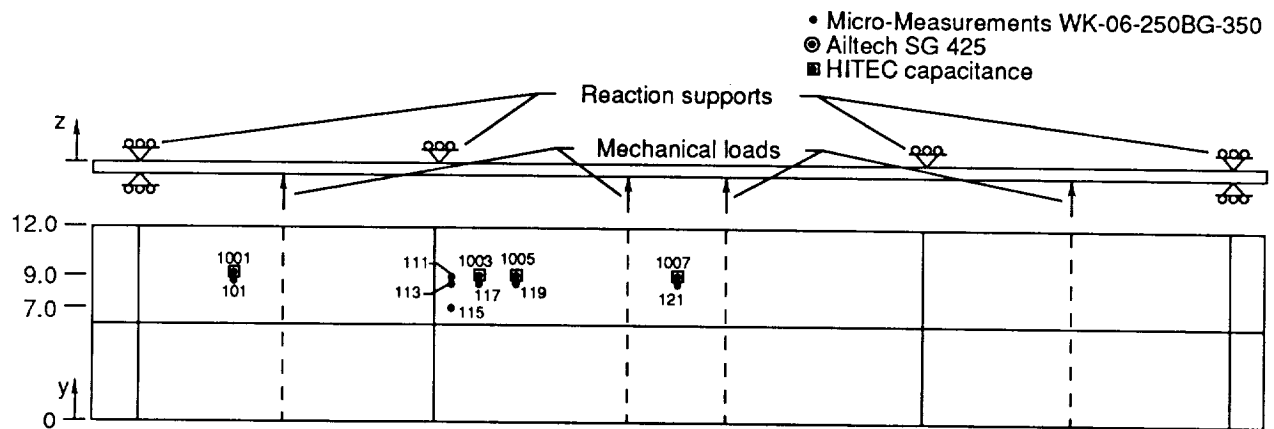
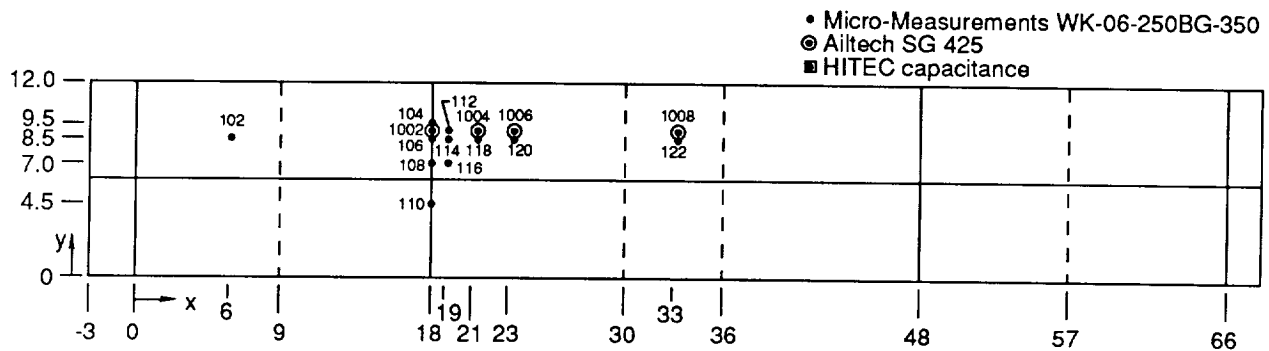


Figure 3. René 41 honeycomb sandwich test panels. Dimensions are in inches.

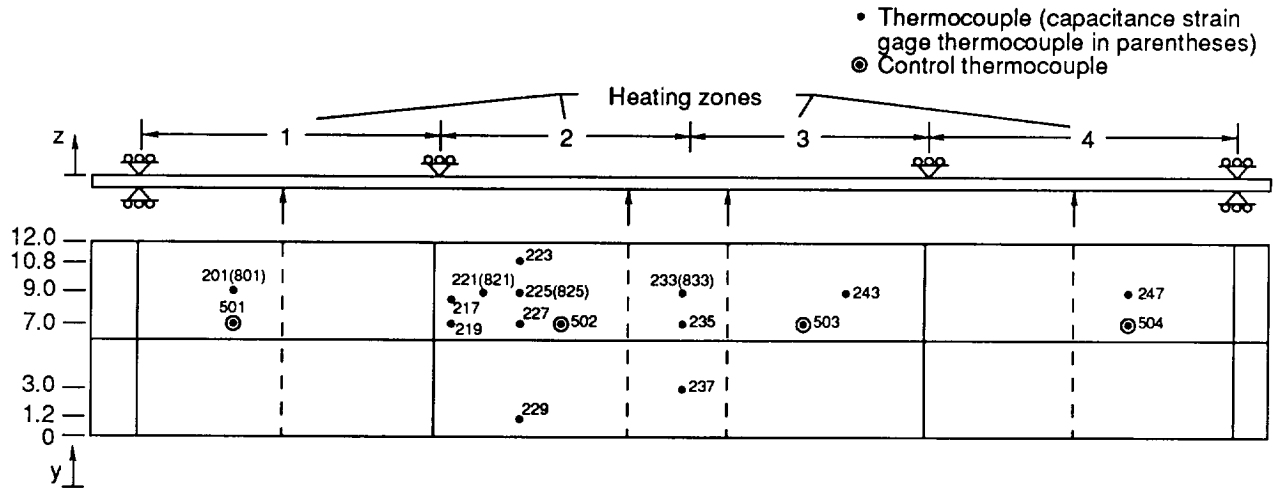


(a) Outer face sheet.

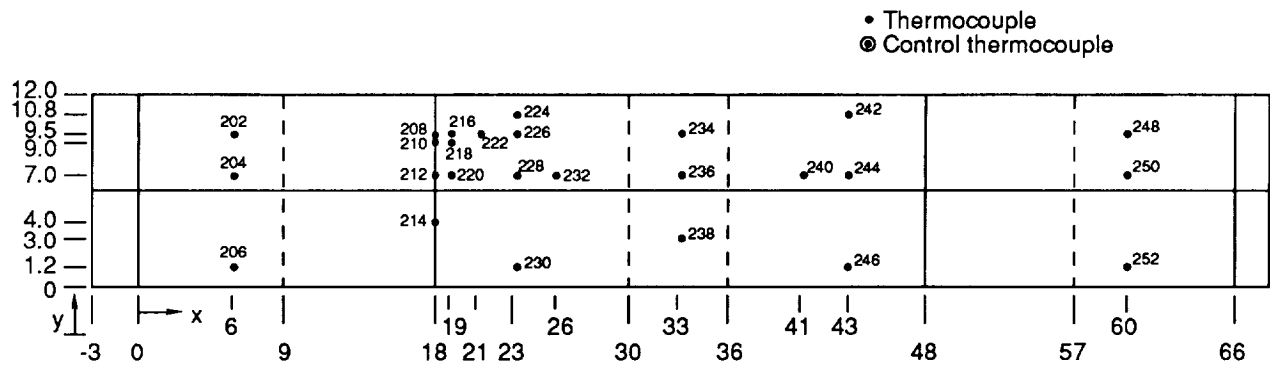


(b) Inner face sheet (viewed through outer face sheet).

Figure 4. Strain gage locations for panel 1. Dimensions are in inches and are approximate. See table I for accurate coordinates.



(a) Outer face sheet.



(b) Inner face sheet (viewed through outer face sheet).

Figure 5. Thermocouple locations for panel 1. Dimensions are in inches and are approximate. See table I for accurate coordinates.

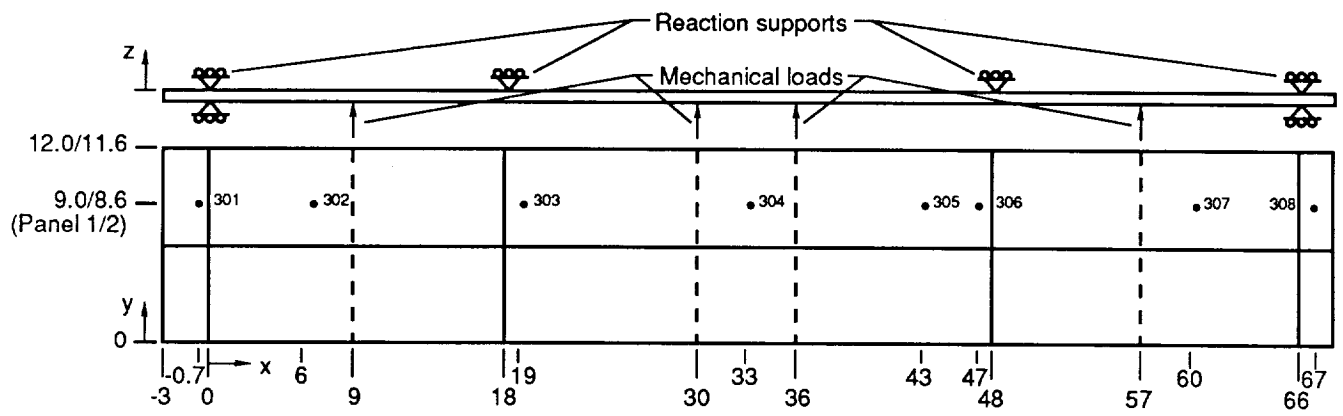
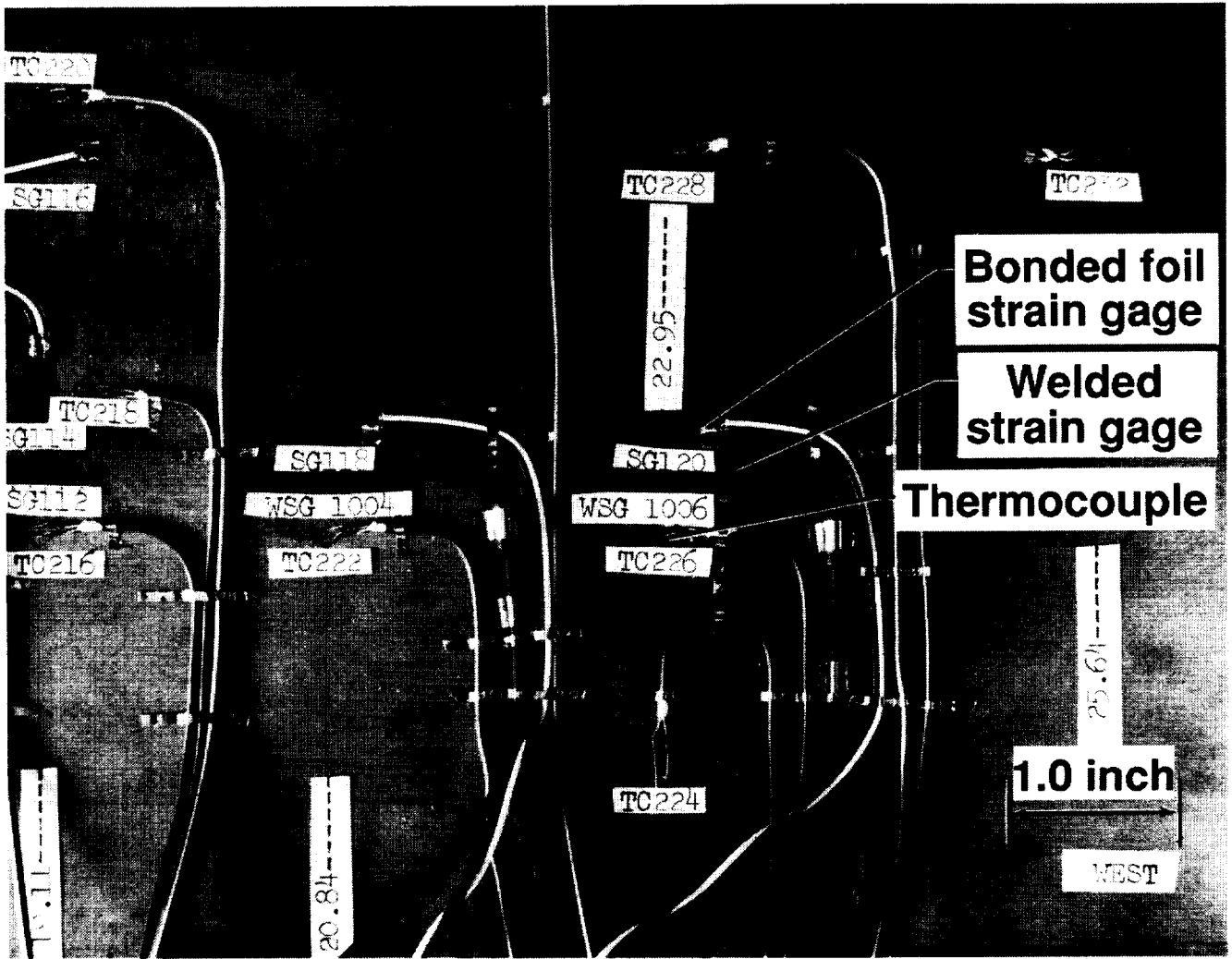


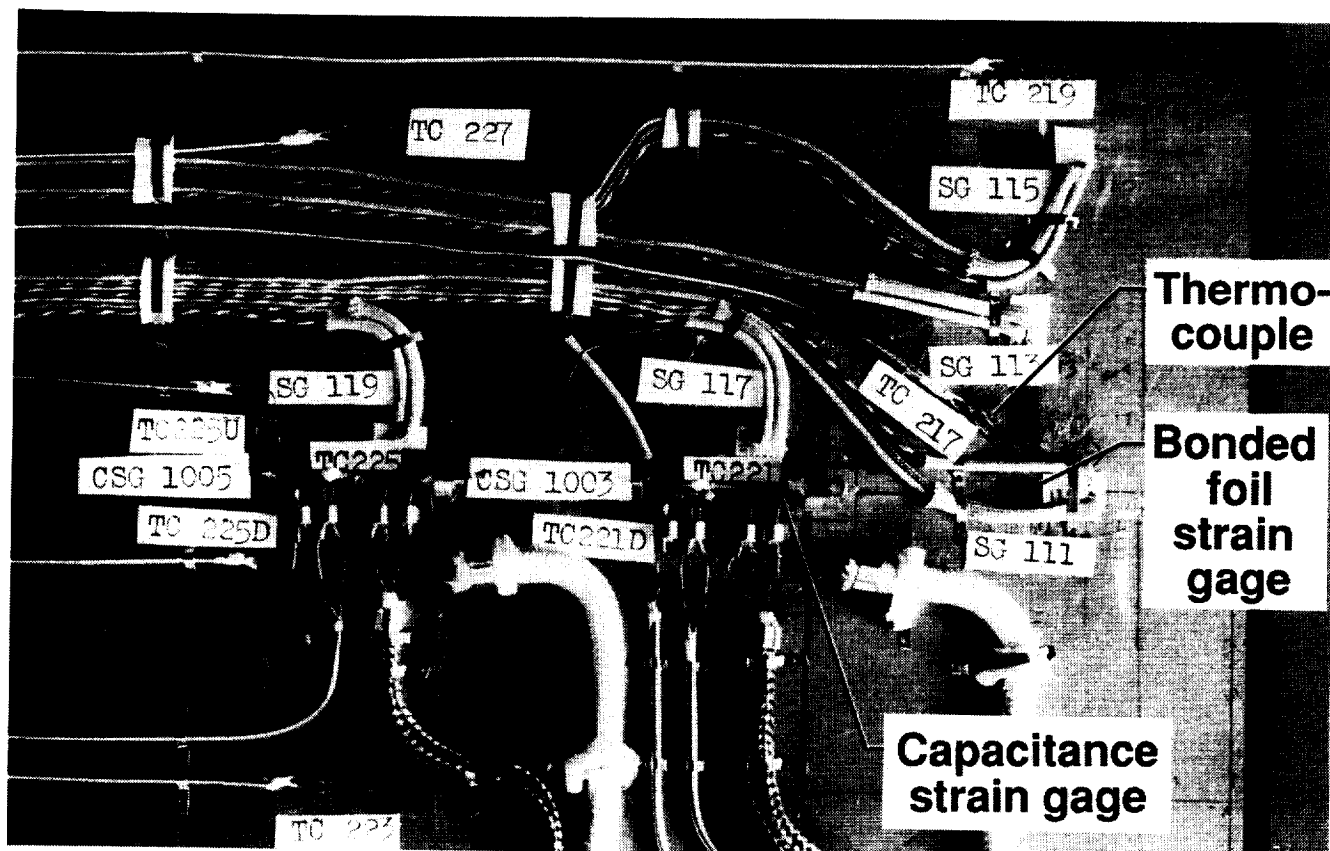
Figure 6. Deflection measurement locations for panels 1 and 2. Dimensions are in inches and are approximate. See tables I and II for accurate coordinates.



E-38396

(a) Inner face sheet.

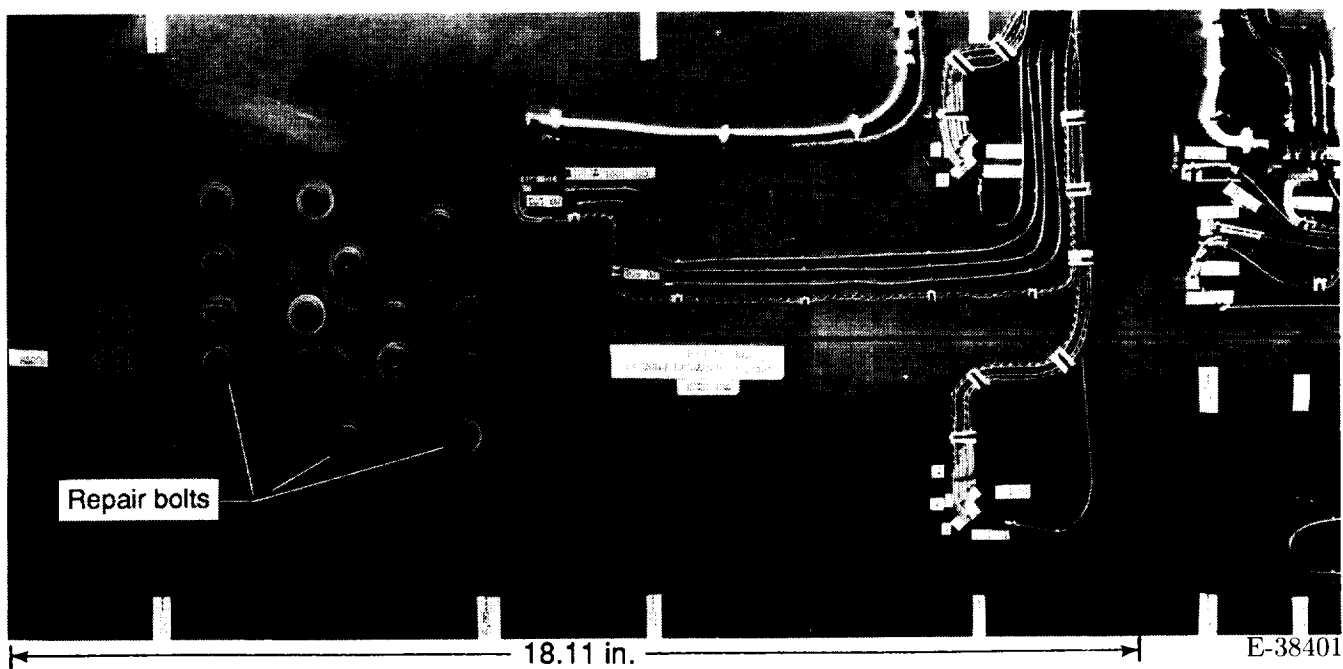
Figure 7. Typical instrumentation.



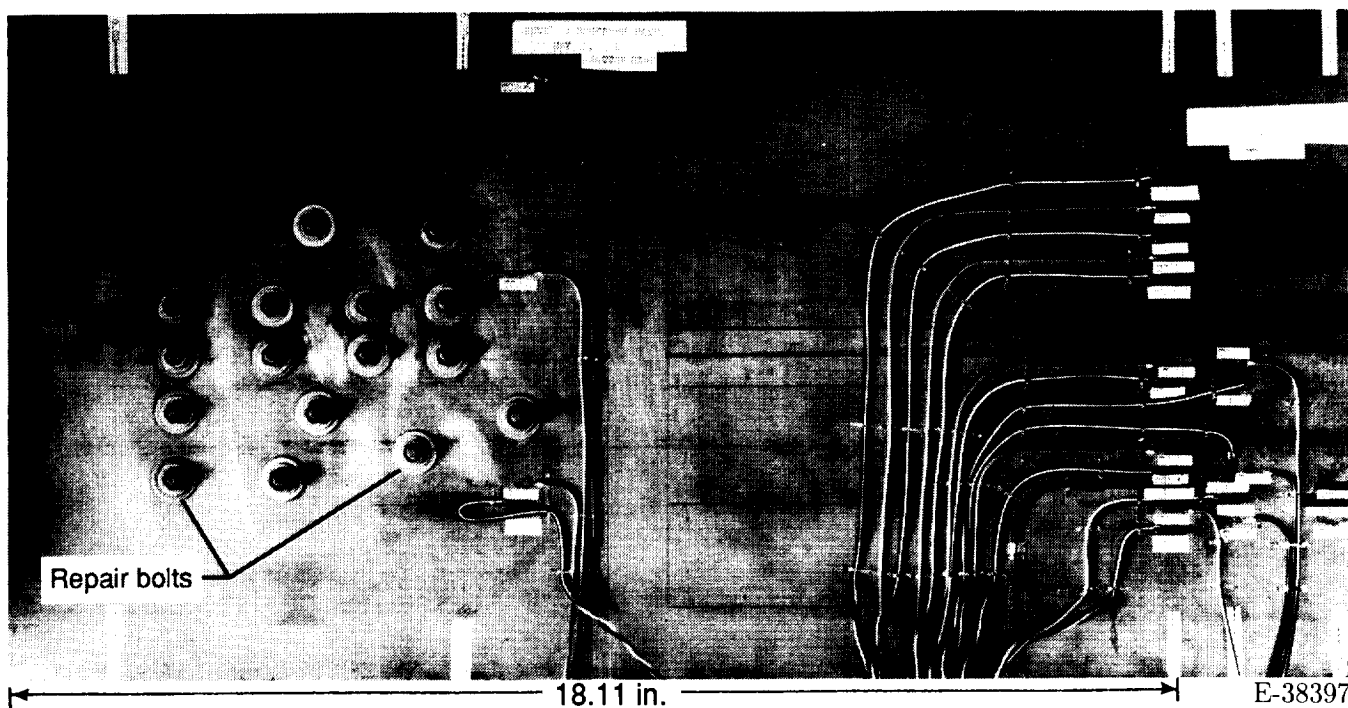
E-38400

(b) Outer face sheet.

Figure 7. Concluded.

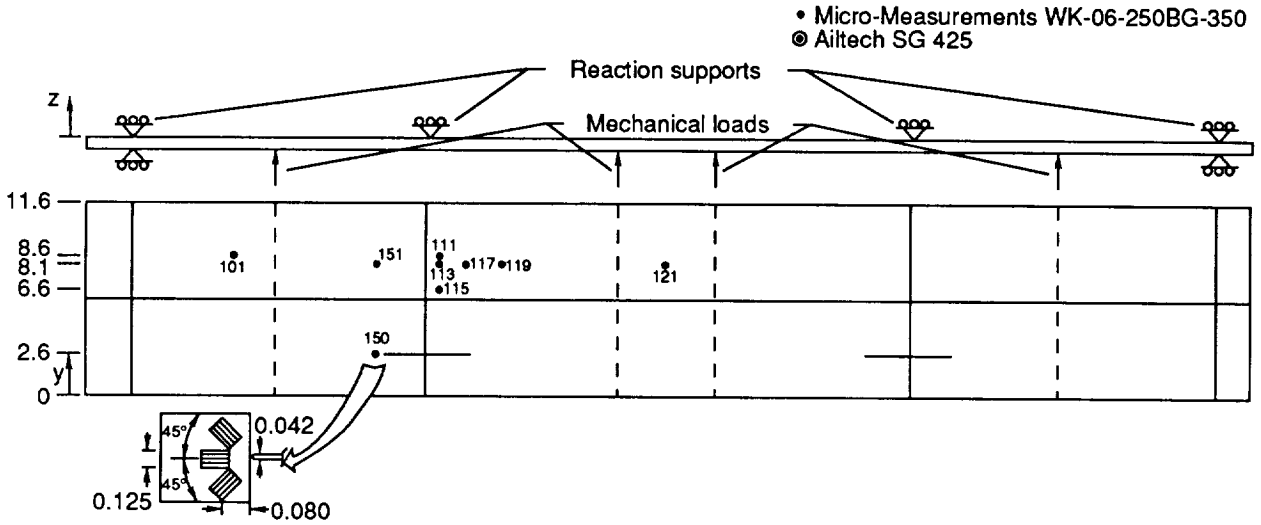


(a) Outer face sheet.

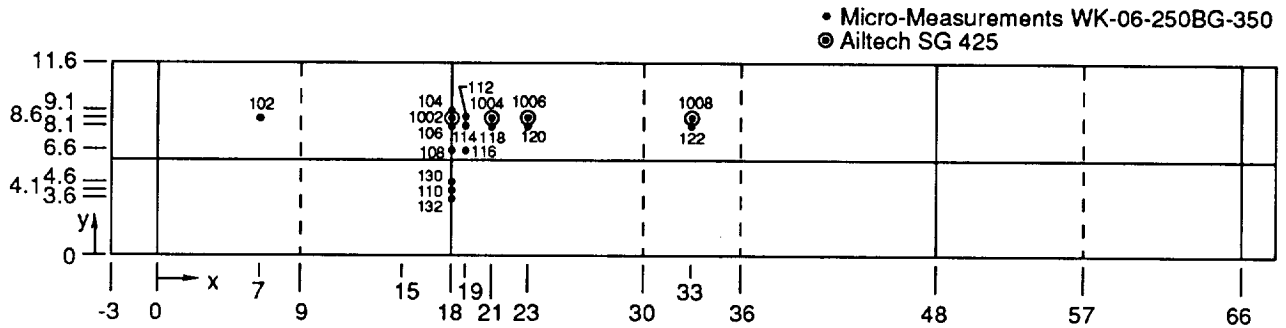


(b) Inner face sheet.

Figure 8. Instrumentation located near reaction support at $x = 18.11$ in.

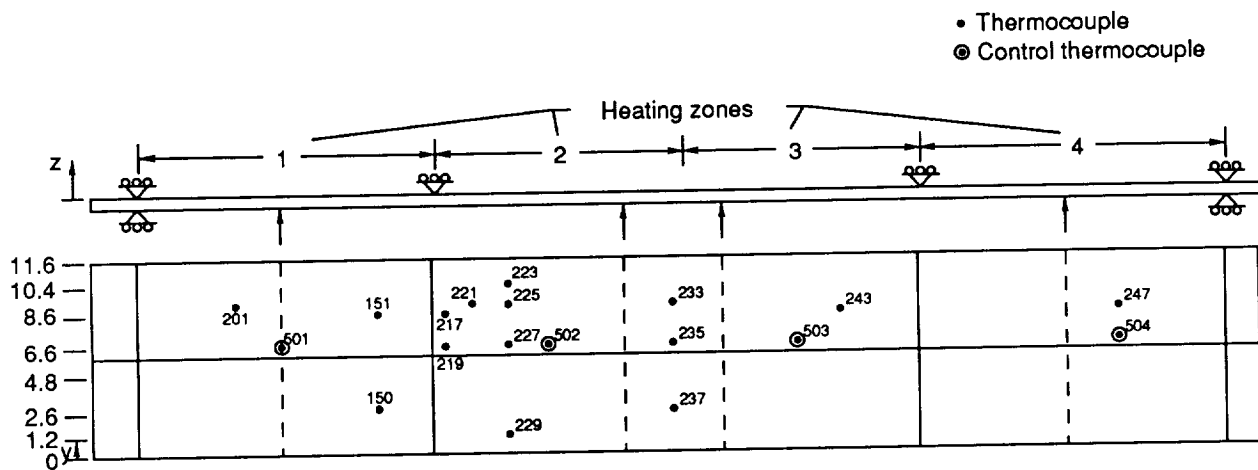


(a) Outer face sheet.

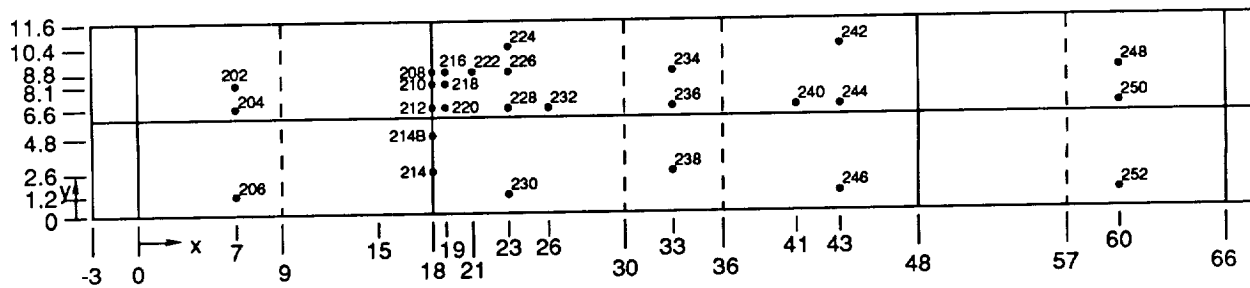


(b) Inner face sheet (viewed through outer face sheet).

Figure 9. Strain gage locations for panel 2. Dimensions are in inches and are approximate. See table II for accurate coordinates.



(a) Outer face sheet.



(b) Inner face sheet (viewed through outer face sheet).

Figure 10. Thermocouple locations for panel 2. Dimensions are in inches and are approximate. See table II for accurate coordinates.

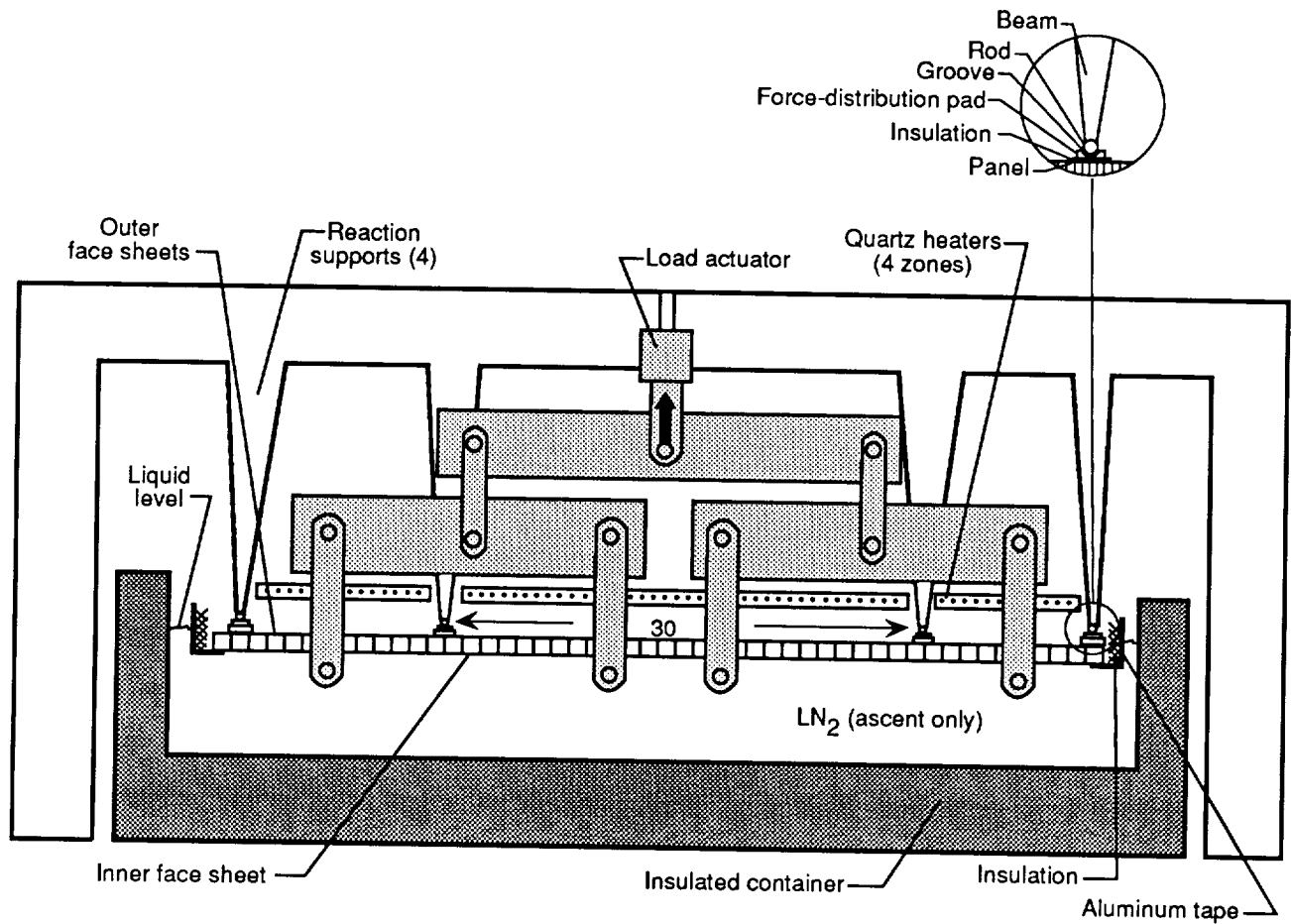
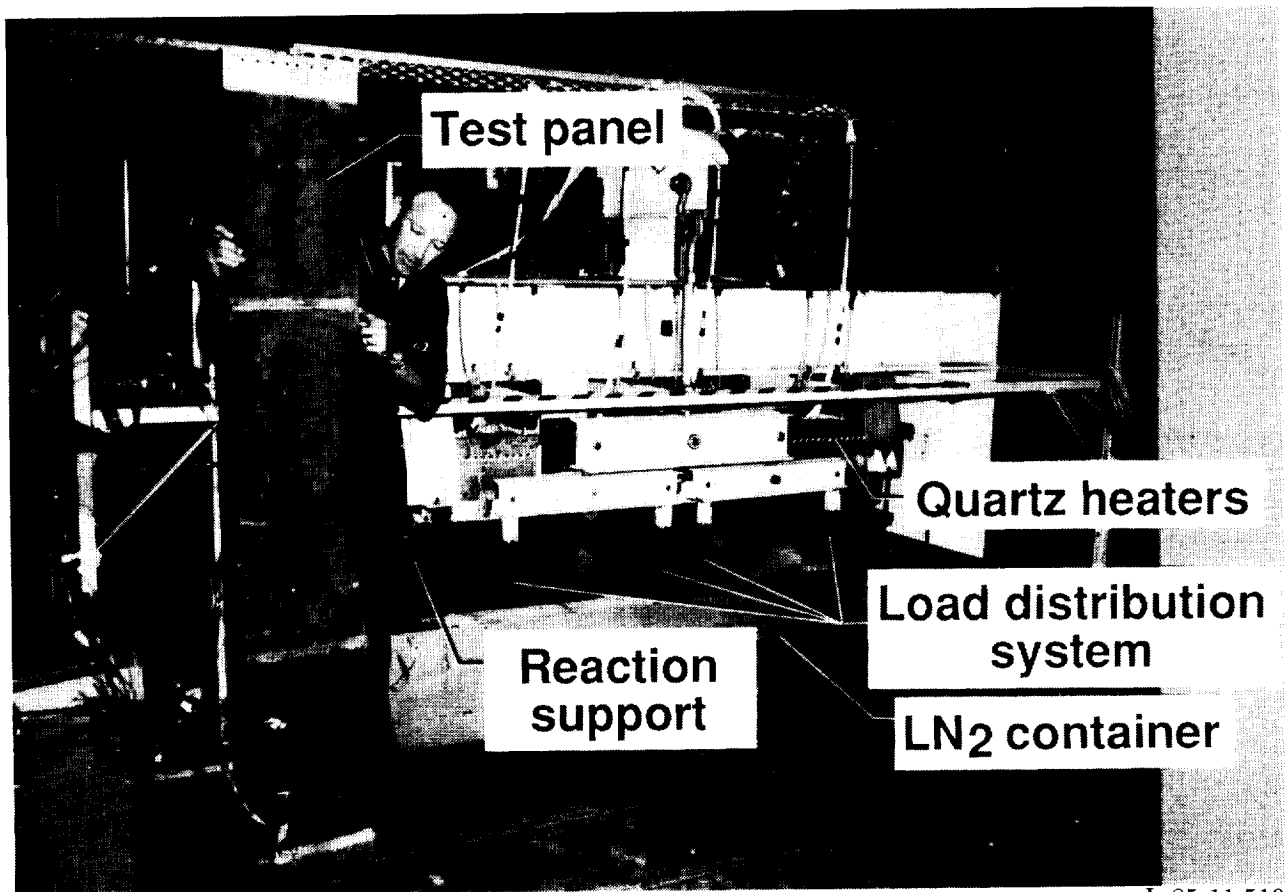
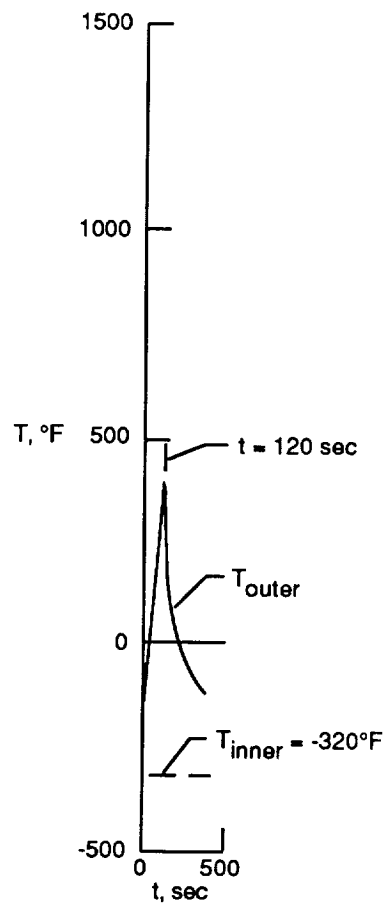


Figure 11. Schematic of combined thermal and mechanical loads test apparatus. Dimensions are in inches.

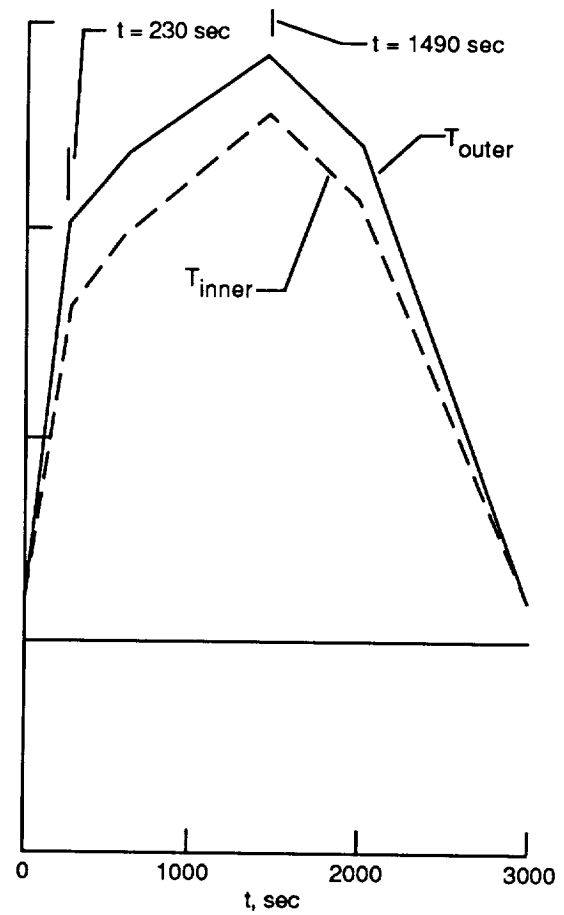


L-85-11,519

Figure 12. Combined-load test apparatus and panel.

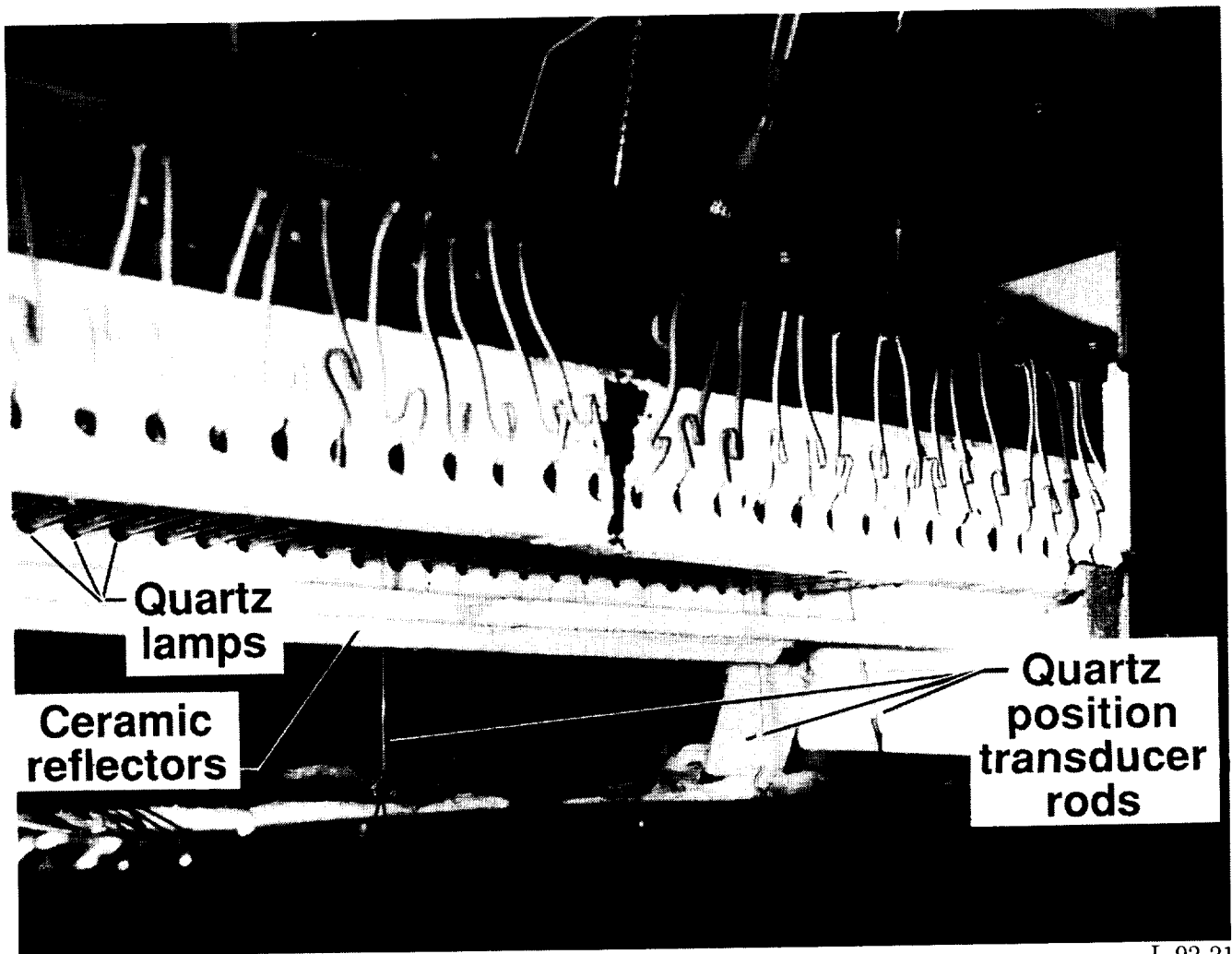


(a) Ascent thermal history.



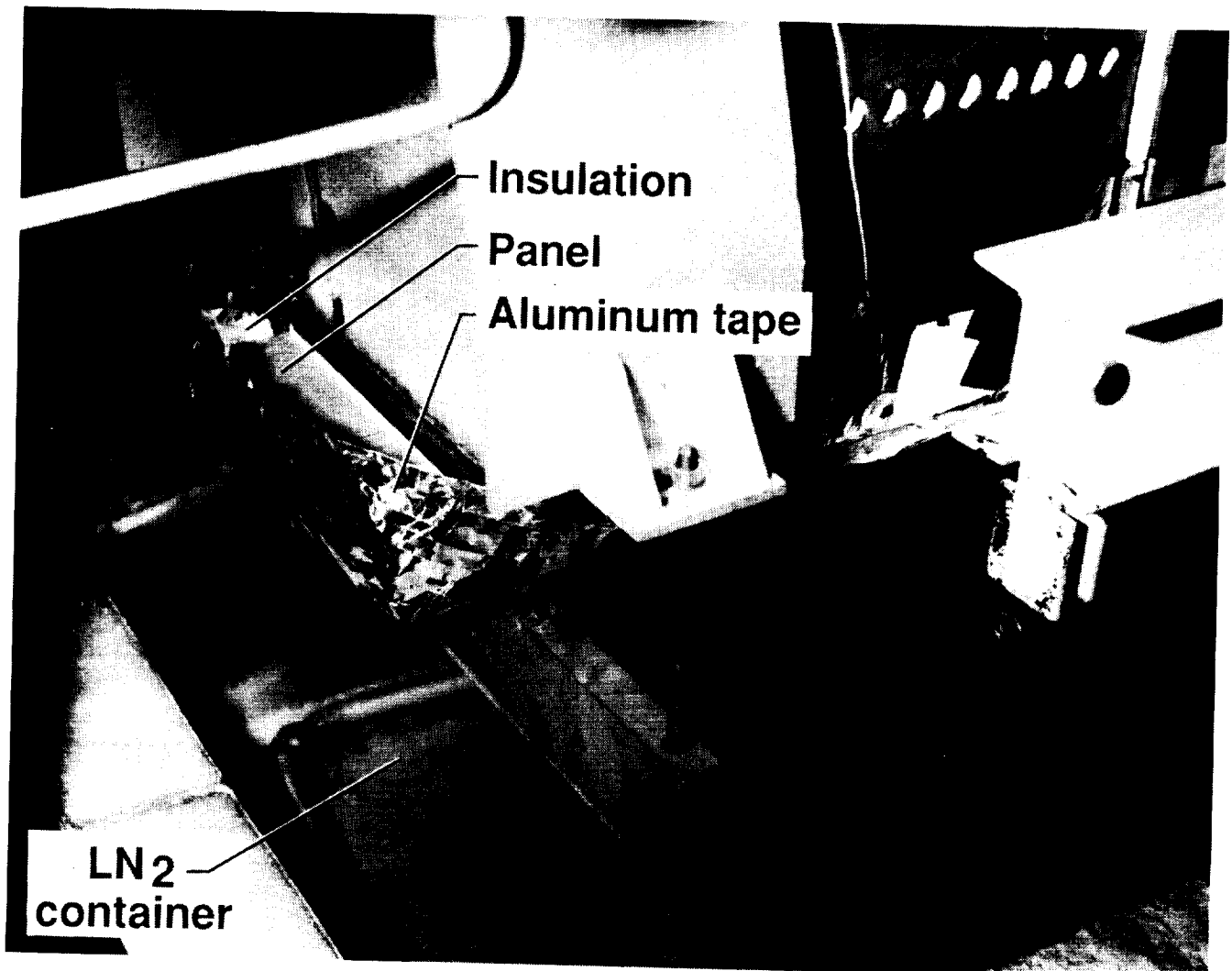
(b) Entry thermal history.

Figure 13. Inner- and outer-face-sheet temperature histories for use in test cycles.



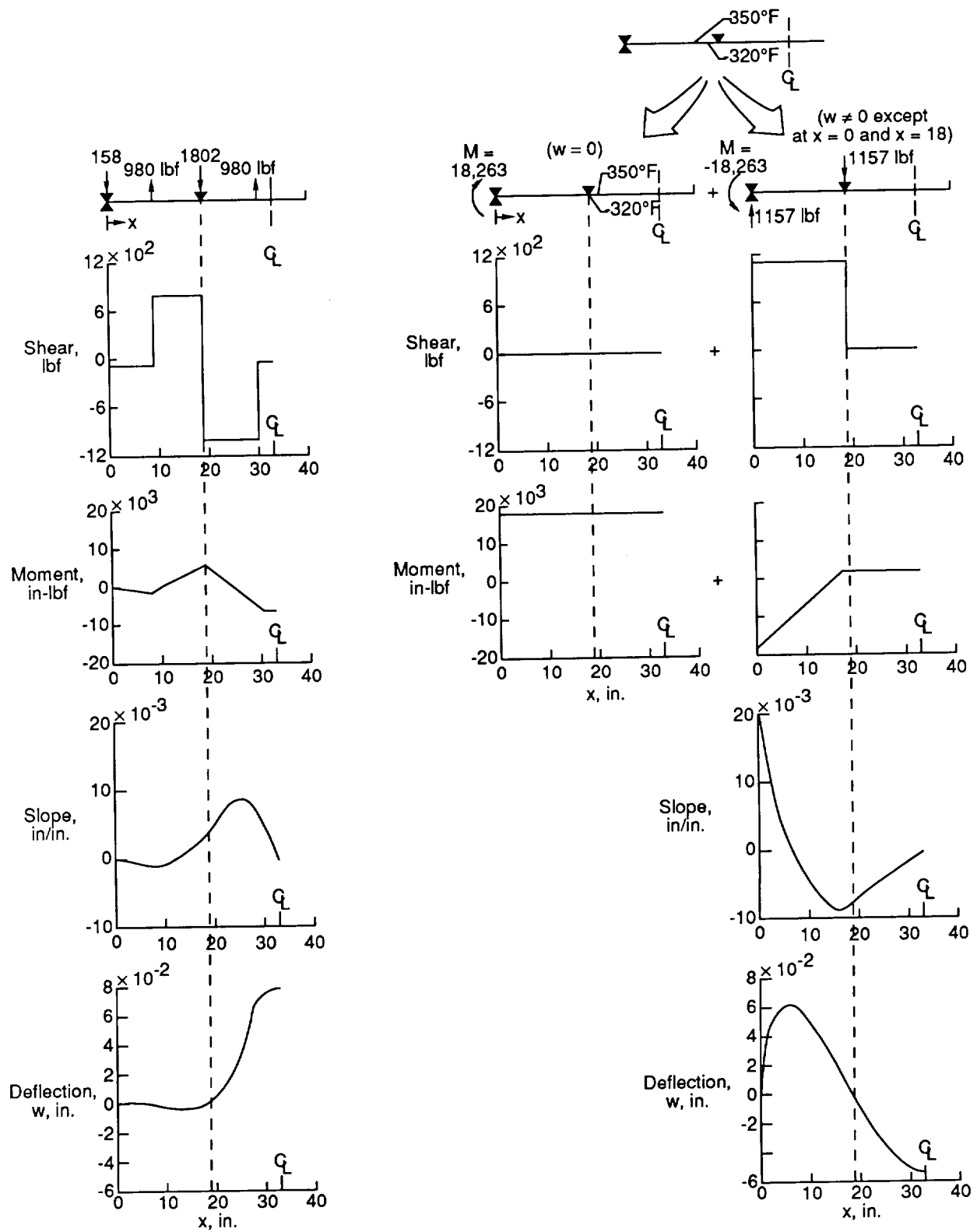
L-92-21

Figure 14. Test setup with mechanical load system removed to show quartz heaters.



L-92-22

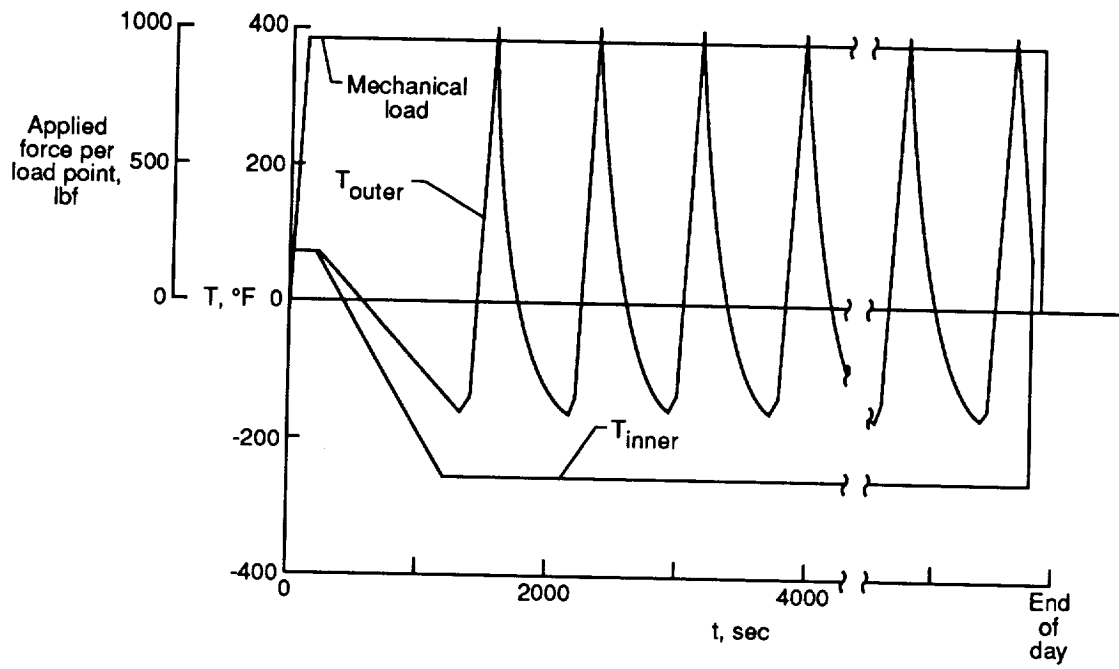
Figure 15. Test panel prior to immersion in liquid nitrogen.



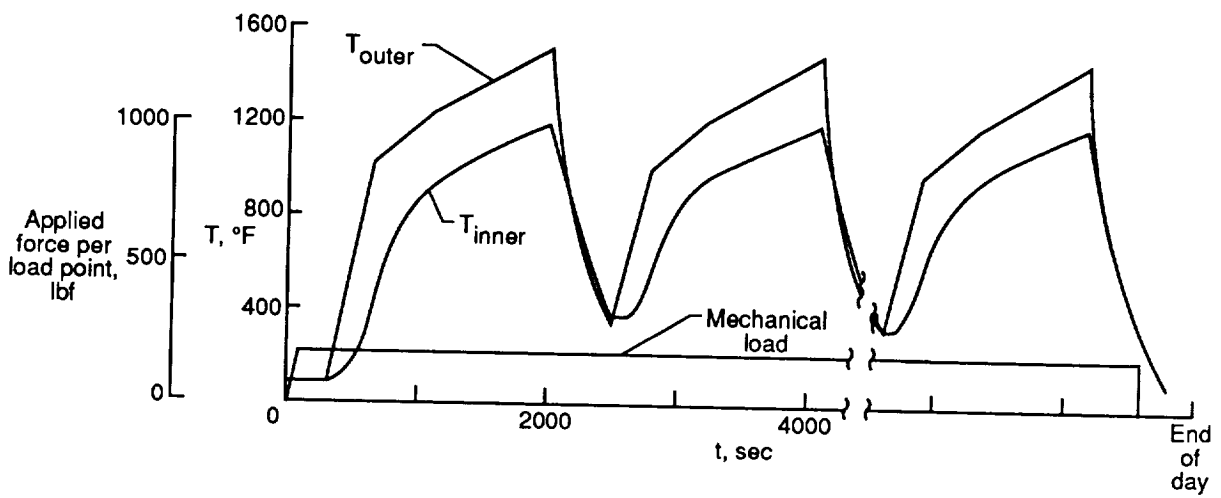
(a) Mechanically applied load.

(b) Thermally applied load.

Figure 16. Typical load, shear, bending moment, slope, and deflection diagrams for ascent cycle of panel 2. Face-sheet thickness, 0.020 in.



(a) Ascent cycles.



(b) Entry cycles.

Figure 17. Typical application sequence of combined loads.

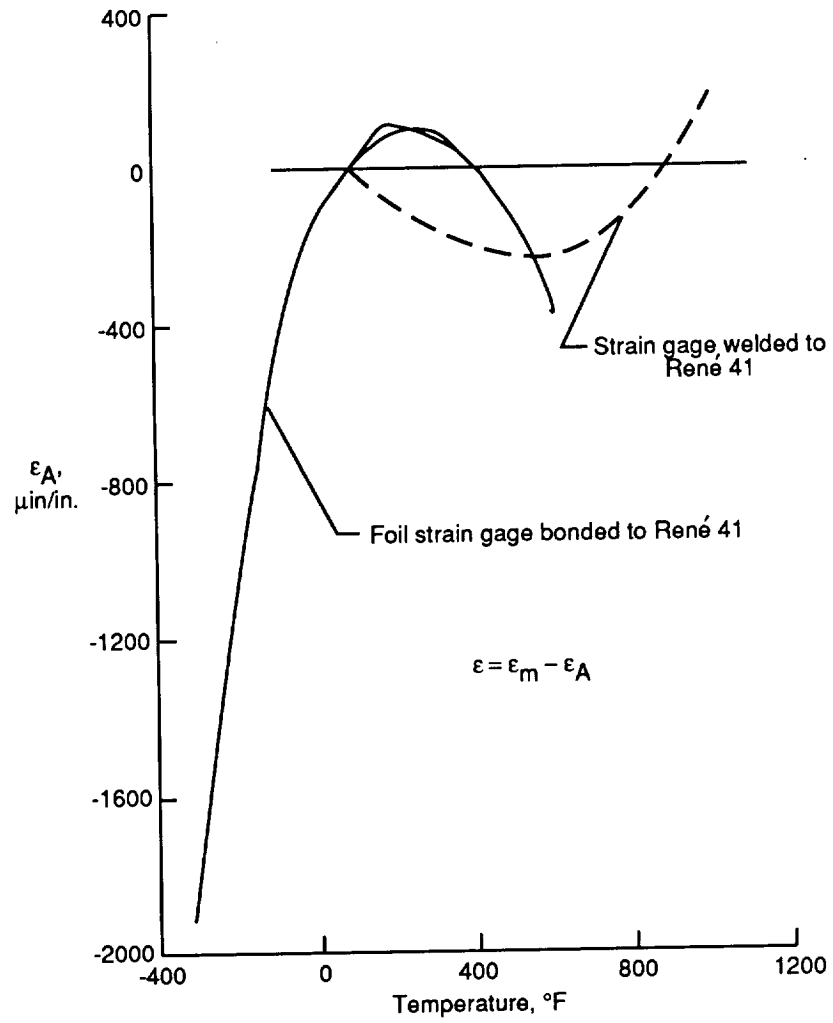


Figure 18. Apparent strain used for correcting measured strain data.

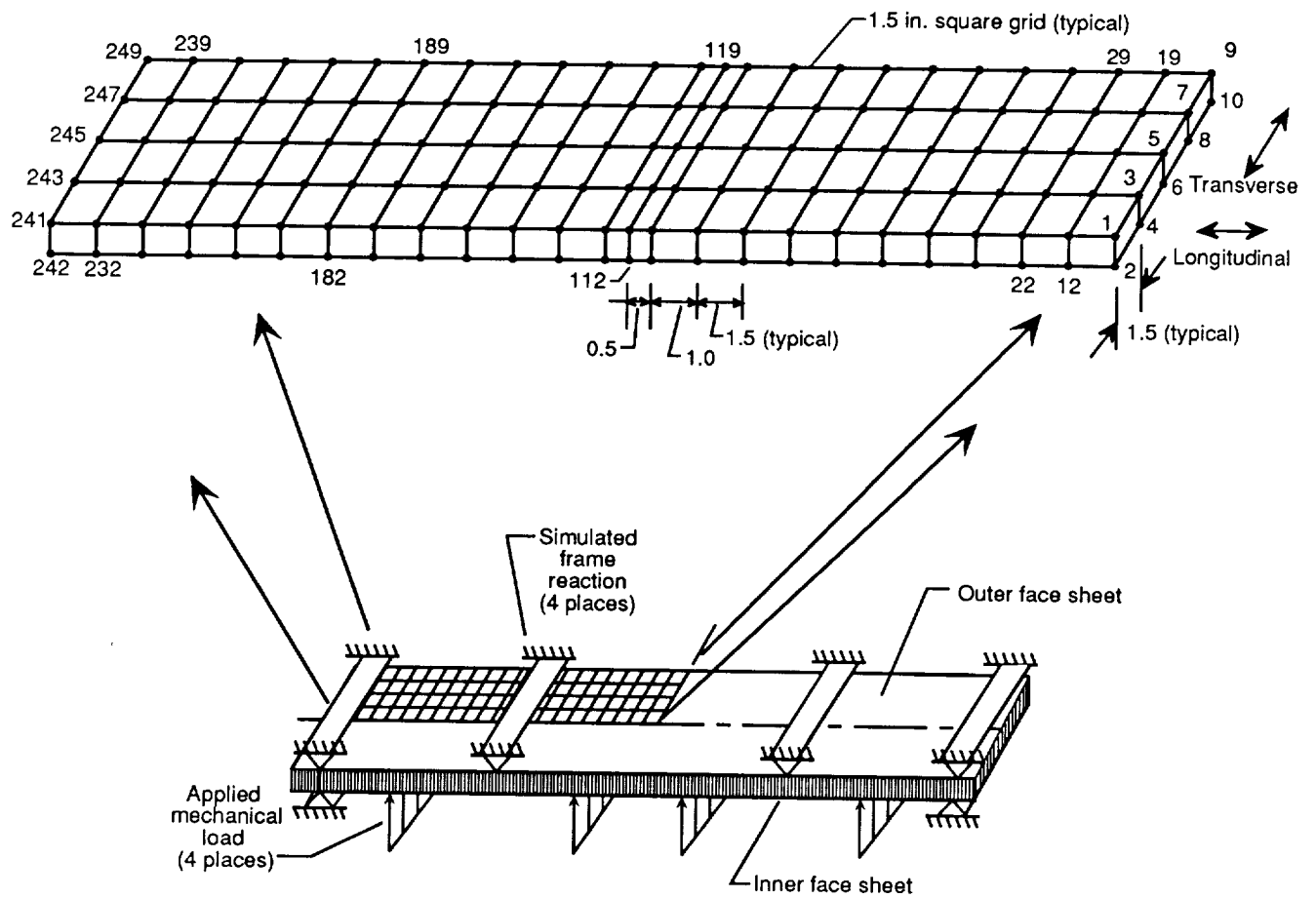
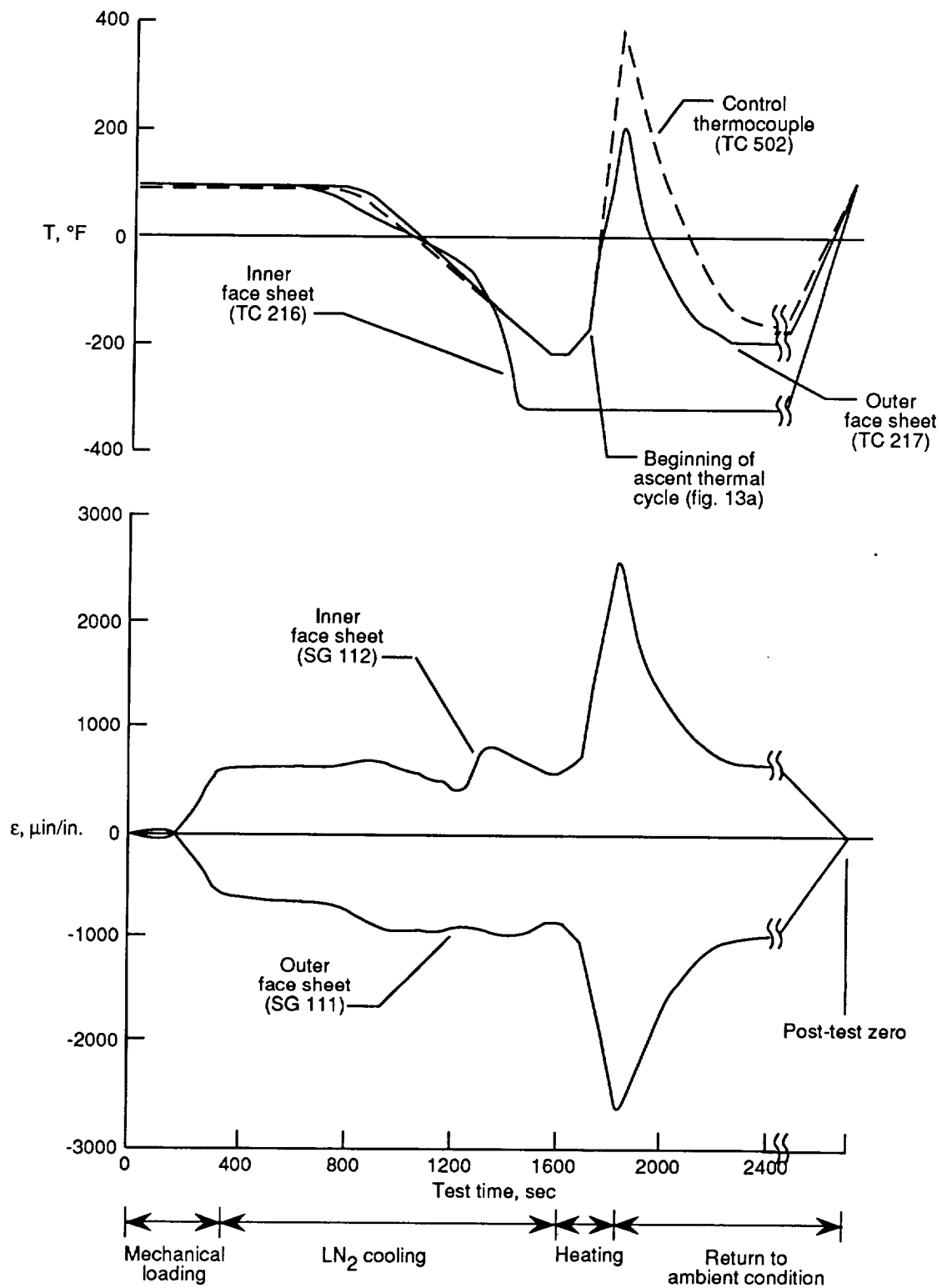
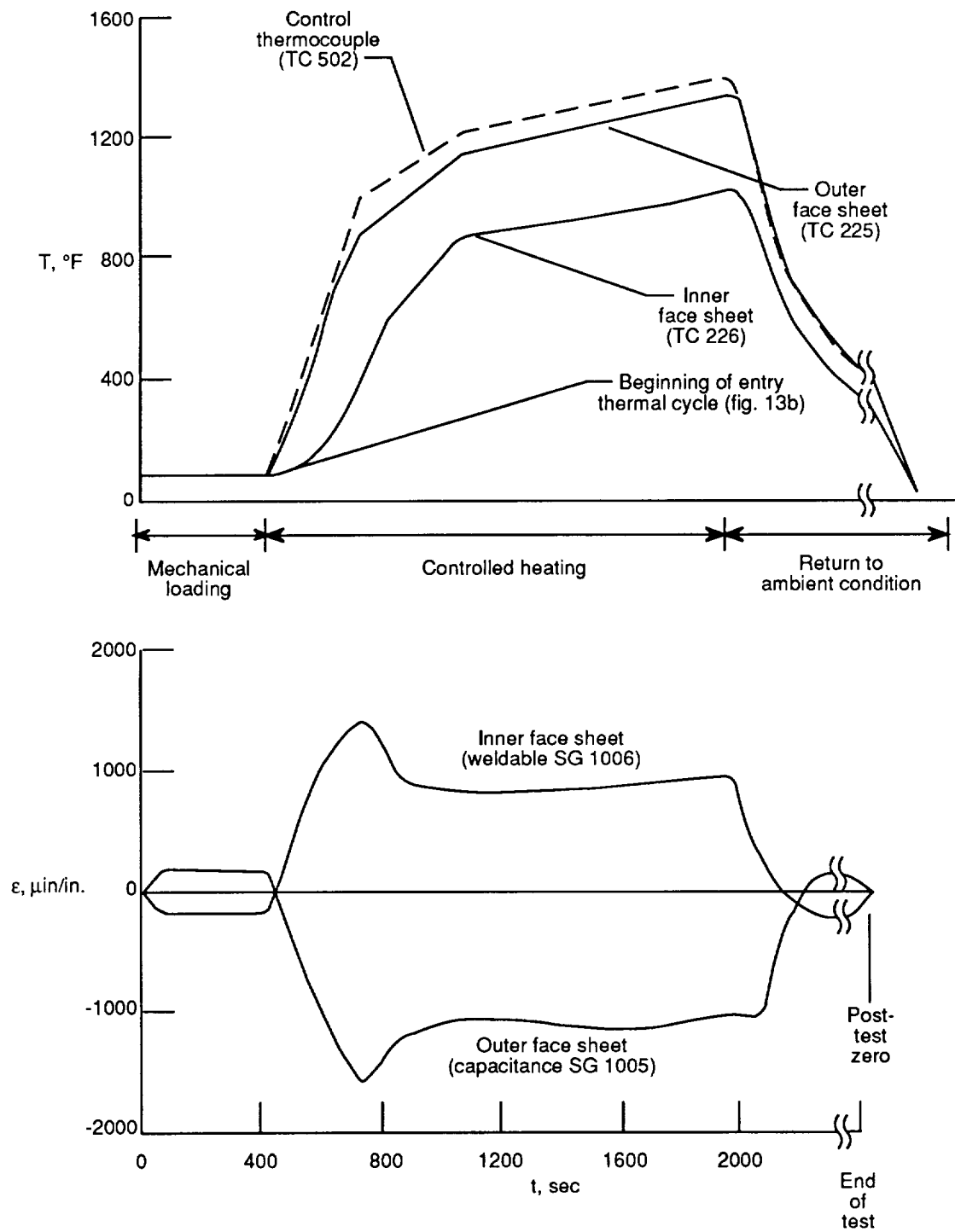


Figure 19. Finite-element model. Dimensions are in inches.



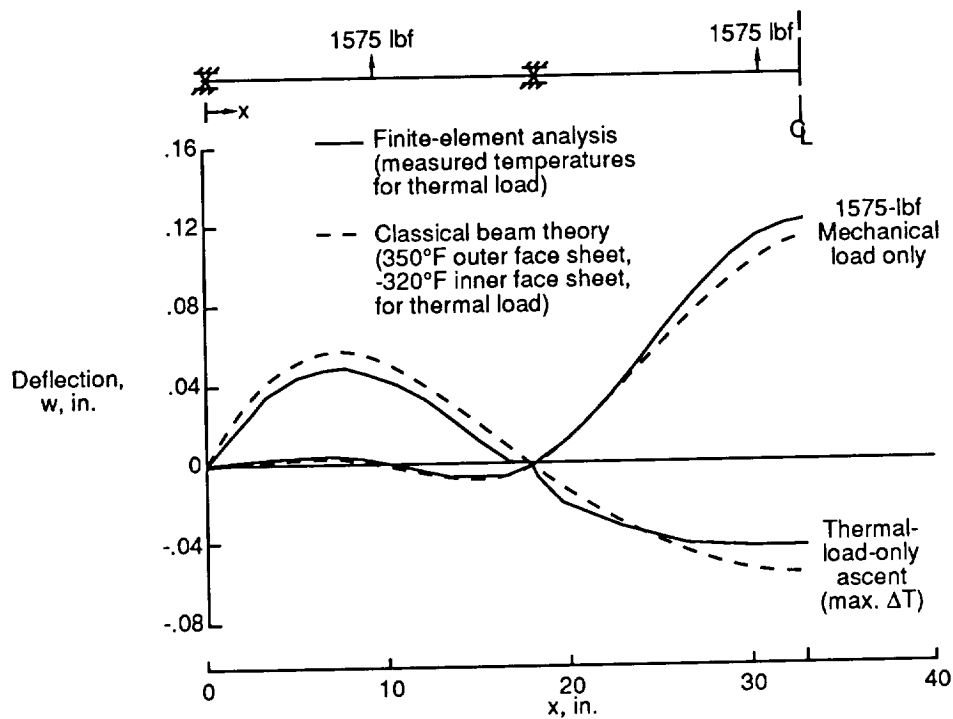
(a) Ascent cycle 81 of panel 2.

Figure 20. Typical measured temperatures and strains.

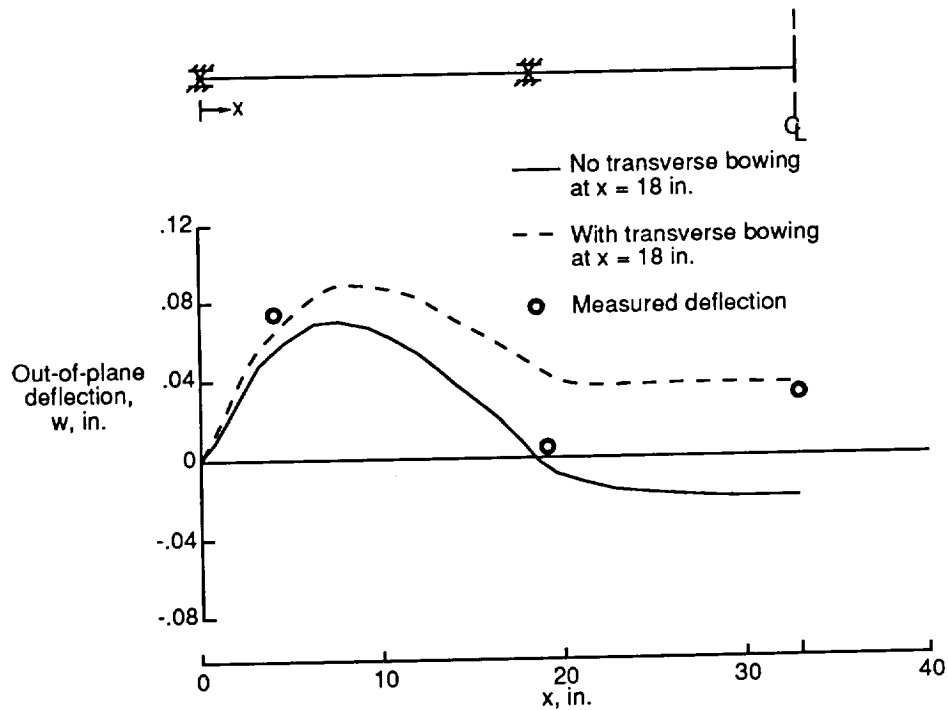


(b) Entry cycle 196 of panel 1.

Figure 20. Concluded.



(a) Calculated centerline ($y = 6$ in.) deflections with no transverse bowing at $x = 18$ in.



(b) Calculated and measured deflections at $y = 8.6$ in. due to measured temperatures for thermal-load-only ascent cycle.

Figure 21. Typical deflections of panel 2.

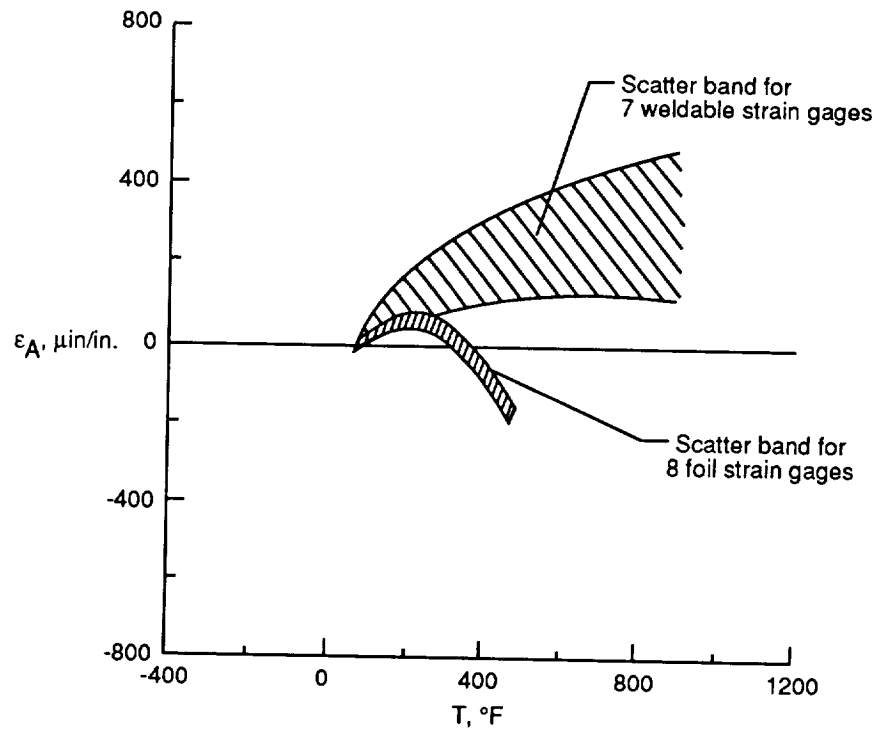
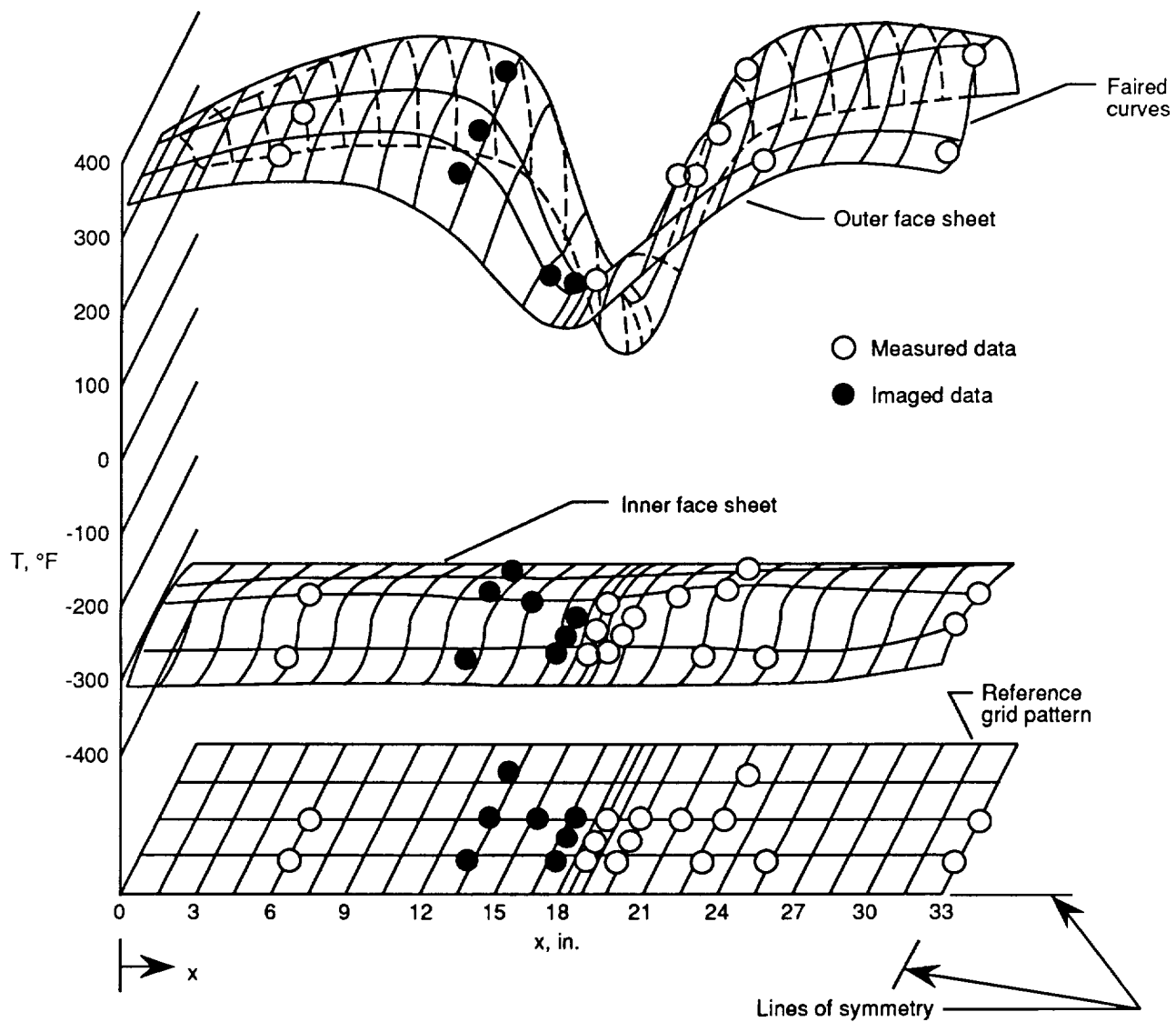
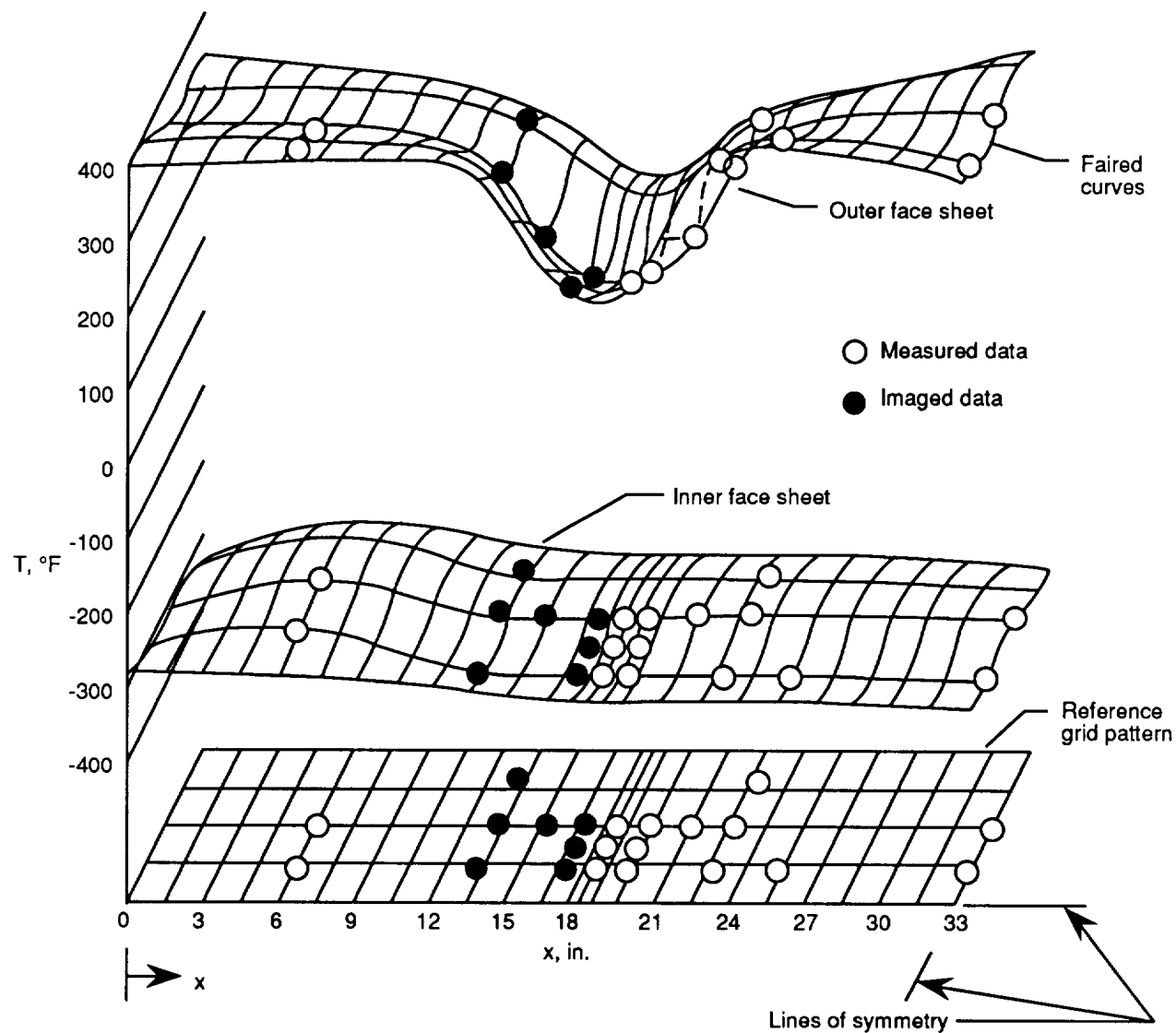


Figure 22. Apparent strain for foil and weldable strain gages attached to titanium (from ref. 14).



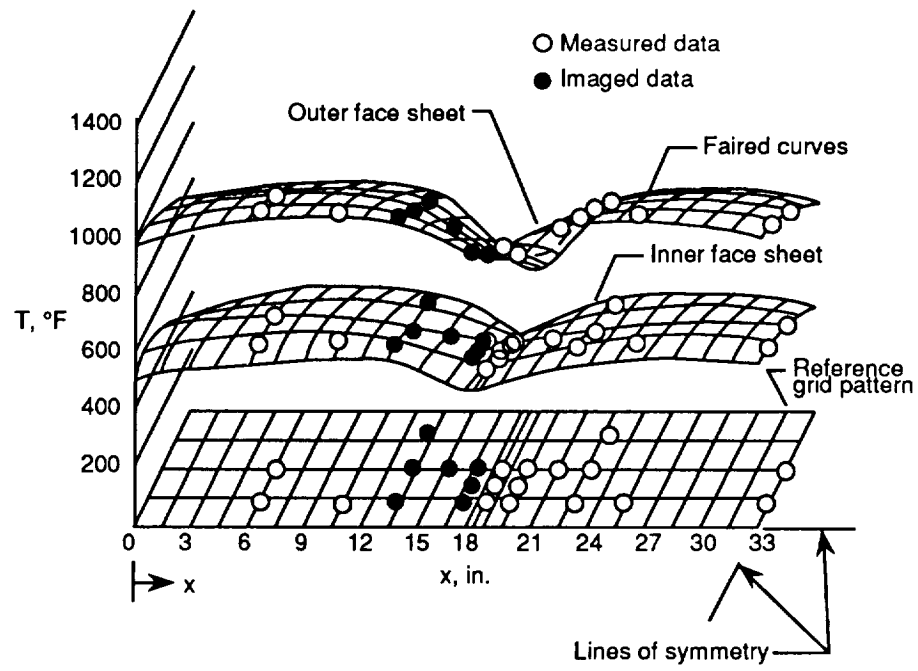
(a) Cycle 1.

Figure 23. Typical face-sheet temperature distributions at time of maximum ascent temperature ($t = 120$ sec) for panel 1.

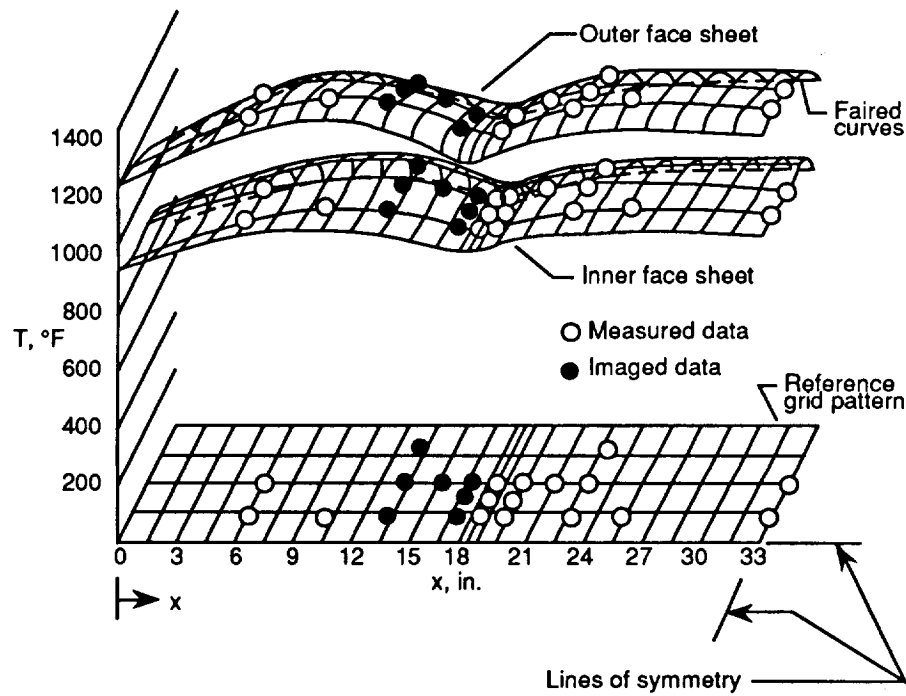


(b) Cycle 500.

Figure 23. Concluded.



(a) At time of maximum temperature difference ($t = 230$ sec).



(b) At time of maximum temperature ($t = 1490$ sec).

Figure 24. Face-sheet temperature distributions for entry cycle 500 of panel 1. Typical for entry cycles 135 through 500.

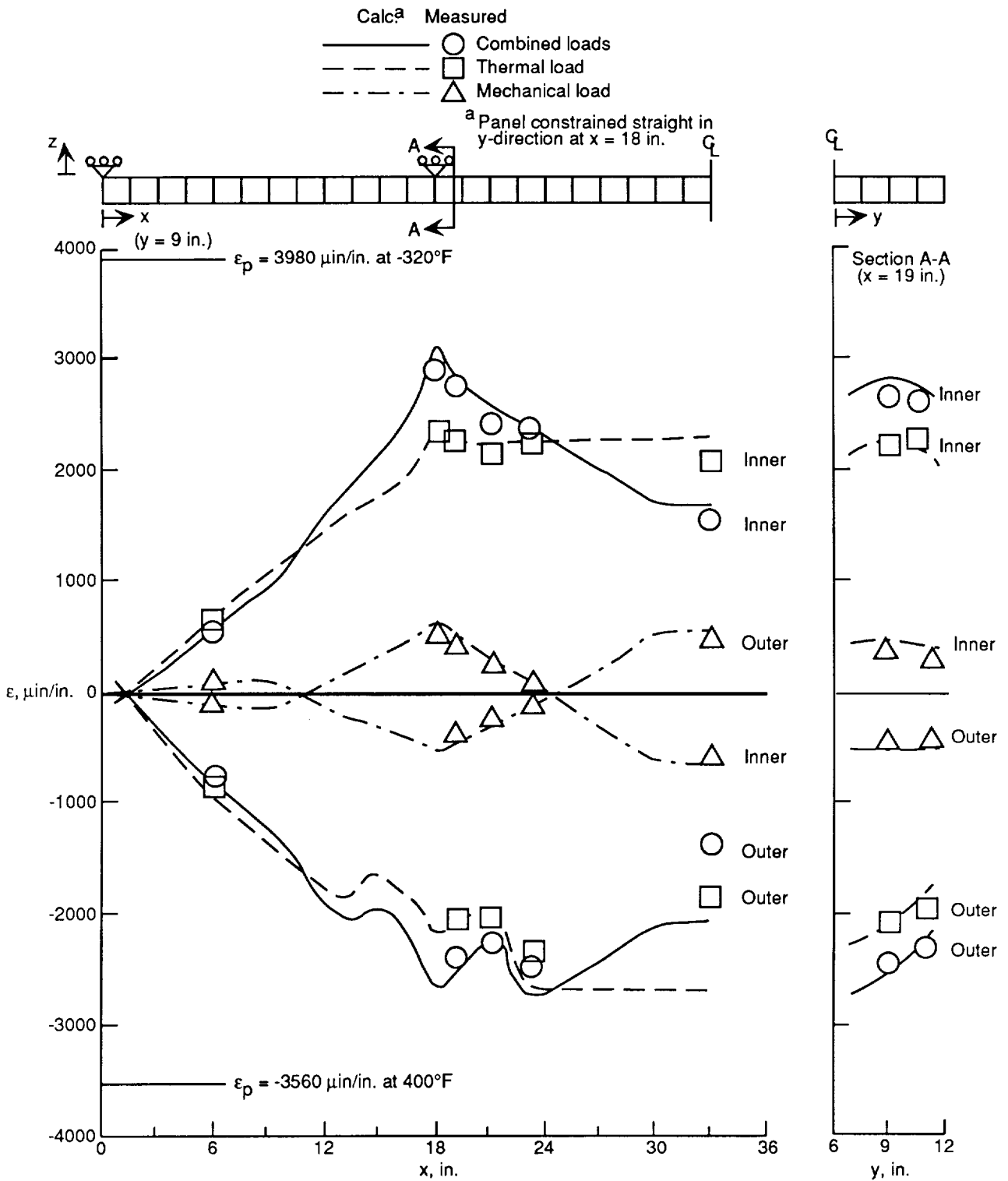


Figure 25. Calculated and measured (with foil gages) longitudinal strains at time of maximum ascent temperature ($t = 120 \text{ sec}$) for ascent cycle 1 of panel 1.

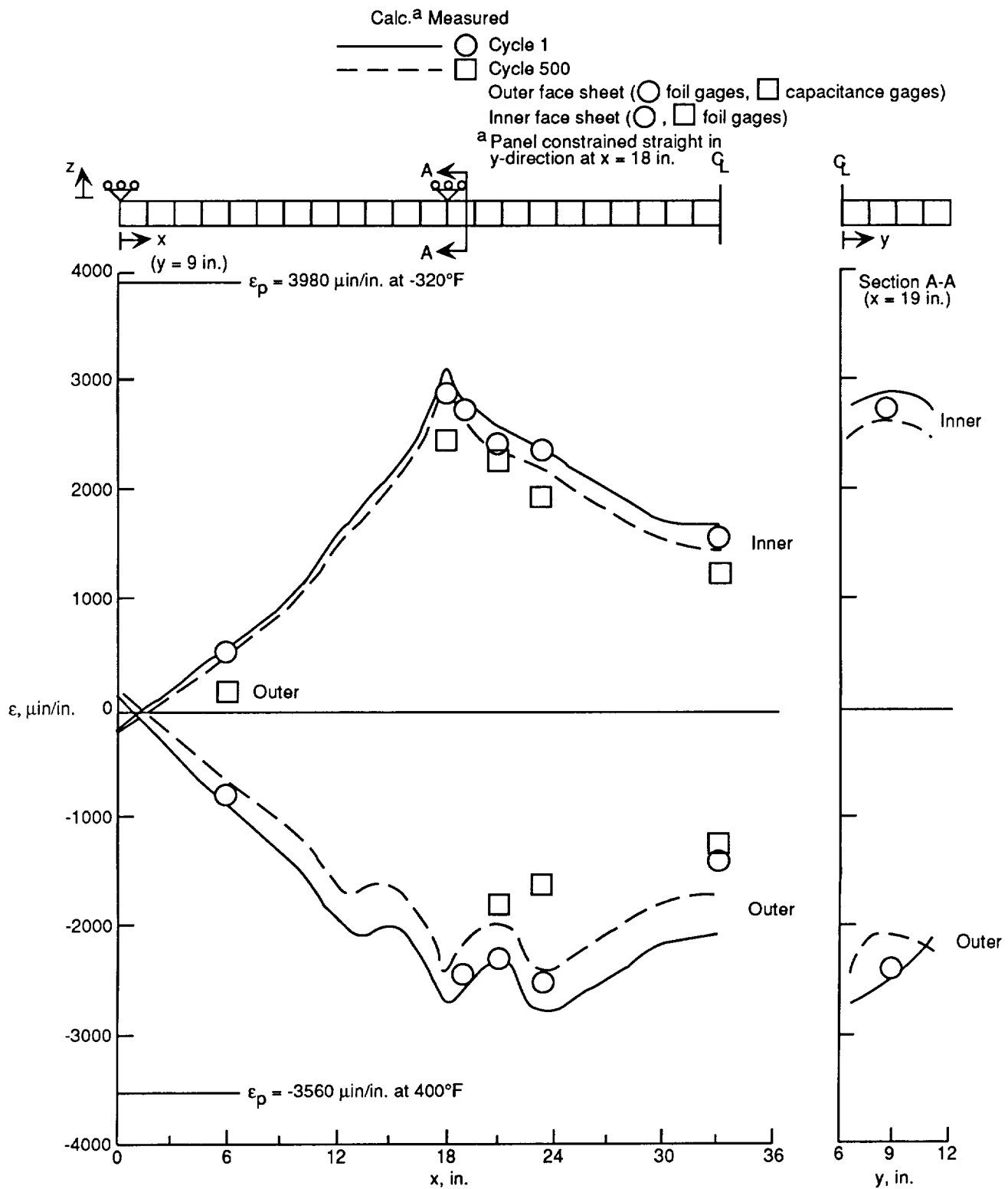
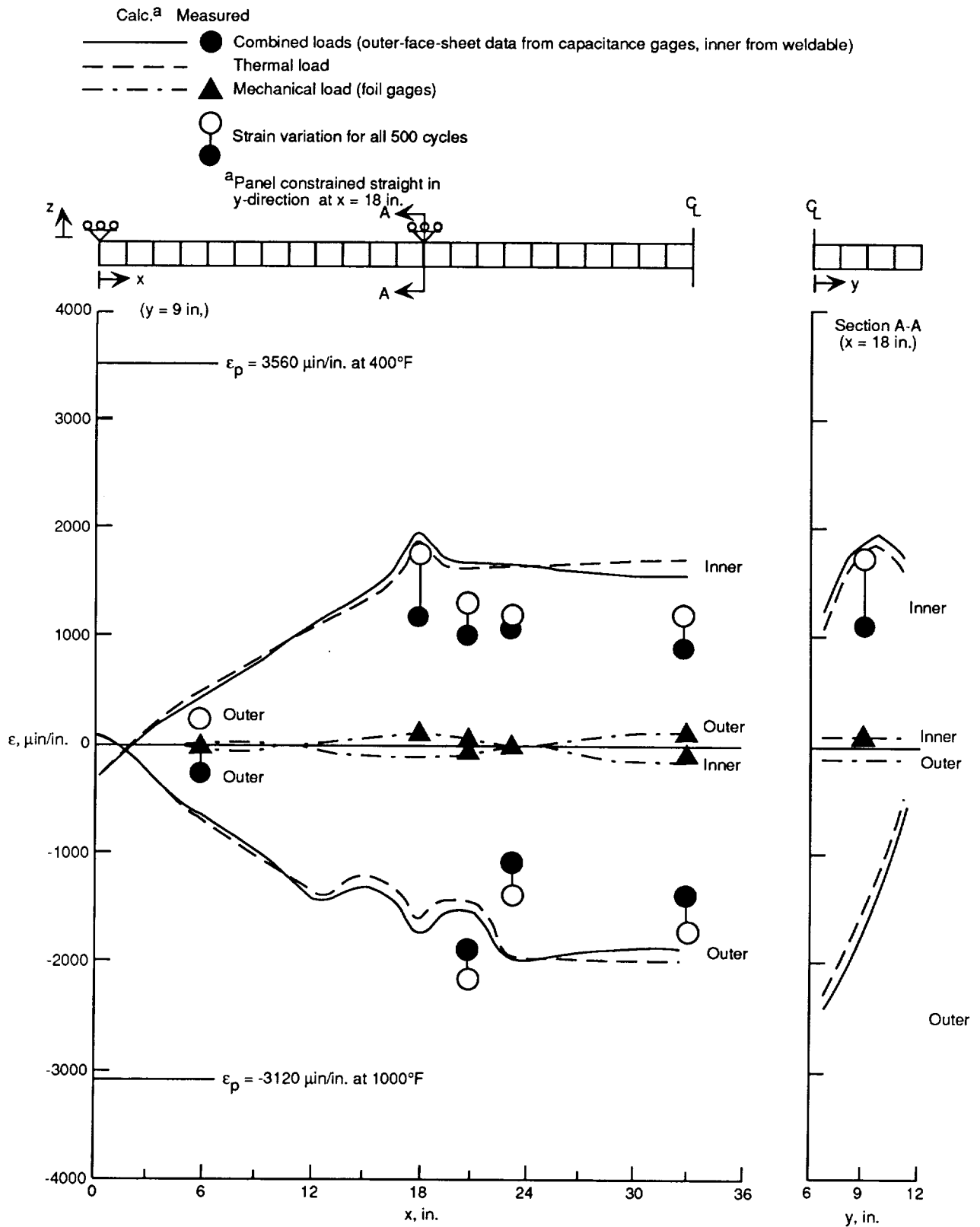


Figure 26. Calculated and measured longitudinal strains for combined thermal and mechanical loads at time of maximum ascent temperature ($t = 120$ sec) for ascent cycles 1 and 500 of panel 1.



(a) At time of maximum temperature difference ($t = 230$ sec).

Figure 27. Calculated and measured longitudinal strains for entry cycle 500 of panel 1.

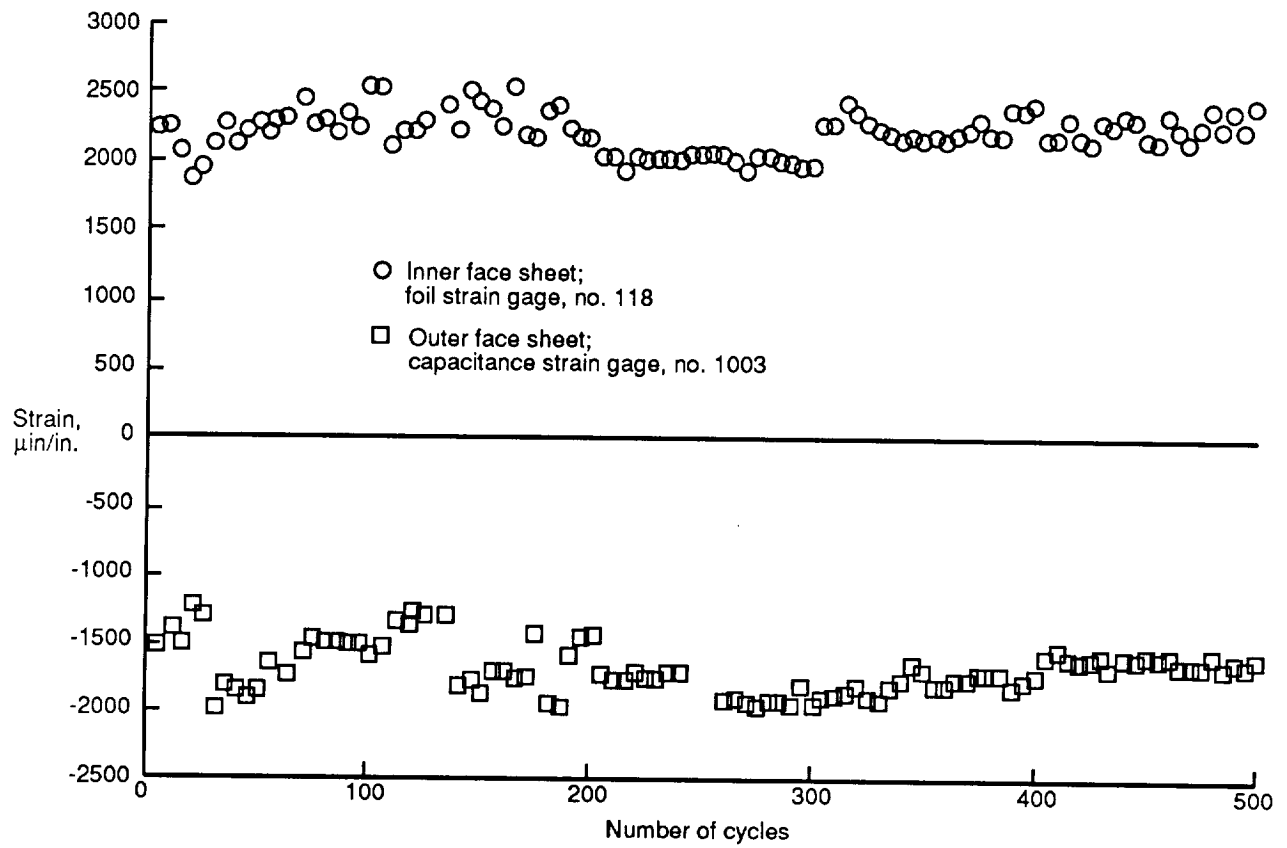


Figure 28. Measured longitudinal strain at $x = 20.84$ in. at time of maximum temperature for ascent cycles of panel 1.

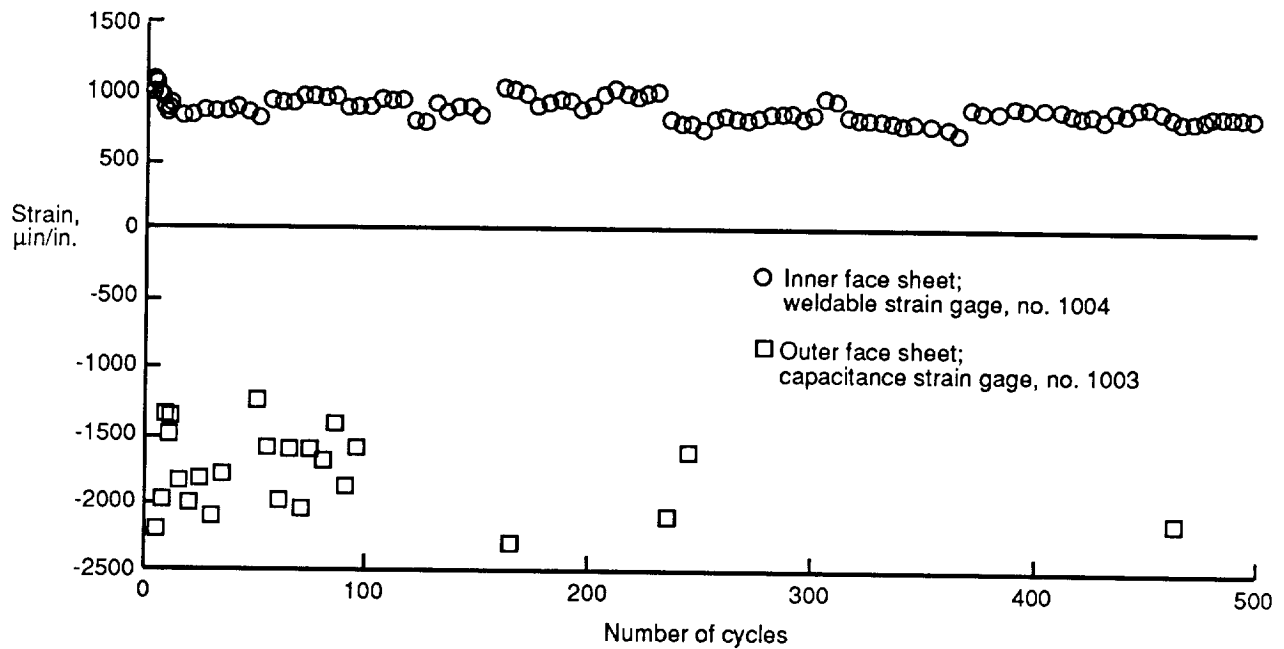
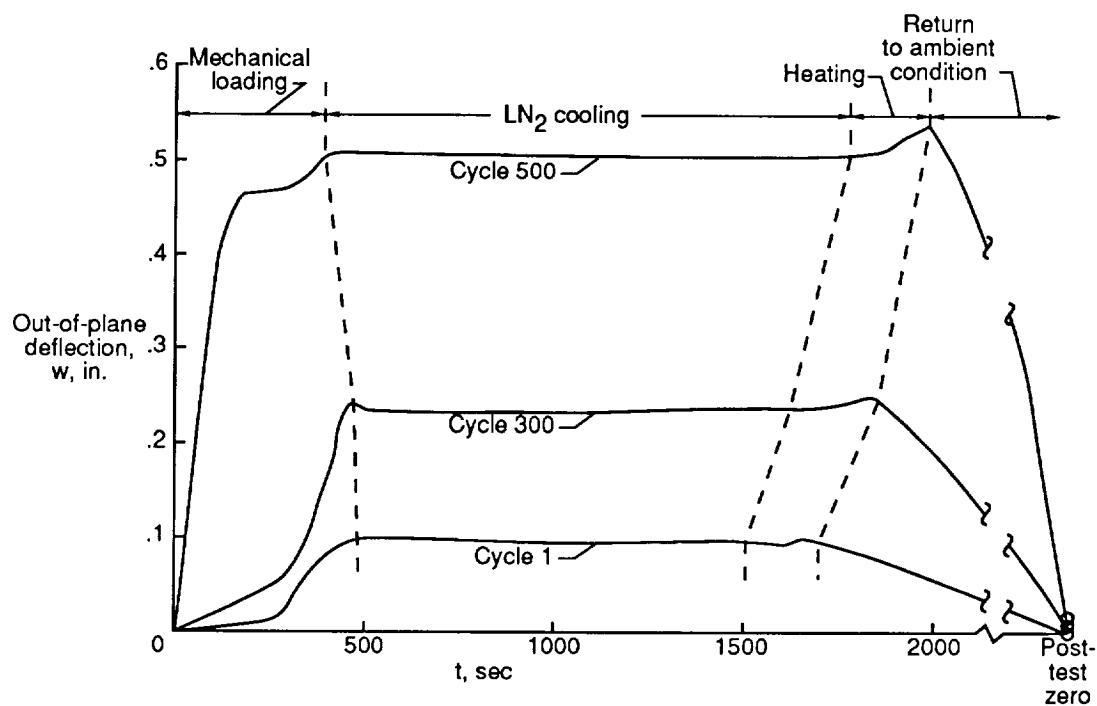
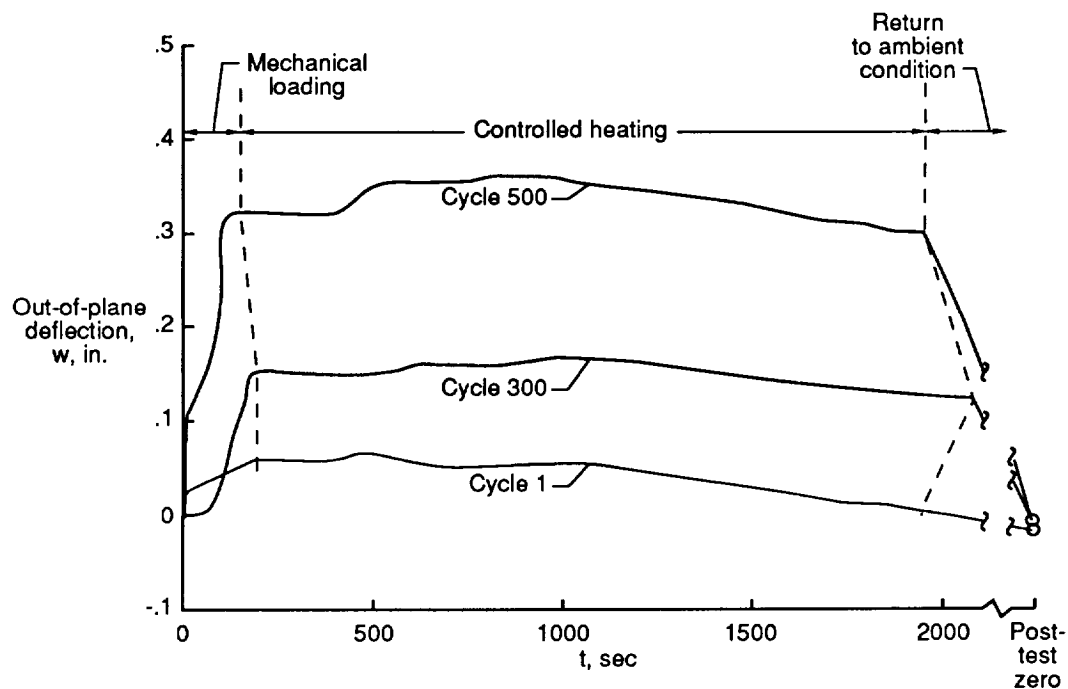


Figure 29. Measured longitudinal strain at approximately $x = 21$ in. at time of maximum temperature for entry cycles of panel 1.



(a) Ascent cycles.



(b) Entry cycles.

Figure 30. Measured out-of-plane center deflection versus time for panel 1. $x = 33$ in.; $y = 9$ in.

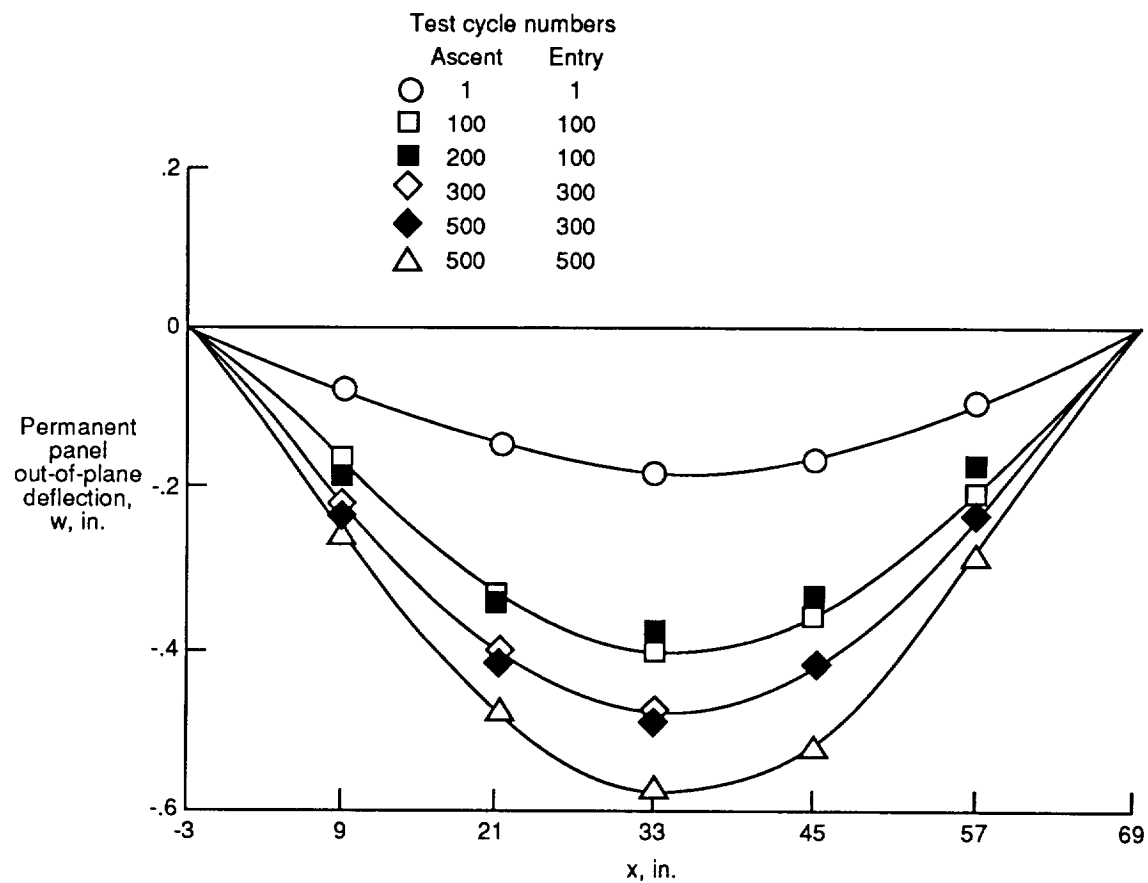
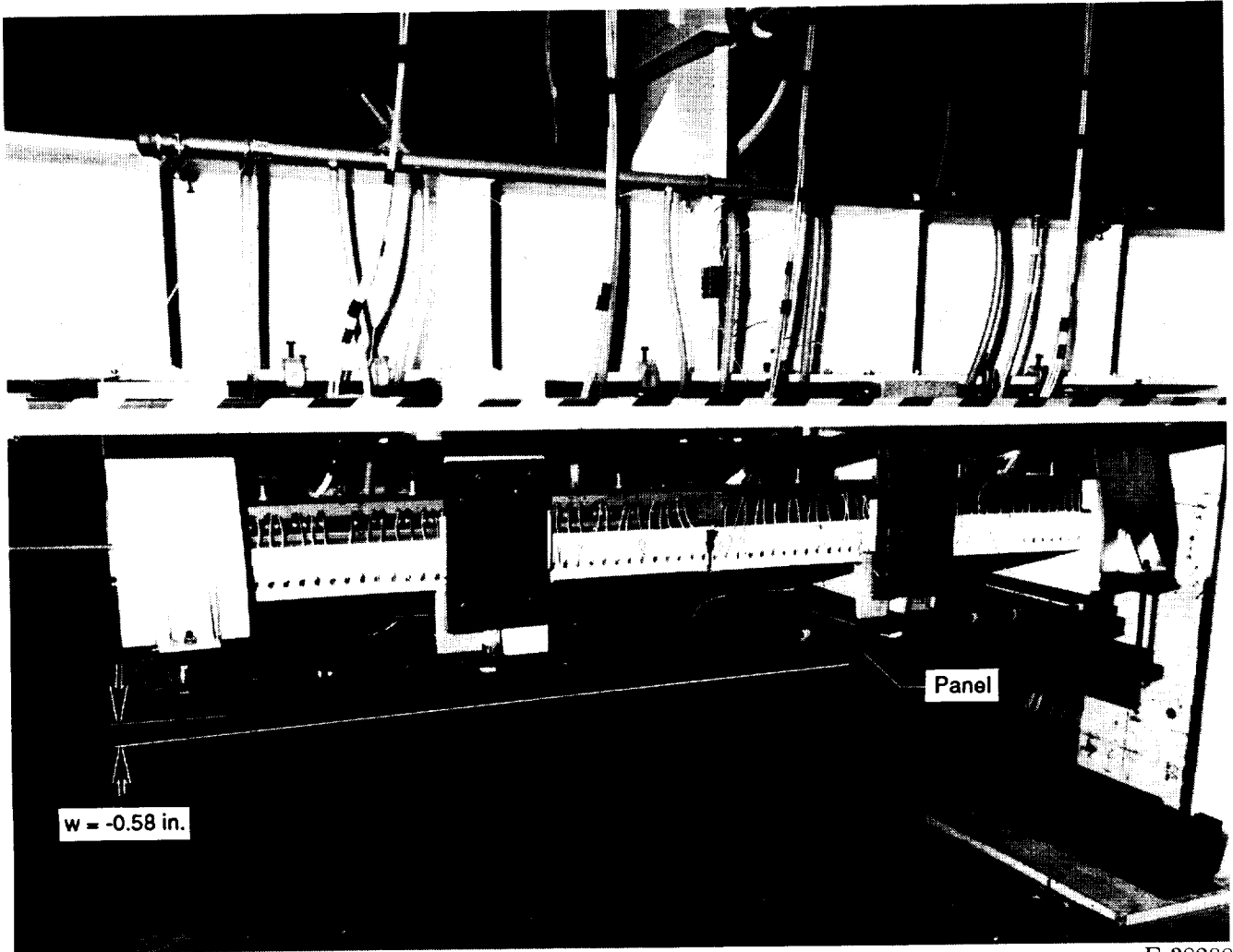
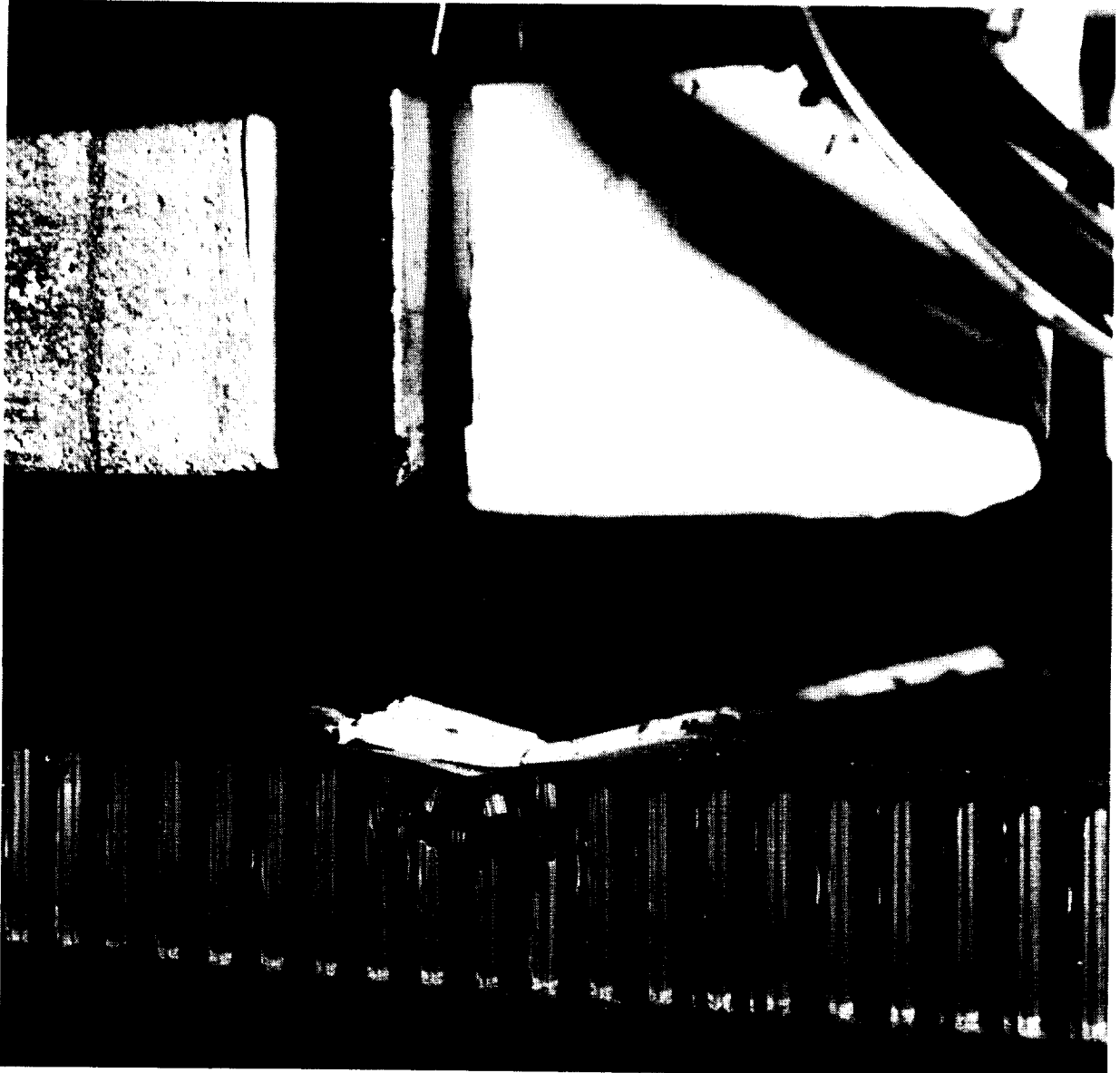


Figure 31. Permanent panel out-of-plane deflection after heating and loading cycles. Panel 1 at room temperature with no mechanical load. $y = 9$ in.



E-38288

Figure 32. Permanent out-of-plane deflection of panel 1 after 500 ascent and entry cycles.



E-38289

Figure 33. Crushed core area of panel 1 (cycle 532).

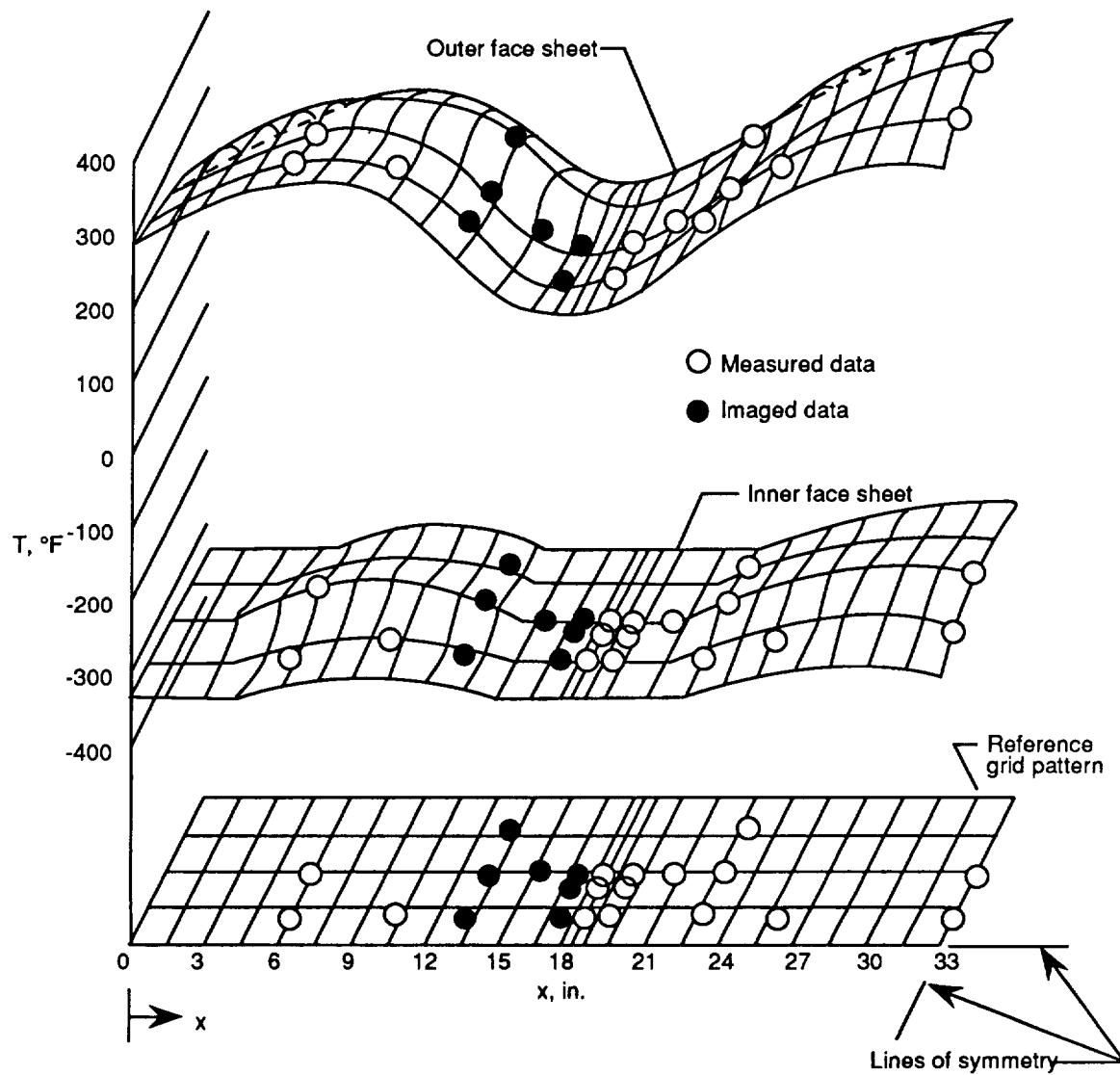


Figure 34. Face-sheet temperature distribution at time of maximum ascent temperature ($t = 120$ sec) for cycle 81 of panel 2.

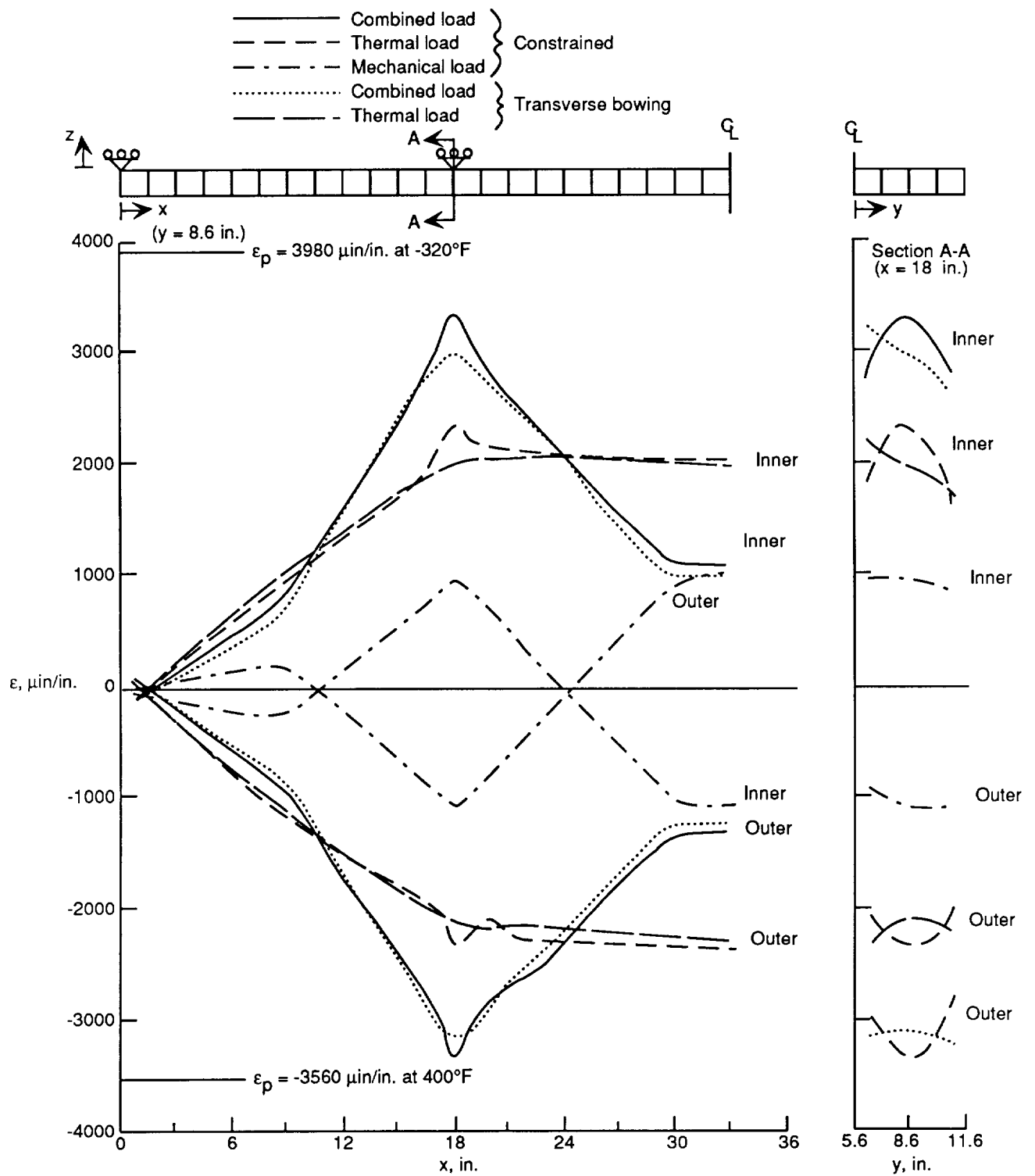


Figure 35. Calculated longitudinal strain distribution at time of maximum temperature ($t = 120$ sec) with two different constraints at $x = 18$ in. for ascent cycle 81 of panel 2.

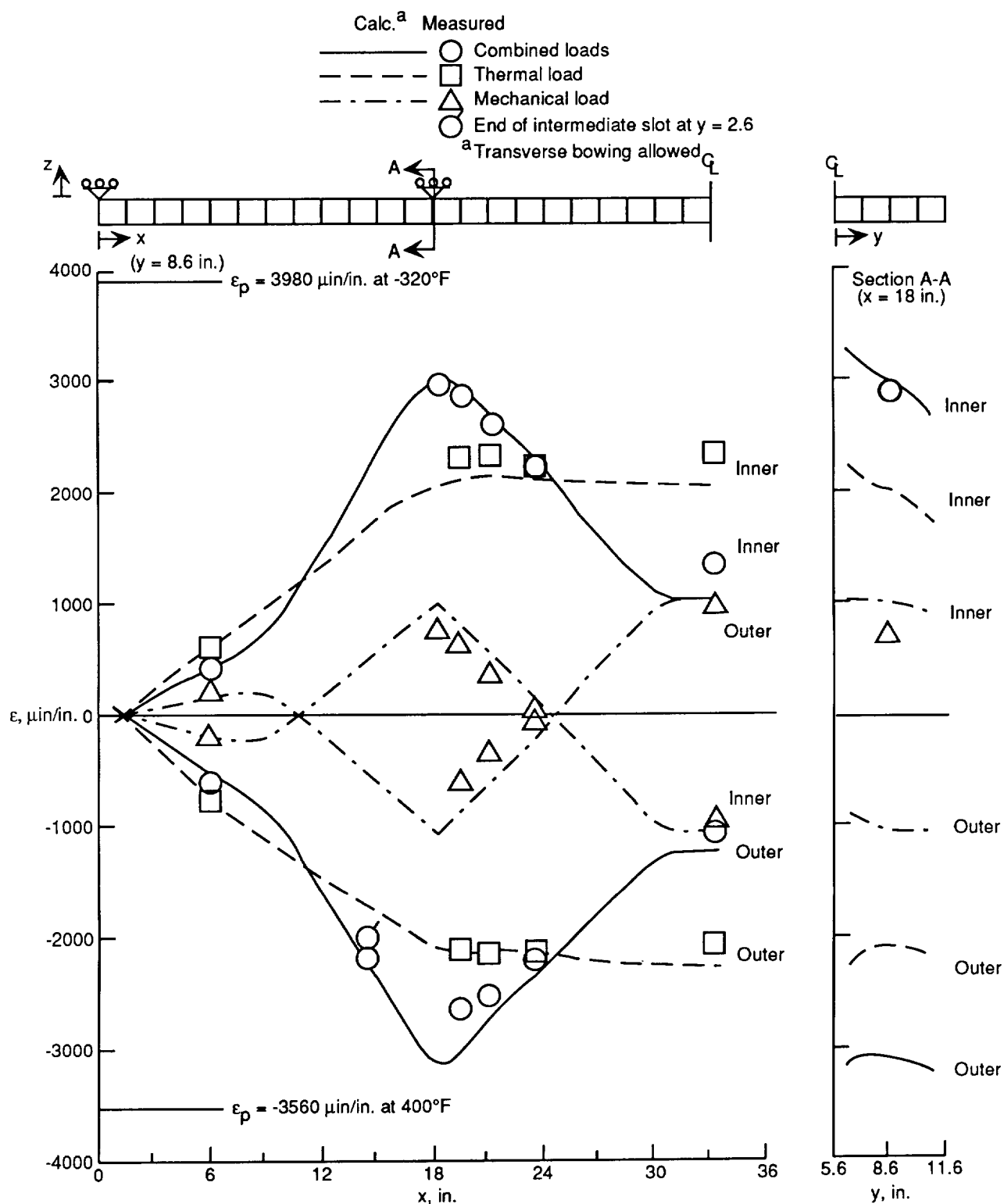


Figure 36. Calculated and measured (with foil gages) longitudinal strains at time of maximum temperature ($t = 120$ sec) for ascent cycle 81 of panel 2.

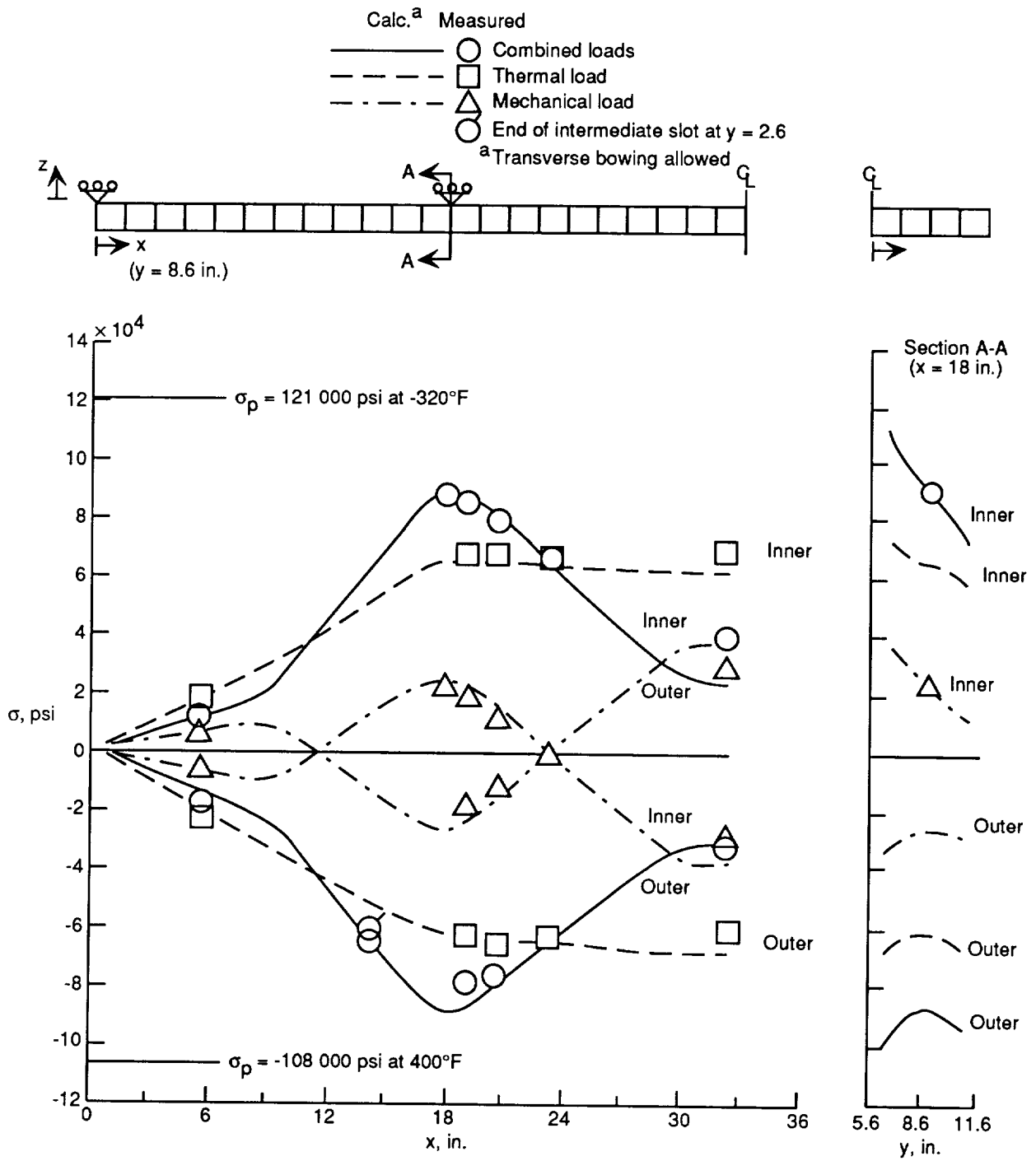


Figure 37. Calculated and measured (with foil gages) longitudinal stresses at time of maximum temperature ($t = 120$ sec) for ascent cycle 81 of panel 2.

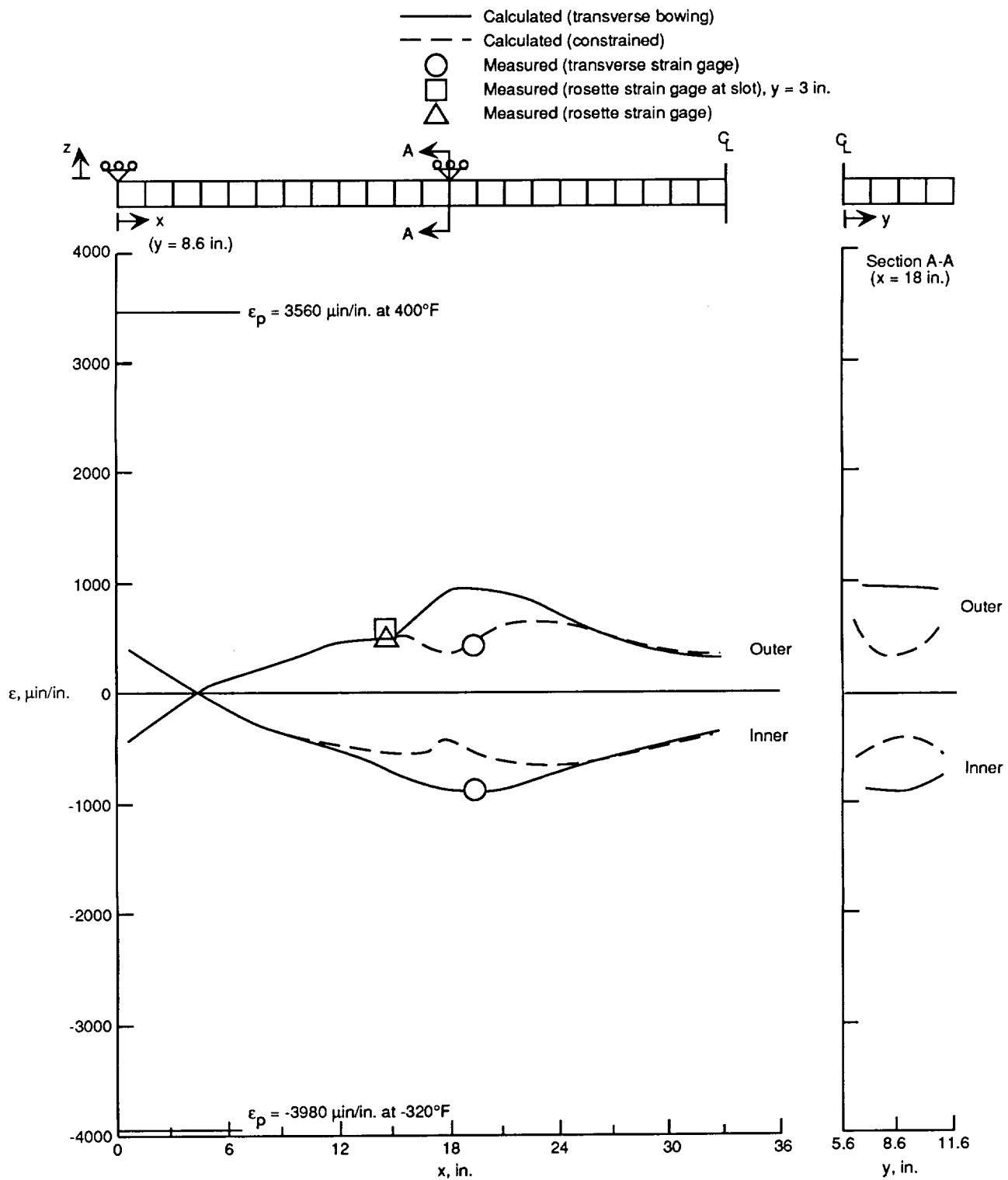


Figure 38. Calculated and measured (with foil gages) transverse strains due to combined loads at time of maximum temperature ($t = 120$ sec) for ascent cycle 81 of panel 2.

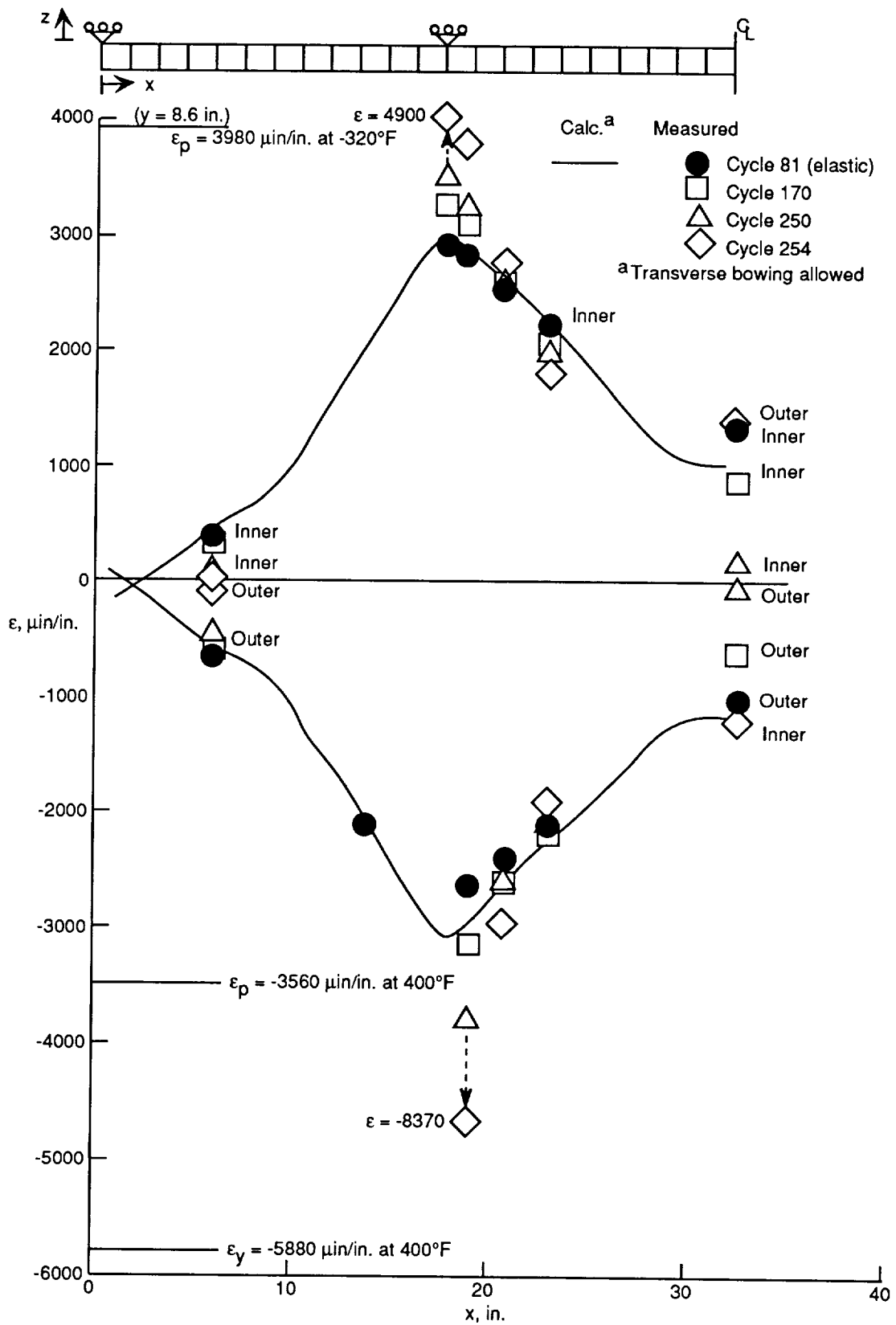
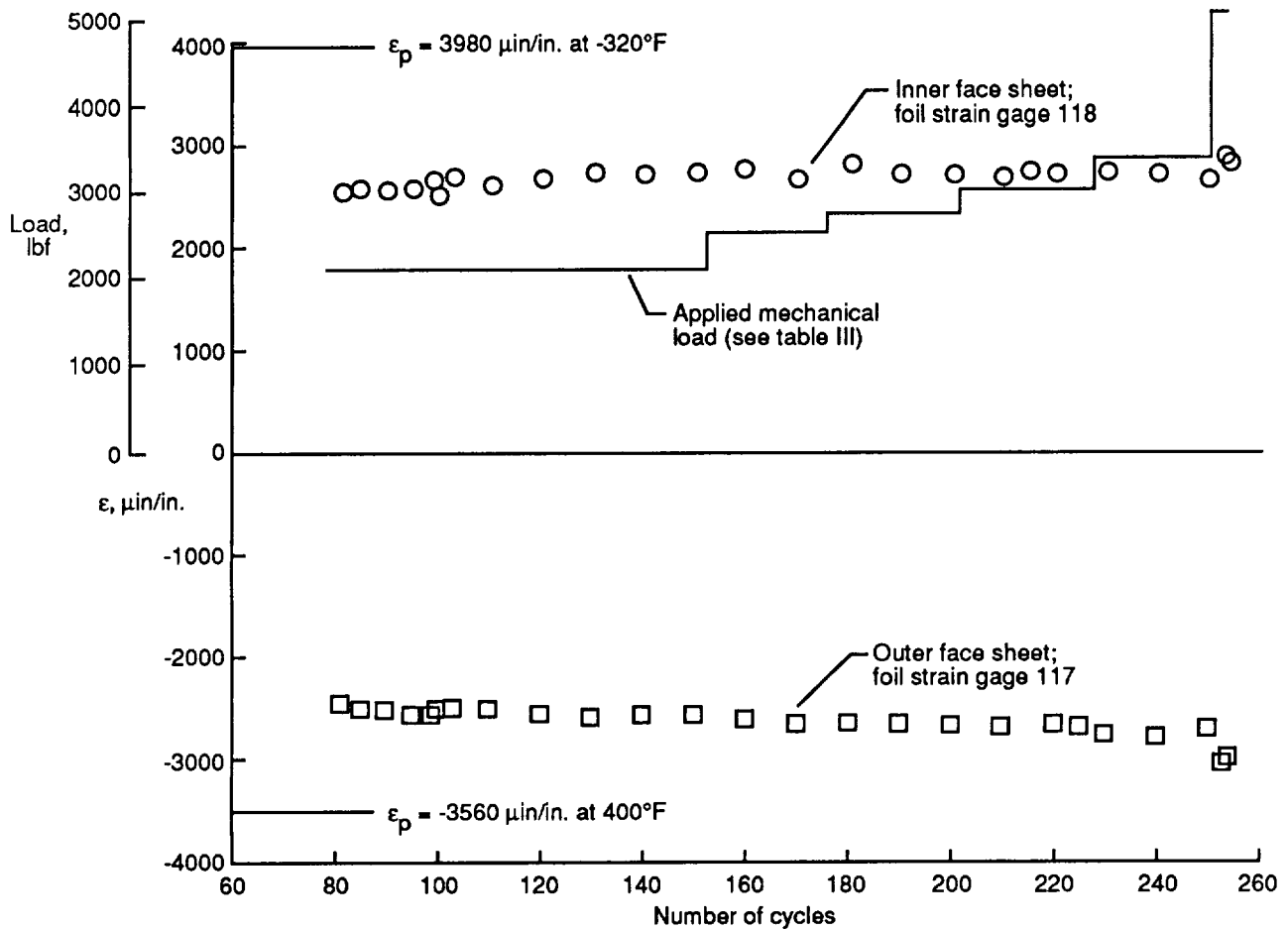
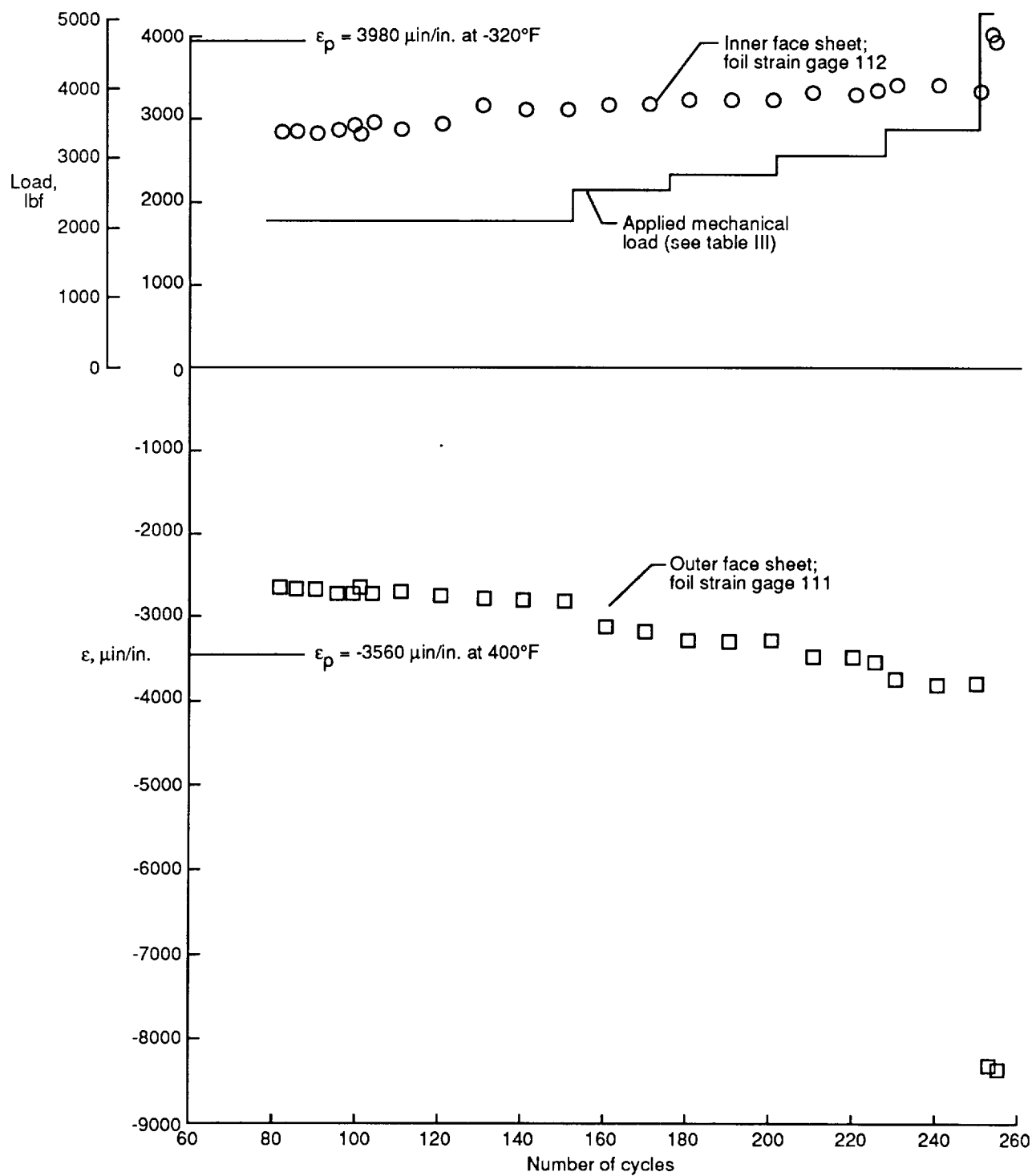


Figure 39. Measured (with foil gages) longitudinal strains at time of maximum ascent cycle temperature ($t = 120 \text{ sec}$) and increasing mechanical load for panel 2.



(a) At location $x = 21$ in.

Figure 40. Longitudinal strain near reaction point at time of maximum temperature ($t = 120$ sec) for ascent cycles of panel 2.



(b) At location $x = 19$ in.

Figure 40. Concluded.

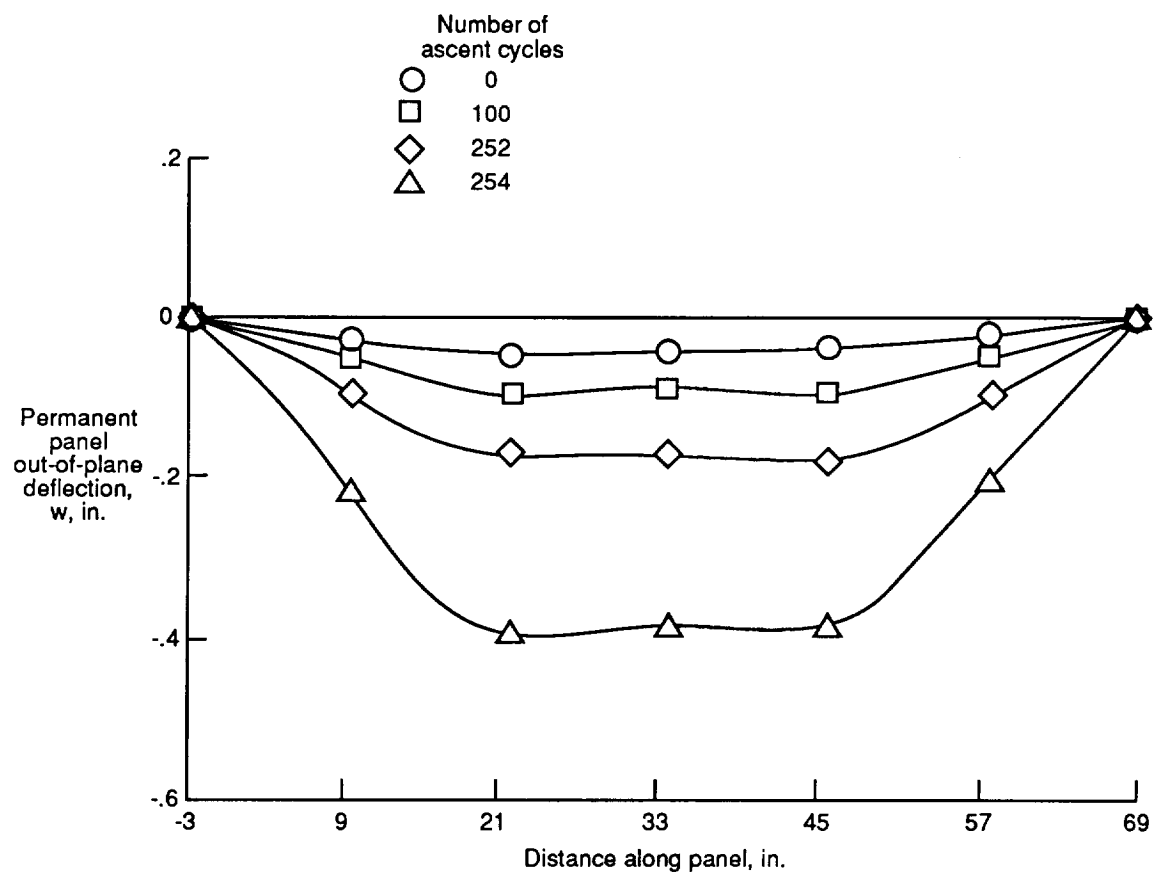
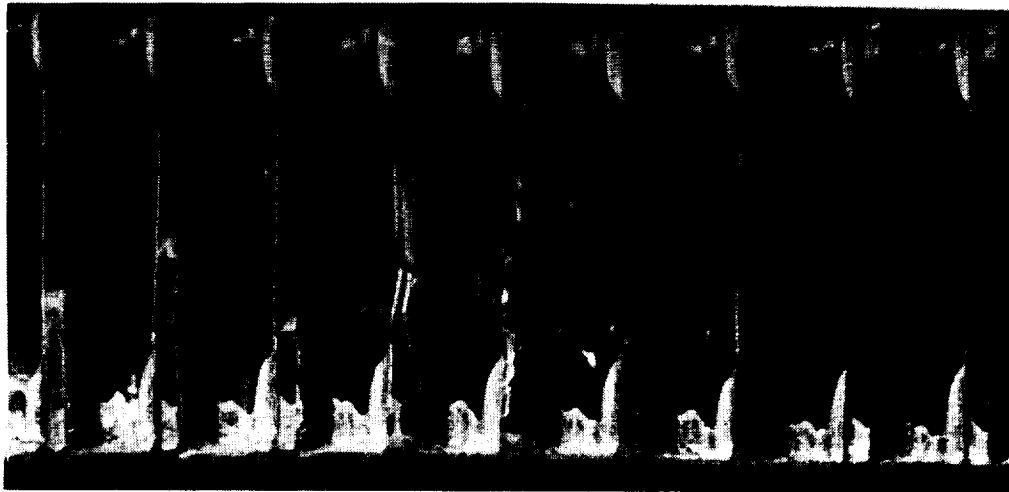


Figure 41. Permanent panel out-of-plane deflection after ascent tests for panel 2 at room temperature with no mechanical load.



E-38835

Figure 42. Core buckling at $x = 36$ in. for cycle 254 of panel 2.

REPORT DOCUMENTATION PAGE			Form Approved OMB No. 0704-0188	
Public reporting burden for this collection of information is estimated to average 1 hour per response, including the time for reviewing instructions, searching existing data sources, gathering and maintaining the data needed, and completing and reviewing the collection of information. Send comments regarding this burden estimate or any other aspect of this collection of information, including suggestions for reducing this burden, to Washington Headquarters Services, Directorate for Information Operations and Reports, 1215 Jefferson Davis Highway, Suite 1204, Arlington, VA 22202-4302, and to the Office of Management and Budget, Paperwork Reduction Project (0704-0188), Washington, DC 20503				
1. AGENCY USE ONLY (Leave blank)	2. REPORT DATE May 1992	3. REPORT TYPE AND DATES COVERED Technical Paper		
4. TITLE AND SUBTITLE Thermal and Structural Tests of René 41 Honeycomb Integral-Tank Concept for Future Space Transportation Systems		5. FUNDING NUMBERS WU 506-43-71-05		
6. AUTHOR(S) John L. Shideler, Roger A. Fields, Lawrence F. Reardon, and Leslie Gong				
7. PERFORMING ORGANIZATION NAME(S) AND ADDRESS(ES) NASA Langley Research Center Hampton, VA 23665-5225		8. PERFORMING ORGANIZATION REPORT NUMBER L-16752		
9. SPONSORING/MONITORING AGENCY NAME(S) AND ADDRESS(ES) National Aeronautics and Space Administration Washington, DC 20546-0001		10. SPONSORING/MONITORING AGENCY REPORT NUMBER NASA TP-3145		
11. SUPPLEMENTARY NOTES Shideler: Langley Research Center, Hampton, VA; Fields, Reardon, and Gong: Dryden Flight Research Facility, Edwards, CA.				
12a. DISTRIBUTION/AVAILABILITY STATEMENT Unclassified - Unlimited Subject Category 39		12b. DISTRIBUTION CODE		
13. ABSTRACT (Maximum 200 words) Two flat 12- by 72-in. René 41 honeycomb sandwich panels were tested in a manner to produce combined thermal and mechanical longitudinal stresses that simulated those that would occur in a larger, more complex integral tank-and-fuselage structure of an Earth-to-orbit vehicle. Elastic strains measured at temperatures below 400°F are compared with calculated values obtained from a linear elastic finite-element analysis to verify the analytical model and to establish confidence in the calculated strains. Elastic strains measured at higher temperatures (between about 600°F and 1400°F), where strain measurement is more difficult and less certain, are also compared with calculated strains. Agreement between measured and calculated strains for the lower temperatures is good, but agreement for the higher temperatures is poor because of unreliable strain measurements. Test results indicate that an ascent-and-entry life cycle of 500 is attainable under high combined thermal and mechanical elastic strains.				
14. SUBJECT TERMS René 41 honeycomb sandwich; Space transportation systems; Integral tank-and-fuselage; Hot structures; Combined thermal-structural tests			15. NUMBER OF PAGES 75	
			16. PRICE CODE A04	
17. SECURITY CLASSIFICATION OF REPORT Unclassified	18. SECURITY CLASSIFICATION OF THIS PAGE Unclassified	19. SECURITY CLASSIFICATION OF ABSTRACT	20. LIMITATION OF ABSTRACT	

NSN 7540-01-280-5500

Standard Form 298 (Rev. 2-89)
Prescribed by ANSI Std. Z39-18
298-102

NASA-Langley, 1992